ORNL/Sub--87-SB046/1

DE92 041383

ANALYTICAL AND EXPERIMENTAL EVALUATION OF JOINING CERAMIC OXIDES TO CERAMIC OXIDES AND CERAMIC OXIDES TO METAL FOR ADVANCED HEAT ENGINE APPLICATIONS

J. Ahmad, B. Majumdar, A. R. Rosenfield, S. L. Swartz,
J. Cawley, E. Park, D. Hauser, and A. T. Hopper

Date Published-April 1992

FINAL REPORT

Prepared by Battelle Columbus Laboratories
505 King Avenue
Columbus, Ohio 43201-2693
86X-SB046C

Funded by
Office of Transportation Materials
Office of Transportation Technologies
the Assistant Secretary for Conservation and Renewable Energy
U.S. Department of Energy
EE 51 01 00 0

for
OAK RIDGE NATIONAL LABORATORY
Oak Ridge, Tennessee 37831
managed by
MARTIN MARIETTA ENERGY SYSTEMS, INC.
for the
U.S. DEPARTMENT OF ENERGY
under Contract DE-AC05-84OR21400

CONTENTS

CONTENTS (cont.)

FIGURES

FIGURES (cont.)

FIGURES (cont.)

FIGURES (cont.)

TABLES

LIST OF SYMBOLS

α	coefficient of linear thermal expansion
β	constant appearing in Equation (25)
Γ	contour of integration
γ	constant appearing in Equation (25)
δ_{ij}	Kronecker delta
ΔT	difference between joining temperature and test temperature
ε	Bimaterial constant
ε	strain
η	logarithmic term in stress field
θ	angle measured from disk-bond line to compressive loading direction
λ	measure of thermal stress singularity at the specimen edge
μ	shear modulus
ν	Poisson's ratio
σ	stress
σ_0	yield strength
σ_c	critical stress value
σ_R	uniform compressive residual stress
σ_R	residual stress
σ_t	nominal residual stress
σ_x	stress component in the x-direction
Φ	angle that assessment vector makes with the strength axis
χ	distance between center of interlayer and crack location
Ψ	phase angle measuring degree of mode I and mode II fracture toughness mixity
a	one half the total crack length
$\bar{a}$	dimensionless crack length, a/W
A	assessment vector magnitude
$\vec{A}$	assessment vector
B	specimen thickness
C	parameter in failure criterion on page 39
c	denotes ceramic when used as subscript
C	geometry dependent factor in asymptotic residual stress solution
D	coefficient in Ramberg-Osgood relation
E	Young's modulus
F_R	rational function of a/W used in calculating the residual stress load parameter P_R
f_s	shielding factor due to mismatches in Young's modulus
$\vec{G}$	crack driving force
G	total (elastic-plastic) energy release rate
G_c	critical crack driving force
G_e	elastic crack tip energy release rate
G_r	dimensionless crack driving force parameter
i	denotes interlayer when used as subscript

LIST OF SYMBOLS (cont.)

K_I	mode I (opening) fracture toughness for monolithic system
K_{Ic}	critical value of fracture toughness, a material property
K_{II}	mode II (shear) fracture toughness for monolithic system
L	distance between outer loading points in four point bend tests
m	denotes metal when used as subscript
M	bending moment
n_j	outward normal to contour of integration Γ
P	total load on the joint
P_c	value of P at which joint failure occurs
P_f	predicted failure load
P_R	residual stress load parameter
P_r	dimensionless strength parameter
q	distance at which σ_x passes through zero
Q_I	mode I (opening) fracture toughness for bimaterial system
Q_{II}	mode II (shear) fracture toughness for bimaterial system
R	total tensile residual stress acting over the length q
R	radius of disk specimens
r	distance from edge of specimen
S	distance between inner loading points in four point bend tests
T	temperature
t_i	interlayer thickness
u_i	displacement component in direction i
V	volume percent zirconia in MASZ compositions
W	stress work density
W	bend bar depth
Y	a function used in reduction of experimental fracture toughness data

FINAL REPORT

on

ANALYTICAL AND EXPERIMENTAL EVALUATION OF JOINING CERAMIC OXIDES TO CERAMIC OXIDES AND CERAMIC OXIDES TO METAL FOR ADVANCED HEAT ENGINE APPLICATIONS

December 31, 1990

J. Ahmad, B. Majumdar, A. R. Rosenfield, S. L. Swartz,
J. Cawley, E. Park, D. Hauser, and A. T. Hopper

ABSTRACT

The problem of designing reliable, high strength zirconia-to-zirconia and zirconia-to-nodular cast iron joints is addressed by developing a general joint design and assessment methodology. A joint's load carrying capability is predicted in terms of its material strength and fracture toughness characteristics. The effects of joint constituent properties and joining process variables are included. The methodology is verified in a two step process by applying it first to notched bend bars and then to a notched disk specimen loaded in compression.

Key technical accomplishments in the program include the development of a joint design and assessment methodology which predicts failure based on a combination of strength and toughness, the development of a new method of hot forging magnesia partially stabilized zirconia to itself, and the development of a bimaterial disk-shaped specimen notched along the diametral bond line and compressively loaded to generate both shear and tensile loadings on the bond line.

Mechanical and thermal characterization of joints, adherents, and interlayer materials were performed to provide data for input to the design methodology. Results from over 150 room temperature tests and 30 high temperature tests are reported. Extensive comparisons of experimental results are made with model predictions of failure load.

The joint design and assessment model, as applied to the materials and test specimens of this program, has been programmed for a PC and is available to interested researchers.

EXECUTIVE SUMMARY

The research discussed in this report was funded by the U.S. Department of Energy under Subcontract No. 86X-SB046C to Martin Marietta Energy Systems. The program was one of three similar contracts dealing with developing a validated design methodology for improving the strength of joints made by joining tough ceramic oxides to either ceramic

oxides or to metals. This project deals with the development of procedures necessary for the design of reliable, high strength zirconia-to-zirconia and zirconia-to-nodular cast iron joints. The objectives were met by implementing a combined program of analysis and experimentation.

Figure 1 is a schematic of the program showing the relationships between the various tasks and milestones in the joint design methodology. It involved finite element analyses of the joint configurations based on joint geometry, properties of constituent materials (adherents and joint interlayers) and the joining temperature; reduction of the finite element analysis results to a simplified engineering joint assessment and design model; experimental evaluation of the failure load of notched and unnotched bend bars containing joints; using the preliminary validation results to fine tune the joint assessment and design model by incorporating factors which were previously not accounted for; and finally, testing cracked disk specimens and comparing measured and predicted fracture loads as part of the final validation of the methodology.

The joint assessment methodology, as it is currently formulated, can be used in two ways. First, it can be used in the machine design of components containing joints, where the processing conditions and interlayer constituents are already prescribed. Second, the methodology can be used for improving joint performance. In this latter mode, processing temperatures and constituent properties can be altered within limits and the model will provide a quantitative assessment of how those changes affect the load bearing capability of the joint relative to the load bearing capability of the monolithic ceramic of the same geometry.

ANALYTICAL DESIGN METHODOLOGY

An analytically based joint design methodology has been developed. The methodology has been applied to the particular materials and geometries studied in this program and the results incorporated into a PC code.

The essence of the methodology is that for a given specimen geometry and the manner in which it is loaded, a joint's load carrying capacity is determined by its strength and toughness properties. Which of the two properties dictates how and at what load failure occurs depends on their relative magnitude and residual stresses in the joint. Joint constituent properties influence the load carrying capacity of a joint through their inherent strength and toughness. Joining process variables influence the load bearing capacity through their effect on residual stresses, local stress-strain behavior and their effects on interlayer and joint constituent properties.

A key difference in this approach and other available formulations is the way failure depends on a combination of toughness and strength. The current approach represents a synergism of applied stress, crack length, toughness, residual stress, and strength in a self-consistent manner.

Stress analysis and fracture mechanics based models were developed for determining the stress field, σ, crack driving force, G, and residual stresses σ_R, for the test specimen geometries being tested in this program. These computations used linear and nonlinear finite element analyses which accounted for the physical properties of the joint constituents as well as the joining temperature and interlayer thickness. Other processing variables were

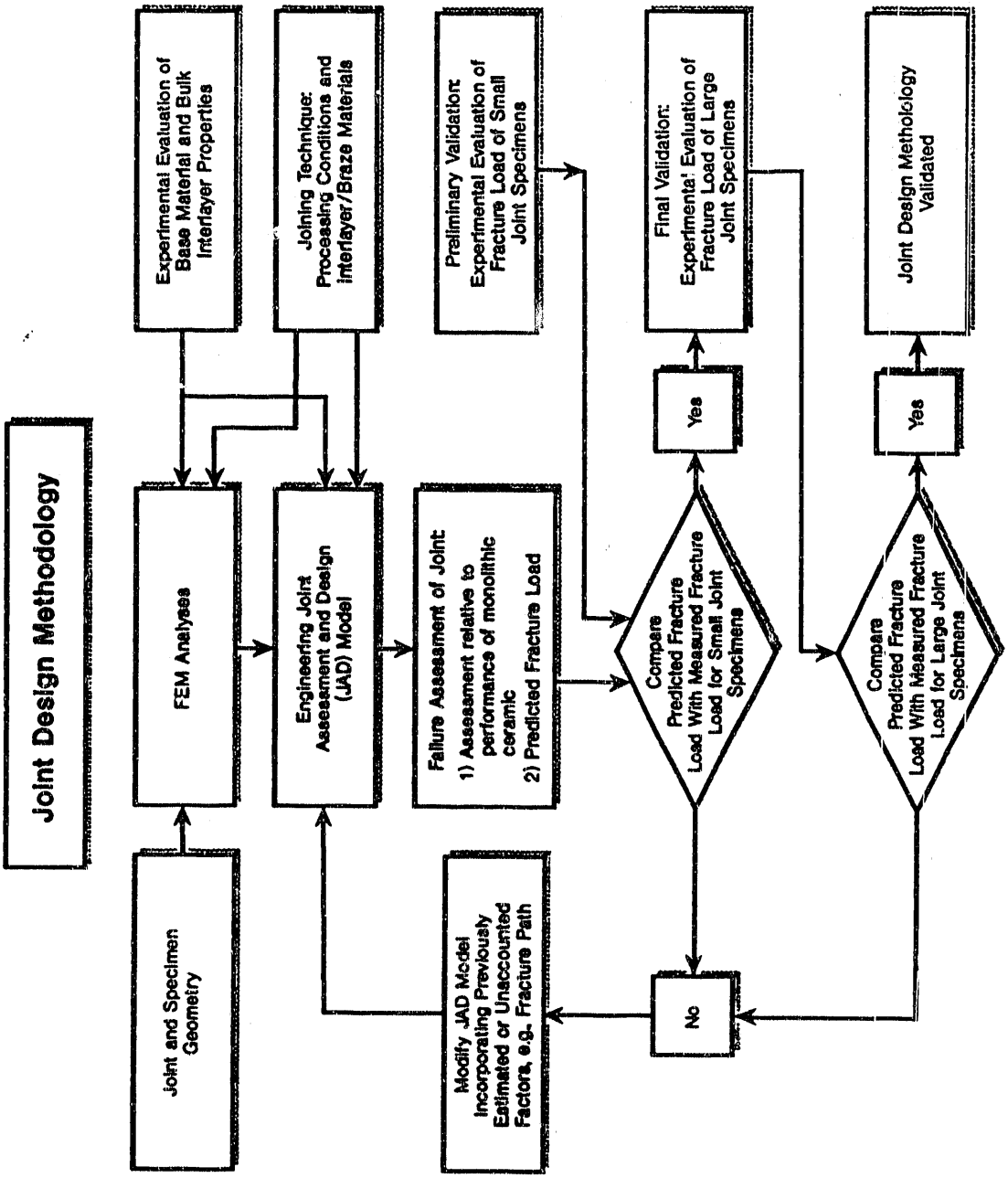

Figure 1. Schematic of joint design methodology development.

handled empirically. The results of the detailed analyses were used to develop simpler engineering models for estimating the factors which influence joint performance.

A joint assessment and design model (JAD model) which unifies the three primary factors (σ, G and σ_R) embodies the simplified analysis. The simplicity resides in the fact that the engineering model is fashioned after a homogeneous material. The complexity of the joint constituents and process conditions are handled by incorporating algebraic factors which account for thermal expansion mismatch effects (residual stresses) and shielding effects (arising from elastic modulus mismatch). A joint assessment vector $\vec{A}$ with components depending on strength, crack driving force, residual stress, and load was derived. It has the property that the smaller its magnitude, the less the propensity for failure of the joint. Another aspect of the design model is a failure curve which depends on the joint type and geometry. The conditions for which the vector extends to the failure curve for a given joint type and geometry define failure.

The area enclosed by the failure curve (or a fraction thereof) represents a design space for the joint. So long as $\vec{A}$ is within this space the joint is not predicted to fail under the prescribed load. For failure prediction, both the assessment vector and the failure curve are needed. A different application in which joint improvement is sought only requires the assessment vector. Here, at some specified reference or design load one would try to minimize the length of $\vec{A}$ with respect to suitably constrained values of the constituent properties and process variables.

JOINT FABRICATION

To validate the methodology and provide input data to the analyses, joints were fabricated by bonding blocks of ceramic and iron materials. Specimens were machined from the resulting billets. All bonds were geometrically simple butt joints to facilitate both analysis and experiment. While smaller joints (typically 1.0-1.6 cm^2) were produced for initial screening, the strength and fracture test specimens were cut from large ($\geq$20 cm^2) bonded areas.

Since bonded joints are likely to contain measurable flaws, it is essential to measure both strength and fracture toughness, either of which property can control the load-carrying capacity of a joint. Furthermore, because joints composed of dissimilar materials have an inherent mixed mode nature arising from elastic property mismatch between constituents, it is important to assess any design and predictive methodology by imposing various combinations of tensile and shear loads on the joints.

Two geometries were used for mechanical testing: bend bars and disks. The bend bar is the most common specimen for measuring ceramic strength in tension. It is also well established as a fracture-toughness specimen. The disk specimen, developed as part of this research, consists of two D-shaped pieces bonded together and loaded in compression. By varying the angle between the bond line and the loading line, desired proportions of tensile and shear stresses were exerted on the bond line. This design was used for both strength and toughness measurements.

MATERIALS SELECTION

Zirconia. Specification of zirconia involved first deciding whether to use one grade for both ceramic/ceramic and ceramic/metal bonds or to tailor the grade to the bond. The choice of a single grade for both bonds provided for the most efficient use of resources in that more effort was devoted to modeling and less to routine material characterization. The magnesia-stabilized grade (Zircoa Zycron L Mg-PSZ) was chosen over a yttria-stabilized grade because it is a more well-established material, a fully-dense ceramic can be more readily produced, and it is easier to machine. It also has good strength and fracture toughness as well as an acceptably low coefficient-of-thermal-expansion mismatch with cast iron.

Nodular Cast Iron. The nodular cast iron (NCI) chosen for this program had a ferritic microstructure, corresponding both to SAE D4018 and to ASTM A536, Grade 60-40-18. The main reason for this choice was that it was the most metallurgically stable grade. It may be noted that significant microstructural changes can occur when NCI is heated to around 760 C, which is only slightly above the temperature range in which brazing is normally carried out. As a result, the mechanical properties of the NCI after brazing can be significantly different from those of the as-received iron and can vary from bond-to-bond, masking the effects of bonding variables and complicating the application of the design model. The major drawback to the chosen grade was that it is weaker than the grade used previously in the Oak Ridge National Laboratories (ORNL) bonding studies (D5506) and much weaker than the one currently being used there (8003).

Zirconia/Zirconia Joint Fabrication. Zirconia/zirconia joints were fabricated using a ceramic interlayer that became molten at the joining temperature. Metallic brazes were rejected due to their limited high-temperature capabilities since the goal was to obtain acceptable strength and toughness of joints at temperatures up to 1000 C. Initially, two ternary eutectic oxides (calcia-titania-silica and calcia-alumina-silica) were evaluated because they become liquid at a bonding temperature of 1420 C where no phase changes were expected in the base zirconia. These eutectic materials proved to be too weak at room temperature, despite good wetting and minimal influence on residual stresses. The eventual choice of interlayer material was magnesia-alumina-silica-zirconia (MASZ) which had acceptable strength and toughness. In order to allow validation of the joint design and assessment methodology over a range of process variables, the composition of the MASZ interlayers was altered by changing the zirconia content.

In addition to fabricating joints with MASZ interlayers, bulk interlayer blocks were fabricated by sintering, and these allowed the determination of thermal expansion coefficients, deformation characteristics, and inherent strength and toughness of bulk MASZ materials.

Zirconia/NCI Joint Fabrication. Brazing of zirconia to NCI was investigated using both the active-substrate and active-filler-metal methods. Attempts to join these materials using the active-substrate brazing method were generally unsuccessful, except when the joint area was small. However, large-area strong bonds were obtained using Incusil-ABA, an active-filler-metal braze (Ag-27.5Cu-12In-1.2Ti), in which the relative amounts of silver, copper, and titanium were nearly the same as produced in the active-substrate brazing

method. In contrast to the active substrate process, no surface coatings were applied to either the zirconia or the NCI in the active filler metal process and no significant voids were observed in the resulting joint.

Joint Scale-up

Although initial fabrication using small joints (2 sq. cm.) with a goal of scaling up to 20 sq. cm. was envisioned, research during the course of the project showed that the larger joints could be fabricated without any additional difficulty. For this reason, the size objective for the joints was achieved.

CHARACTERIZATION AND ANALYSIS OF JOINTS AND MONOLITHIC MATERIALS

Mechanical and thermal characterization of joints, adherents, and interlayer materials were performed. Specifically, stress-versus-strain curves were measured for the zirconia, MASZ interlayer materials, Incusil-ABA, and the cast iron. In the case of the zirconia, stress-strain behavior for both as received material and material heat treated at 1350 C was measured. Thermal expansion curves were obtained over appropriate temperature ranges for each of these materials for use in residual stress calculations. Based on these results and the published literature, estimates were obtained for the flow stress, ultimate tensile strength, elastic modulus, and Poisson's ratio of the adherents as a function of temperature.

Five different specimen types were used to characterize the materials and joints. Unnotched bend specimens were loaded in 4-point bending to determine the bend strength and stress-strain behavior of monolithic materials and specimens containing joints. Notched bend specimens were loaded in 4-point bending to determine the fracture toughness of monolithic materials and specimens containing joints. The notched bend specimens containing joints were used in the preliminary validation procedure. Tensile specimens were used to evaluate the stress-strain behavior of nodular cast iron and Incusil ABA. Uncracked disk specimens were loaded in diametral compression to evaluate the shear strength of zirconia/zirconia joints. Cracked disk specimens were loaded in diametral compression for final validation of the joint design methodology. The disk specimens had bond areas that were approximately 20 times that of the bend bars used in the preliminary validation.

Approximately 160 room temperature tests and 30 high temperature tests were performed to generate material data and validation results. For the zirconia/zirconia joints high temperature tests were performed at 1000 C; for zirconia/NCI joints high temperature tests were performed at 400 C.

Fracture surfaces were examined optically and using a scanning electron microscope. Failure of zirconia/zirconia joints occurred primarily through the ceramic interlayer, although in a few cases the crack also propagated partly through the reaction zone of the base material. The propensity of the crack to propagate through the interlayer provided a good opportunity to predict the failure load of these joints based on the strength and toughness of the bulk interlayer; this was the approach used in failure load predictions. For the zirconia/NCI joints, however, failure occurred partly through the reaction zone of the

zirconia and partly through the Ti interface of the braze-metal/zirconia interface. In this system, the fracture toughness associated with the failure location had to be estimated indirectly.

VALIDATION OF JOINT ASSESSMENT AND DESIGN METHODOLOGY

Two kinds of validation experiments were conducted to compare with the JAD model analyses. Bend bars, both notched and unnotched, were used in preliminary validation experiments. These experiments were conducted to fine tune the model and provide some degree of assurance that the predictions made by the methodology were reasonably accurate. The second type of experiments were termed final validation experiments and were conducted on disk specimens. Because the geometry of the disk specimens was significantly different than that of the bend bars, these experiments provided a challenging validation of the design methodology developed on this program.

In all of the comparisons made between computations and experiments the parameter used for comparison was the failure load. During preliminary validation the model was used to calculate the failure load of notched bend bars fabricated from zirconia/zirconia joints and zirconia/nodular cast iron joints. Final validation computations were made on disk specimens of a similar variety; zirconia/zirconia disks and zirconia/nodular cast iron disks.

For several tests of zirconia/zirconia bend bars with a notch the measured failure loads had an average value of 211 N. The design model predicted a failure load of 260 N. For zirconia/cast iron bend bars an average failure load of 514 N was measured. This compares with a calculated value of 505 N. In an example of a zirconia/zirconia disk with a chevron notch and loaded in compression in line with the joint, the measured failure load was 1442 N while the calculated failure load was 1600 N. A final example is supplied by a metal-ceramic disk loaded in compression with the crack and bond line at an angle of 15 degrees to the load line. The specimen failed at 6631 N and was predicted to be able to withstand 7100 N. The degree of difference between experiment and theory cited in these examples was typical for all of the validation experiments. A master plot comparing measured and predicted failure loads is presented in Section 4.0 Validation.

1.0 CERAMIC OXIDE JOINT DESIGN METHODOLOGY

1.1 JOINT ASSESSMENT AND DESIGN MODEL FORMULATION

In this section a predictive model that can be used in design and structural integrity assessments of ceramic to ceramic and metal to ceramic joints for advanced gas turbine and internal combustion engine applications is developed.

In the modeling effort, the measure of joint performance was taken to be its ability to withstand monotonically applied load. A pragmatic, continuum mechanics-based approach was adopted which links joint performance with joining process variables and physical properties of the constituents. The approach was based on the notion that for a given joint configuration, its ability to withstand load is dictated by strength (σ_c) and toughness (G_c) properties at the potential failure location and the residual stress (σ_R) induced by the joining

process. Physical properties of the joint constituents (ceramic, metal and joining material) and joint process variables (e.g., interlayer thickness and joining temperature) influence joint performance indirectly by changing σ_c, G_c, and σ_R. Also, it was assumed that a micromechanical defect population and distribution associated with a joining process affects joint performance indirectly by changing the apparent strength and toughness properties. The influence of joining area on performance was dealt with empirically by testing specimens with significantly different joint dimensions.

With strength, toughness, and residual stress being the primary factors influencing performance, effort was focussed on developing stress analysis and fracture mechanics based models which would determine the stress field (σ), crack driving force (G) and residual stress (σ_R) for the test specimen geometries shown in Figure 2. Only cracked/notched specimens with crack lengths significantly larger than the interlayer thickness were included in the JAD model calculations. However, the same methodology can easily be extended to macroscopically uncracked geometries, where any crack would typically have dimensions less than the dimensions of the interlayer thickness. As discussed in Appendix A, this modeling effort involved detailed linear and nonlinear finite element analyses whose results were subsequently used to develop simpler and easier-to-use engineering models for estimating σ, G and σ_R. Input to these stress and fracture mechanics models included physical properties of the joint constituent materials as well as two joining process variables-joining temperature (T_J) and interlayer thickness (t_i). The affect of other joining process variables could only be included empirically. For ceramic/ceramic joints, this was done by developing an empirical relation between joining material (MASZ) composition and the interlayer's elastic modulus, yield strength and toughness.

Following the development of engineering models capable of estimating σ, G, and σ_R corresponding to all the loads, specimens and material combinations included in the experimental part of the project, the focus shifted to developing a joint assessment and design model. The objective was to formulate a methodology in which the three primary factors (σ_c, G_c, and σ_R) would be represented in a synergistic and unified manner. This objective was achieved by invoking concepts in engineering nonlinear fracture mechanics[1,2] to derive an expression for a joint assessment vector ($\bar{A}$) as follows:

$$\bar{A} = \left(\frac{G_e}{G_c}\right)^{\frac{1}{2}} i + \left(\frac{P}{P_c}\right) j \qquad (1)$$

in which i and j denote orthogonal unit vectors, P is a load parameter (related to joint stresses due to applied loads and residual stresses) and P_c is the critical load parameter (related to strength, σ_c). The quantity G_e is the elastic crack tip energy release rate for the cracked joint geometry of interest, corresponding to the combined action of residual stresses and applied load. The magnitude of the vector,

$$A = \left[\frac{G_e}{G_c} + \left(\frac{P}{P_c}\right)^2\right]^{\frac{1}{2}} \qquad (2)$$

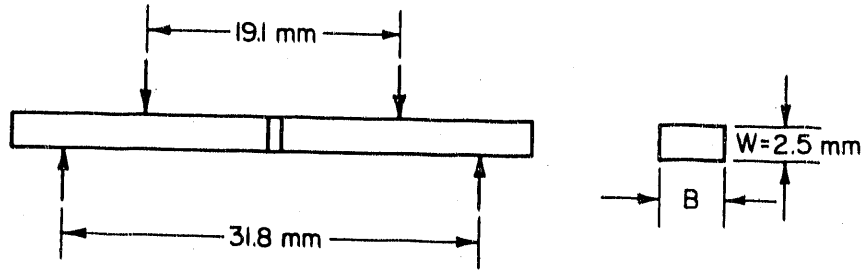

Unnotched Bend Bar, B=5.1 mm

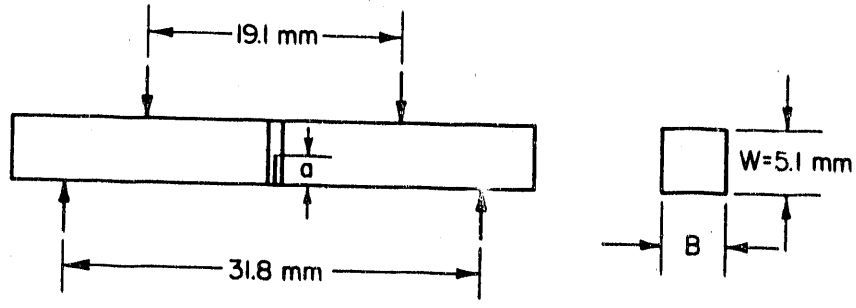

Notched Bend Bar, A/W=0.30 mm, B=5.1 mm

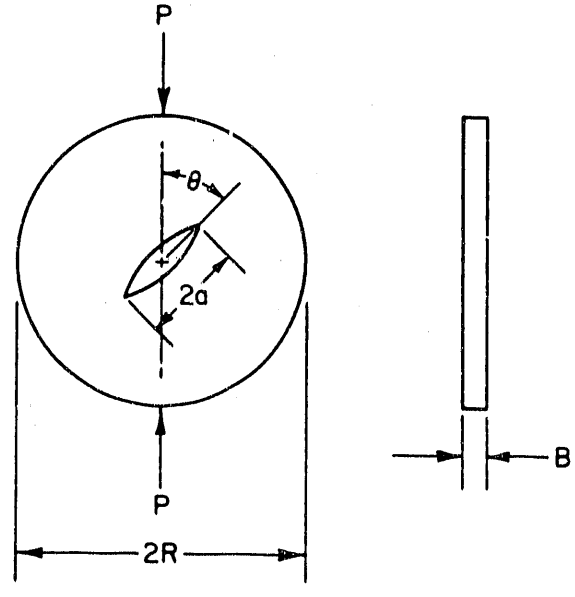

Disk Specimen

Figure 2. Test specimen geometries studied by finite element analysis.

represents the propensity for joint failure in the direction in G-P space given by

$$\phi = \tan^{-1}\left[\frac{\sqrt{G_e/G_c}}{(P/P_c)}\right] \tag{3}$$

The smaller the magnitude of A, the smaller is the propensity for joint failure. For a given joint type and geometry, failure would occur when the vector intersects the following failure curve

$$\sqrt{G_r} = \frac{\sqrt{G_e(a, P_r)}}{G\ (a, P_r)} \tag{4}$$

in which a is crack length dimension, $G_r = G_e/G_c$, $P_r = P/P_c$ and G represents the total (elastic-plastic) energy release rate. Note that equation (4) defines the failure curve and is not the definition of G_r. For $P << P_c$, the plastic deformation contribution to G is small, G approaches G_e, and the right hand side of Equation (4) approaches unity. For P approaching P_c, $G >> G_e$, and the right hand side of Equation (4) approaches zero.

A graphical representation of the assessment vector [Equation (1)] and the failure curve [Equation (4)] is shown in Figure 3. Using the dimensionless quantities G_r and P_r, the assessment vector can be expressed as follows:

$$\bar{A} = (G_r)^{\frac{1}{2}}\, i + (P_r)\, j \tag{5}$$

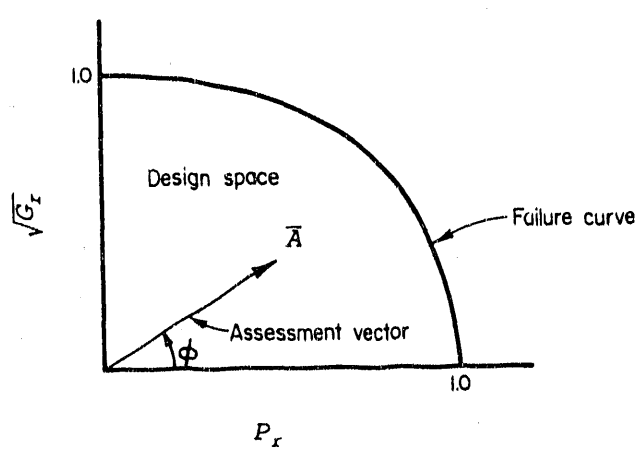

Figure 3. Graphical respresentation of assessment vector and failure curve.

In the graphical representation of the JAD model, the space enclosed by the failure curve (or a fraction thereof) may be defined as the design space within which the assessment vector $\vec{A}$ would be required to reside. At a reference or anticipated service applied load (P_A), one would try to minimize A with respect to joint constituent properties and process variables to improve joint performance. To predict failure, one would find the applied load (P_f) such that the vector $\vec{A}$ intersects the failure curve. Thus, for failure prediction one needs both the failure curve [Equation (4)] and the assessment vector [Equation (5)]. For improving design, only the assessment vector is needed.

For joint design one needs to specify a reference load (P_A) which is used to find the total load, P, on the joint

$$P = P_A + P_R \tag{6}$$

in the evaluation of A. In Equation (6), P_R represents a load parameter due to residual stress in the joint. From a practical viewpoint P_A should be chosen such that $P_R << P_A < (S_F \cdot P_f)$ where S_F is a safety factor and P_f is the failure load. For the present work, we choose P_A to be the minimum of the failure loads corresponding to a monolithic specimen of the materials being joined. For example, in designing a nodular cast iron/zirconia bend bar joint, P_A would be the failure load corresponding to a monolithic zirconia bend bar of the same dimensions and subjected to the same type of loading, knowing that the failure load corresponding to a cast iron bend bar would be higher. This particular choice of P_A is, of course, not mandatory. But it may have practical significance if it is argued that a component containing a joint need not withstand any more load than a monolithic component of either of the two materials being joined.

Based on the stress and fracture mechanics engineering models mentioned earlier, expressions for A and $\sqrt{G_r}$ for the four joint types and specimen geometry combinations are given in the following paragraphs. Details and justifications for the assumptions involved in their derivation are given in Appendix A.

1.2 ZIRCONIA/ZIRCONIA BEND SPECIMEN

For cracked zirconia/zirconia bend specimens, the failure curve is given by the following equation:

$$\sqrt{G_r} = \frac{\pi f g}{2\sqrt{2}} P_r \left[\ln \left\{ \sec \left(\frac{\pi}{2} \cdot f \cdot g \cdot P_r \right) \right\} \right]^{-\frac{1}{2}} \tag{7}$$

where

$$g = 1 - \sqrt{P_r} + \frac{P_r}{f} \tag{8}$$

The assessment vector for this specimen type (for $P_R << P_c$) is given by the following equation:

$$\overline{A} = \left[\frac{3f(S-L)P}{2W^2t} \left(\frac{\pi a}{E_1' G_{c1}} \right)^{\frac{1}{2}} \right] i + P_r j \tag{9}$$

In Equations (7), (8), and (9)

$$E_1' = E_1/(1-\nu_1^2) \tag{10}$$

$$f = f_H \cdot f_s \tag{11}$$

$$f_H = 1.12 - 1.39\,\overline{a} + 7.32\,\overline{a}^2 - 13.1\,\overline{a}^3 + 14.0\,\overline{a}^4 \tag{12}$$

$$\overline{a} = a/W \tag{13}$$

$$f_s = 1.0 + \left(0.376 + 2.34\,\frac{t_1}{2a}\right)\left(1 - \frac{\mu_1}{\mu_c}\right) - \left(2.504 + 3.87\,\frac{t_1}{2a}\right)\left(1 - \frac{\mu_1}{\mu_c}\right)^2 \tag{14}$$

$$P_r = P_A \frac{1.5\,(S-L)\,\overline{\sigma}}{W^2 t\,\sigma_{o1}} \tag{15}$$

$$P_A = \frac{W^2 t}{1.5\,(S-L)\,f_H} \left(\frac{G_{cc}\,E_c'}{\pi\,a} \right)^{\frac{1}{2}} \tag{16}$$

$$P = P_A + \frac{2\,W^2 t\,F_R\,\sigma_{RT}}{3\,(S-L)\,f} \tag{17}$$

$$\bar{\sigma} = 1.0 + \left(\frac{ti}{w}\right)\left(1 - \frac{\mu_i}{\mu_c}\right)\left[177\,\frac{ti}{w} - 10.9\right] \tag{18}$$

$$F_R = \frac{f_R}{\pi\bar{a}} - f_R' \tag{19}$$

$$f_R = \frac{3.52}{(1-\bar{a})^{\frac{3}{2}}} - \frac{4.35}{(1-\bar{a})^{\frac{1}{2}}} + 2.13\,(1-\bar{a}) \tag{20}$$

$$f_R' = 0.265(1-\bar{a})^4 + \frac{0.857 + 0.265\,(\bar{a})}{(1-\bar{a})^{\frac{3}{2}}} \tag{21}$$

The symbols ν, μ, E, and σ_o represent Poisson's Ratio, the shear modulus, Young's Modulus and yield strength, respectively, with subscripts i and c denoting interlayer (MASZ) and ceramic (zirconia) materials. Geometric dimensions (a, W, t, S, L. and t_i) used in Equations (9) to (21) are shown in Figure 2. In Equations (11) and (14) the term f_s is a shielding factor and accounts for modulus mismatch effects on joint stresses. The word "shielding", in this context, has ben coined because the interlayers used in this investigation (as well as in most other ceramic joining processes) had lower moduli than the adherents, and acted to reduce the local stresses and crack driving forces compared with corresponding values calculated based on a homogeneous material. The quantity σ_{RT} is related to the residual stress across the bond line which occurs close to the specimen edges. At the ceramic-interlayer interface,

$$\sigma_{RT} = \frac{2\,t_i\,\sigma_t\,(\lambda-1)}{\lambda\,(W-2t_i)}\left[\left(\frac{\sigma_t}{\sigma_Y + \sigma_t}\right)^{\frac{\lambda}{1-\lambda}} - 1\right] \tag{22}$$

where

$$\sigma_t = \left| \frac{E_i'\,E_c'}{E_i' + E_c'}\left[(1+\nu_i)\,\alpha_i - (1+\nu_c)\,\alpha_c\right]\cdot\Delta T \right| \tag{23}$$

ΔT = Difference between joining temperature (T_j) and test temperature (T_t)

σ_Y = minimum of σ_{oi} and σ_{oo}

$\alpha_{i,c}$ = coefficients of linear thermal expansion corresponding to interlayer (i) and ceramic (c)

λ = 1.0 + power of thermal stress singularity at the specimen edge. For a zirconia/zirconia joint with an MASZ interlayer, λ =0.97.

For the parameters given in the third line of Table 1, a graphical representation of the JAD model application to a zirconia/zirconia bend bar joint is shown in Figure 4. The reference load, which is much higher than the predicted and measured failure load for the joint, is the load which would be needed to cause fracture in a geometrically identical monolithic specimen made of zirconia. The predicted failure load corresponds to the intersection of the vector with the curve at P/P_o = 0.493, and is somewhat lower than the measured value of 260N. To improve joint design one would need to increase G_{ci} and σ_{oi} (e.g. by increasing zirconia content in the interlayer material) which would reduce the assessment vector length. As discussed later in the report, empirical relations between σ_{oi}, G_{ci}, E_i and volume percent (V) of zirconia in the interlayer material (MASZ) are as follows:

σ_{oi}	=	41.4 + 2.35 (V-50)	MPa	
E_i	=	109 + 0.1588 (V-50)	GPa	$50 \le V < 67$
G_{ci}	=	$[1.52 + 0.03 (V-50)]^2/10^3 E_i$	N/m	
σ_{oi}	=	74.0 + 2.13 (V-67)	MPa	
E_i	=	111.7 + 2.2692 (V-67)	GPa	$67 \le V < 80$
G_{ci}	=	$[2.04 + 0.06 (V-67)]^2/10^3 E_i$	N/m	
σ_{oi}	=	101.7 + 1.95 (V-80)	MPa	
E_i	=	141.2 + 3.04 (V-80)	GPa	$80 \le V$
G_{ci}	=	$[2.82 + 0.0125 (v-80)]^2/10^3 E_i$	N/m	

As an example, using 80 percent zirconia (instead of 67 percent) would reduce the assessment vector length by approximately 37 percent. Further reduction may also be effected by reducing interlayer thickness of the joint.

Table 1. Parameters used in assessment diagram calculations.

Joint Type	Joining Temp., C	Width Meters	Thickness Meters	Notch Depth Meters	Radius Meters	Theta Degrees	MASZ Percent
ZrO_2/Iron Bend Bar	700	.00508	.00508	.001600			
ZrO_2/Iron Disk	700		.00363	.000825	.00178	10.00	
ZrO_2/ZrO_2 Bend Bar	1350	.00508	.00580	.001549			67
ZrO_2/ZrO_2 Disk	1350		.00363	.008250	.01780	0.00	80

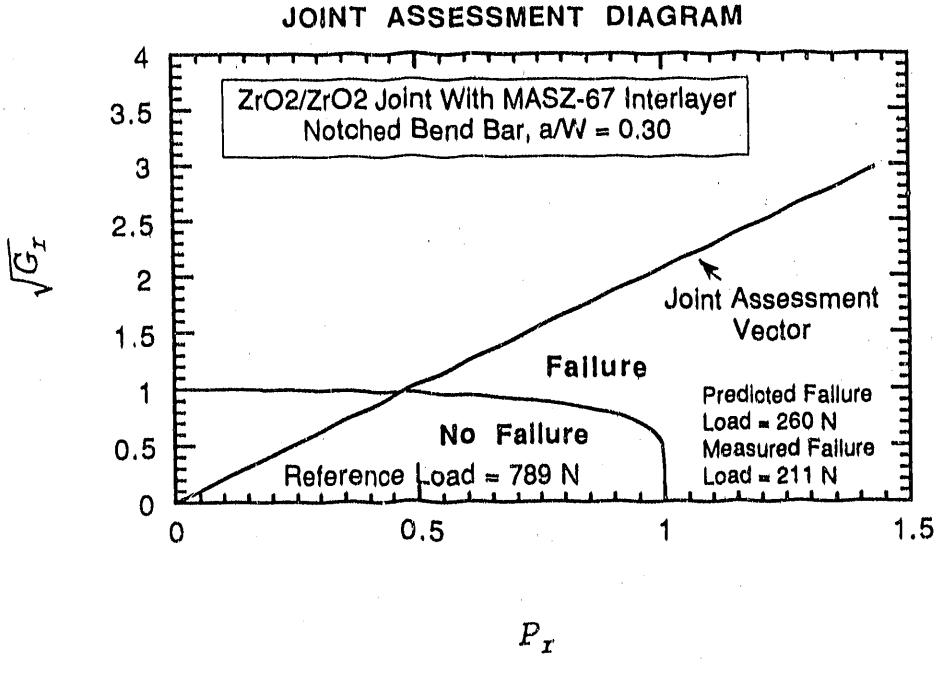

Figure 4. Assessment diagram for zirconia/zirconia bend specimen.

1.3 ZIRCONIA/NODULAR CAST IRON BEND SPECIMEN

For ceramic/metal bend specimens (with appropriate material property changes) all the equations from (7) to (23), with the exception of Equations (14) and (18), still apply. The dimensionless quantities f_s and $\bar{\sigma}$ are now redefined as:

$$f_s = 0.4766 + 1.0468 \left(\frac{\mu_d}{\mu_m + \mu_c} \right) \tag{24}$$

$$\bar{\sigma} = \left\{1.0 + \frac{t_1}{W}\left(1 - \frac{2\,\mu_1}{\mu_m + \mu_c}\right)\left[177\,\frac{t_1}{W} - 10.9\right]\right\} \cdot \left[0.98 + \beta\left(\frac{2x}{t_1}\right) + \gamma\left(\frac{2x}{t_1}\right)^2\right] \tag{25}$$

where $\beta = 0.0389$, $\gamma = 0.0949$, and x denotes the distance from the center of the interlayer to the crack location. For the cast iron/zirconia joints in the present program, the crack location was at the ceramic-interlayer interface. Thus, $x = t_1/2$. As before μ represents shear modulus and subscript m represents metal (cast iron).

For the parameters given in Table 1, a graphical representation of the JAD model application to a metal-ceramic bend specimen geometry is shown in Figure 5.

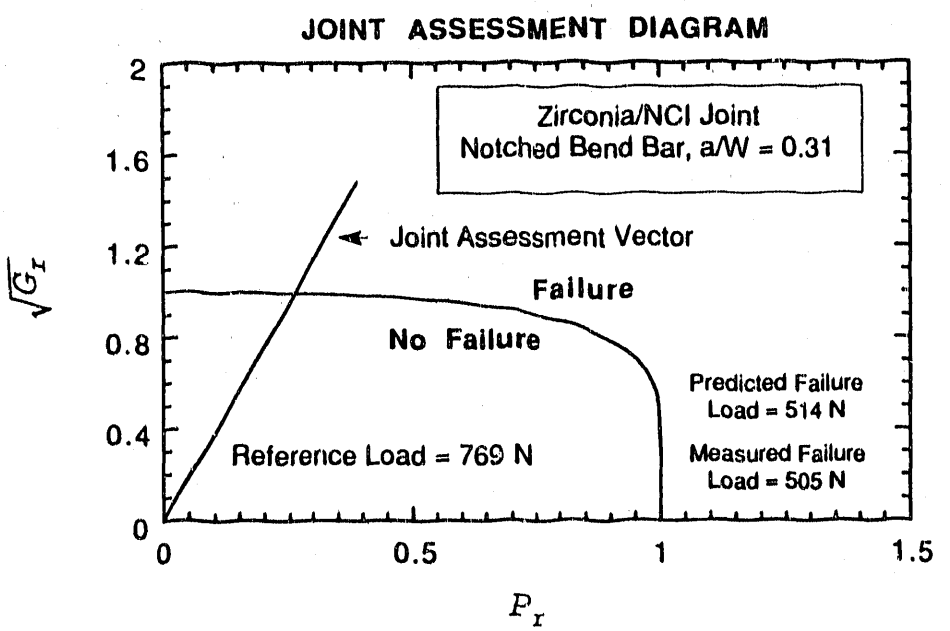

Figure 5. Assessment diagram for zirconia/cast iron bend specimen.

1.4 ZIRCONIA/ZIRCONIA DISK SPECIMEN

For a zirconia/zirconia disk specimen with load angle θ between the bond line and load line in the range $0.0 \le \theta \le 22.5$ degrees and $a/R = 0.5$ the failure curve is given by the following equation

$$\sqrt{G_r} = \frac{\pi\, f\, g}{2\sqrt{2}}\, P_r \left[\ln\left\{\sec\left(\frac{\pi}{2}\, f\, g\, P_r\right)\right\}\right]^{-\frac{1}{2}} \tag{26}$$

where

$$g = 1 - \sqrt{P_r} + \frac{P_r}{f} \tag{27}$$

The assessment vector for this specimen type (for $P_R << P_c$) is given by the following equation

$$\bar{A} = \left[\frac{f\,P}{Rt} \left(\frac{a}{\pi\, E_1'\, G_{c1}} \right)^{\frac{1}{2}} \right] i + P_r\, j \tag{29}$$

In Equations (26), (27), and (29)

$$f = f_H \cdot f_s \tag{30}$$

$$f_H = 62.755 - 43.316 \sin\theta - 65.257 \cos\theta + \\ + 21.883 \sin 2\theta + 4.485 \cos 2\theta \tag{31}$$

$$f_s = (\cos^2\theta) \cdot \\ \cdot \left[\frac{\mu_1\,(1-\nu_c)}{\mu_c(1-\nu_1)} \left\{ 1.0 - 0.224 \left(1 - \frac{\mu_1}{\mu_c} \right) + 0.375 \left(1 - \frac{\mu_1}{\mu_c} \right)^2 \right\} \right]^{\frac{1}{2}} \tag{32}$$

$$P_r = P_A\, \bar{\sigma} / (\pi\, R\, t\, \sigma_{o1}) \tag{33}$$

$$P_A = \frac{Rt}{f_H} \left[\frac{\pi\, E_c\, G_{cc}}{(1-\nu_c^2)\, a} \right]^{\frac{1}{2}} \tag{34}$$

$$P = P_A - \pi R t \sigma_{RT} \tag{35}$$

The quantity σ_{RT} is the same as defined in Equations (23) and (24), and for the disk specimen, the dimensionless quantity $\bar{\sigma}$ appearing in Equation (33) is approximately unity.

For the parameters given in Table 1, a graphical representation of the JAD model application to a zirconia/zirconia disk specimen geometry is shown in Figure 6.

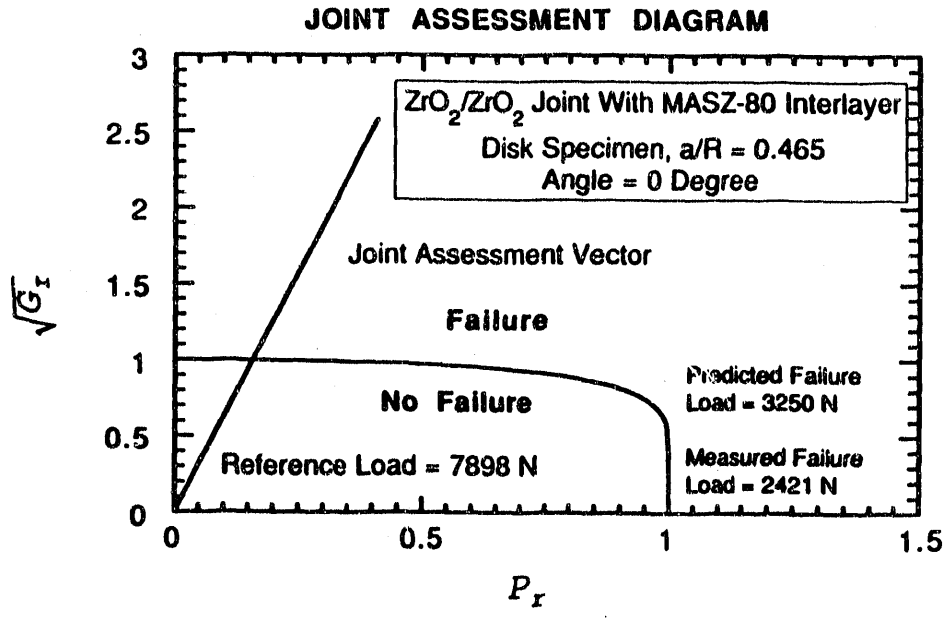

Figure 6. Assessment diagram for zirconia/zirconia disk specimen.

1.5 ZIRCONIA/NODULAR CAST IRON DISK SPECIMEN

For a zirconia/nodular cast iron disk specimen with load angle θ in the range $0.0 \le \theta \le 22.5$ degrees and a/R = 0.5, the failure curve and assessment vector are given by Equations (26) to (30). The dimensionless quantities f_H and f_s are for this case defined as follows:

$$f_H = [62.493 - 42.935 \sin\theta - 65.112 \cos\theta + 21.765 \sin 2\theta + 4.587 \cos 2\theta]^{\frac{1}{2}} \tag{36}$$

$$f_s = \left[0.4766 + 1.0468 \left(\frac{\mu_i}{\mu_m + \mu_c}\right)\right] \cos^2\theta \tag{37}$$

Equations (33), (34), and (35) remain applicable to metal-ceramic disk specimens with $\bar{\sigma} = 1.0$ and σ_{RT} defined by Equations (23) and (24).

For the parameters given in Table 1, a graphical representation of the JAD model application to a cast iron/zirconia disk specimen geometry is shown in Figure 7.

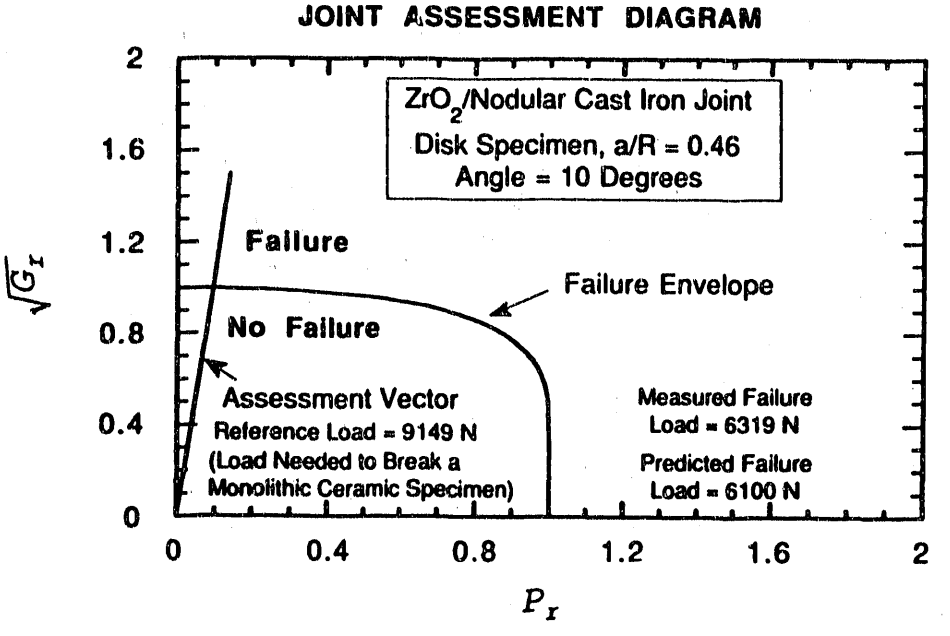

Figure 7. Assessment diagram for zirconia/cast iron disk specimen.

1.6 DISCUSSION OF THE JAD MODEL

The JAD model developed in the present work represents an attempt to provide a link between the structural performance of ceramic/ceramic and metal/ceramic joints with the fracture, mechanical and thermal expansion properties of the joint constituents (ceramic, metal and interlayer). For the materials and joint geometries selected for material property data generation and model validation, the JAD model was found to provide reasonably accurate results. The bend bar and disk specimens tested in the project represent significantly different geometries, giving rise to widely different stress distributions across the joint. The fact that the model provided reasonably good results for both geometries and for both material bonds, suggests that the modeling approach may provide a useful tool for design and assessment of joints.

While model validation was performed on only bend bar and disk (with varying load angles) specimens, the modeling approach adopted in the present work is quite general. It can be readily extended to other joint configurations as well as other material combinations. To do so, one would need to find (probably numerically) appropriate expressions for G_e, G, and P_r appearing in Equations (4) and (5) for the failure curve and assessment vector. If it is found (by numerical analysis of other material and geometry combinations) that the equation for the failure curve [see Equations (7) and (26)] is a reasonably good representation for other geometries as well, one would need to find only the dimensionless factors f and g for the new geometry and material. Figure 8 shows the variation in the failure curve shape using the extreme values of f [with g as defined by Equation (8)] encountered in the present work. The smaller value of f corresponds to a bend specimen and the larger value

corresponds to a disk specimen with load angle (θ) of 22.5 degrees. The figure suggests that the failure curve shape does not change drastically by varying f. Thus, for other geometries a fixed value of f (say, f = 1.0) may be appropriate. If both f and g are taken to be unity, the curve shape, also shown in Figure 8, becomes specimen geometry independent.

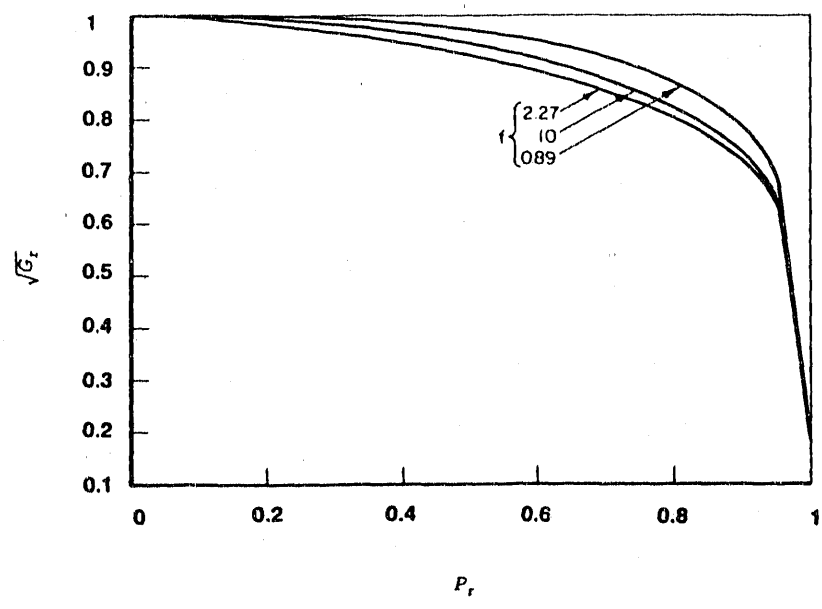

Figure 8. Variation in failure curve shape.

From a design view point, it is desirable that joining process variables (and not only constituent material properties) can also be linked to joint performance. Two of the process variables (joining temperature and interlayer thickness) are directly represented in the JAD model. For ceramic/ceramic joints with an MASZ interlayer, the zirconia content in the MASZ is also included in the model using empirical relations between percent zirconia and E_i, σ_{oi}, and G_{ci}, as discussed in Section 3.0 Characterization and Analysis of Joints and Monolithic Materials.

The JAD model has been programmed in BASIC for use on an IBM- compatible personal computer. Instructions for obtaining a copy of the code can be found in Appendix D. The code (which contains the material property data base generated in the present project) represents a first step toward a potentially much more general and useful design tool for ceramic/ceramic and ceramic metal joints. A more general code would encompass a wider range of geometry configurations, material combinations, joining methods and service load and environmental conditions.

2.0 JOINT FABRICATION

Figure 9 summarizes the joint types and fabrication techniques used in this investigation. The adherents were magnesia partially stabilized zirconia and nodular cast iron. Small scale joints with bond areas approximately 12.5 mm x 12.5 mm were used for preliminary screening of the joining techniques. Later, large scale joints were fabricated using disks 51 mm in diameter and 19 mm thick and joining them along their flat faces. Mechanical test specimens used for preliminary and final validation were machined from these large scale joints. As illustrated in Figure 9 a number of techniques were tried for fabricating zirconia/zirconia and zirconia/NCI joint. Among these, the magnesia-alumina-silica-zirconia system was selected for fabricating zirconia/zirconia joints for validation testing. The active filler metal approach was finally selected for joining zirconia and cast iron. The details of material selection and fabrication techniques are discussed in the paragraphs that follow.

2.1 MATERIALS SELECTION

2.1.1 Zirconia

Type Zycron-L magnesia partially stabilized zirconia (PSZ) was purchased from Zircoa Products, Inc.. This grade was selected to obtain optimal strength and toughness up to temperatures of 400 C. It is chemically inert to molten metals, minimizing hot corrosion problems during brazing. Finally, a good thermal-expansion match to nodular cast iron minimizes residual stresses and a good elastic-modulus match minimizes interface stresses under load. Two other types of zirconia were used in the development stages of the joining process. These included an yttria zirconia which was fabricated by vacuum hot pressing at Ohio State and a magnesia zirconia, Nielsen grade MS, with an electron-beam PVC titanium coating supplied by ORNL. However, all of the joints used in validation testing were fabricated using the Zircoa Zycron-L material.

2.1.2 Nodular Cast Iron

A piece of nodular cast iron measuring 203 mm x 203 mm x 25 mm was supplied by Sandia National Laboratory and used in metal/ceramic joints. The material is of ferritic microstructure and close to SAE D4018 (equivalent to ASTM A536, Grade 60-40-18).[a] However, it is weaker than the grade used previously in the ORNL bonding studies (D5506) and much weaker than the one currently being used there (8003).

(a) The SAE designation code for nodular iron is DXXOO, where XX = Yield Strength and oo = Elongation.

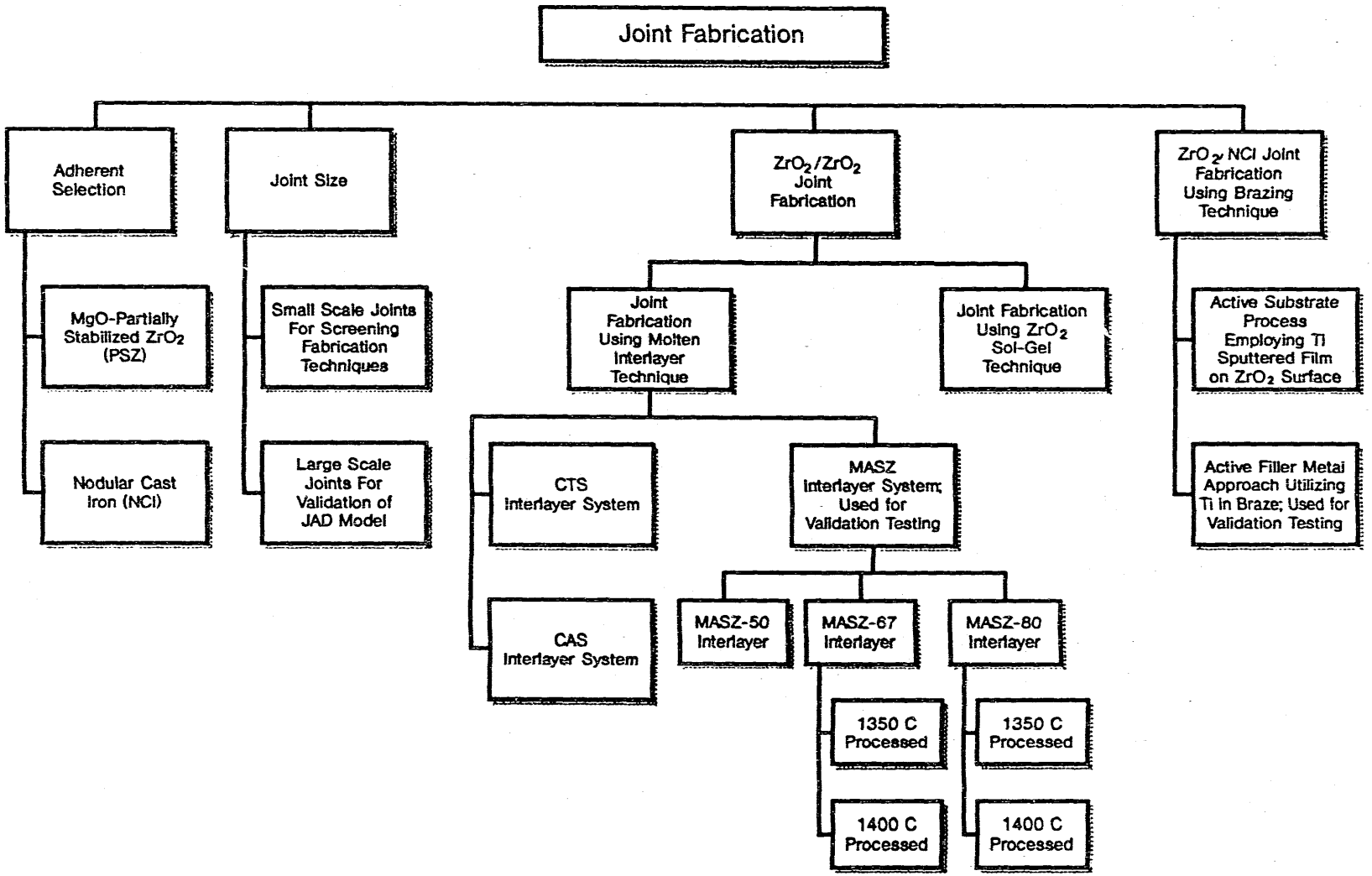

Figure 9. Summary of joint types and fabrication techniques.

The reasons for choosing this material were:

1. It has the most stable microstructure in this alloy system. Significant metallurgical changes can occur when these alloys are heated to around 760 C, which is only slightly above the temperature range in which brazing is normally carried out. As a result, there is concern that the mechanical properties of the iron after brazing will not only be significantly different from those of the as-received material, but also will vary from bond-to-bond, which would mask the effects of bonding variables. To compound the problem, some of the physical properties become erratic when these changes occur, complicating the model verification. Therefore, use of the ferritic material was expected to minimize problems associated with possible phase and microstructural changes.

2. The physical and mechanical properties of this grade of nodular cast iron have been characterized in great detail. For example, Sandia is doing extensive work on the same block that was used in this investigation.

2.2 ZIRCONIA/ZIRCONIA JOINTS

A literature survey indicated that there was no established technique that provided zirconia/zirconia joints of acceptable strengths at temperatures up to 1000 C. A brazing technique was ruled out because the braze metal is molten below that temperature. Accordingly, various ceramic interlayers were evaluated for joining zirconia to itself. Results on experiments performed with various interlayer materials are discussed below and also in the papers[3, 4, 5] provided in Appendix B.

2.2.1 Sol-gel Zirconia Interlayer

The use of a zirconia interlayer would be ideal because the thermal expansion match would be good and because of the inherent strength of zirconia ceramics. However, a bond could be formed with a zirconia interlayer only through solid-state diffusion. It was felt that this would be possible with a highly reactive, fine-particle-size zirconia powder produced by sol-gel processing. A sol-gel method for the preparation of an MgO-doped zirconia powder was developed. This powder was used as an interlayer for a joining experiment with 12.5 mm diameter zirconia disks. The zirconia powder was dispersed in methanol and applied to the mating faces. Sintering of the zirconia sandwich in air at a temperature of 1500 C resulted in a bond that survived several drop-tests before failing. Observation of the fracture surface indicated that the bond was porous and that the interlayer exhibited lateral shrinkage during sintering. It was clear that the application of pressure during bonding would be required for a sol-gel zirconia interlayer to be effective for joining.

An air-ambient hot-forging apparatus was built at Battelle for this program, and two joining experiments were performed with the sol-gel zirconia interlayer. In the first experiment, two 12.5 mm diameter zirconia disks were joined by the application of 13.8 MPa at a temperature of 1600 C. A good bond was formed although the specimen size was too small for a bond strength measurement. Optical micrographs (Figure 10) showed that the as-formed bond region was very dense, although some porous regions were present. A bonding experiment was then repeated using 51 mm diameter zirconia billets.

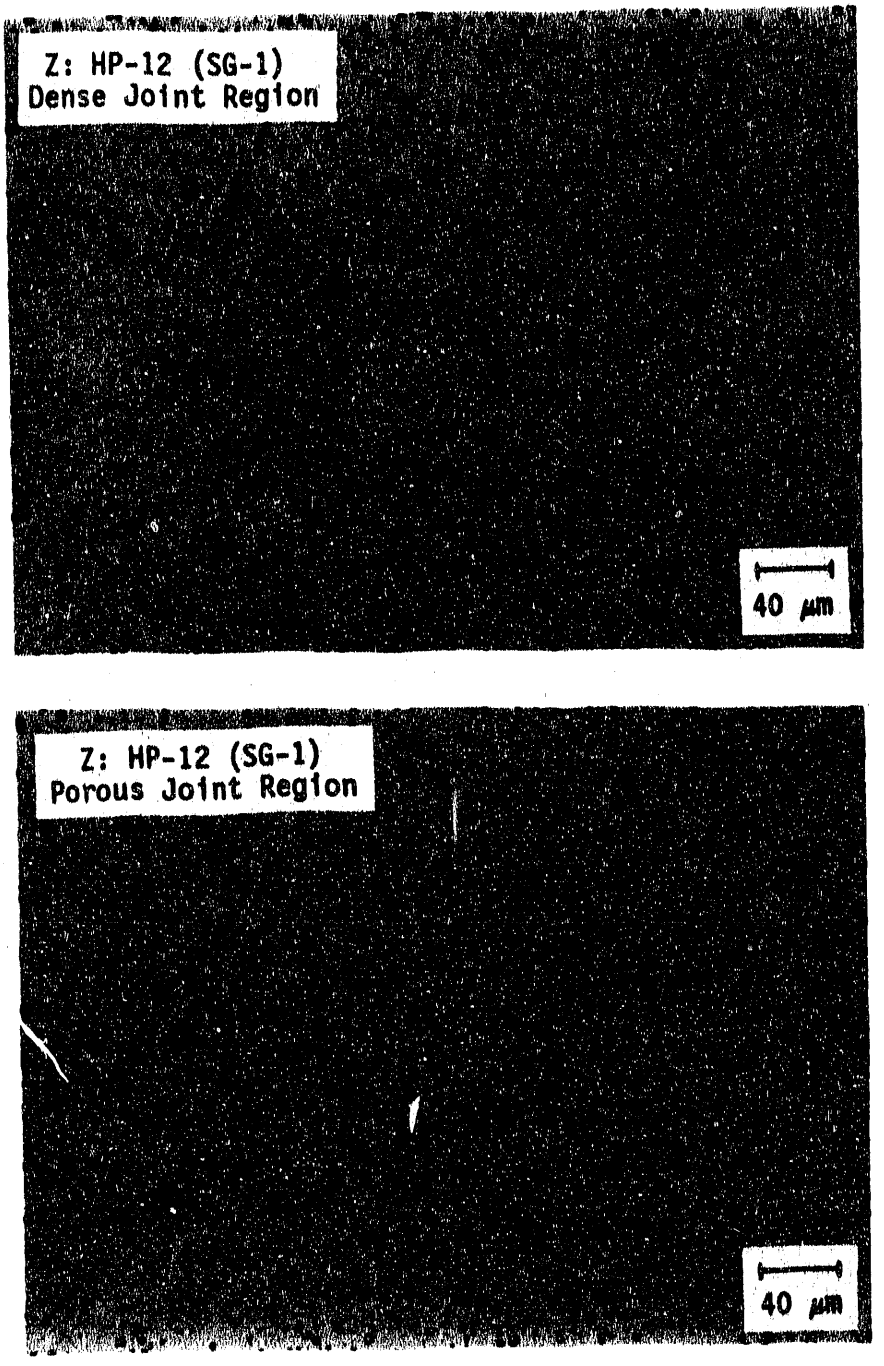

Figure 10. Optical micrographs of zirconia joint produced by hot-forging at 1600 C with a sol-gel zirconia interlayer. Both dense (top) and porour (bottom) joint regions are shown.

Unfortunately, this experiment ended in catastrophic failure of the alumina forging rams. It became clear that hot forging was a promising approach but that lower joining temperatures were required.

2.2.2 CTS and CAS Interlayers

The use of Battelle's air-ambient hot-forging apparatus for joining zirconia ceramics was limited to below about 1450 C. Since solid-state diffusional bonding with zirconia interlayers was not feasible at these low temperatures, a molten interlayer technique was considered to reduce the bonding temperatures for hot-forging. A temperature of 1420 C was selected as the bonding temperature, because it was thought that this temperature would minimize degradation of the base zirconia material (although this assumption was not evaluated). Two possible molten-interlayer systems were identified by searching through various phase diagrams. These were the CaO-TiO_2-SiO_2 (CTS) and CaO-Al_2O_3-SiO_2 (CAS) systems, each of which has eutectic compositions below 1400 C.

Interlayer powders of three CTS compositions and three CAS compositions were prepared by milling the oxide/carbonate raw materials, followed by calcination at 1100 C, and sieving to below 200 mesh. Compositions of CTS and CAS interlayer powders are given in Tables 2 and 3, respectively. Both small-scale (15 mm diameter disks) and large-scale (51 mm diameter disks) joining experiments were performed. Interlayers were applied to the zirconia disks through a methanol slurry, and disks were joined by hot-forging at 1420 C under pressures of 3.4 to 13.8 MPa. Both CTS and CAS interlayers provided successful small-scale bonds. Optical micrographs of small-scale zirconia joints produced with CTS and CAS interlayers are provided in Figures 11 and 12, respectively. Scale-up problems were encountered, related to thermal expansion mismatch and to "squeeze-out" of the interlayer material during hot forging. This was addressed by adding 30 wt% zirconia powder to the CAS and CTS interlayer material. The zirconia powder increased the viscosity of the interlayer during hot-forging, thus preventing "squeeze out", and also provided for a better expansion match between the interlayer and the zirconia base material. The best large-scale joint was produced by hot-forging with the CTS-3 interlayer composition, containing 30 weight percent zirconia. The average joint strength (four-point bending) was 67 MPA, with a Weibull modulus of 6.1. An optical micrograph of this joint, and an SEM micrograph of the fractured surface of a bend-test specimen, are shown in Figure 13.

Electron microprobe results obtained during initial CTS joining experiments were published[3]. Additional work describing zirconia joints formed using interlayers in both CTS and CAS systems was also published[4]. These two papers are reproduced in Appendix B.

Table 2. $CaO-TiO_2-Sio_2$ (CTS) interlayer compositions.

	Composition (wt%)				
	CaO	TiO_2	SiO_2	ZrO_2	Comments
CTS-1	35.0	50.0	15.0		Tm = 1372 C (DTA)
CTS-2	25.0	57.0	18.0		eutectic composition Tm = 1356 C (DTA)
CTS-3	17.5	39.9	12.6	30.0	70 wt% CTS-2 + 30 wt% Zro2 Tm = 1357 C (DTA)

Table 3. $CaO-Al_2O_3-SiO_2$ (CAS) Interlayer compositions.

	Composition (wt%)				
	CaO	Al_2O_3	SiO_2	ZrO_2	Comments
CAS-4	49.7	43.4	7.0		eutectic composition Tm = 1323 C (DTA) α = 8.4 ppm/C
CAS-5	41.0	11.8	47.2		eutectic composition Tm = 1308 C (DTA) α = 8.9 ppm/C
CAS-6	28.7	8.3	33.0	30.0	70 wt% CAS-5 + 30 wt% Zro2

2.2.3 MASZ Interlayers

The low joint strengths achieved in the CTS and CAS systems required consideration of alternative molten-interlayer materials. One possibility was the use of a glass-ceramic material that was molten during joining but would crystallize, providing high strength to the joint, during cooling. Glass-ceramics in the $MgO-Al_2O_3-SiO_2$ (MAS) system are used for certain structural applications, and Battelle's experience with these materials suggested reasonable high-temperature (1000 C) strength. One such glass-ceramic material is Zircoa 9606 glass-ceramic, which contains MgO, Al_2O_3, SiO_2, and TiO_2 (MAST). An initial, rather

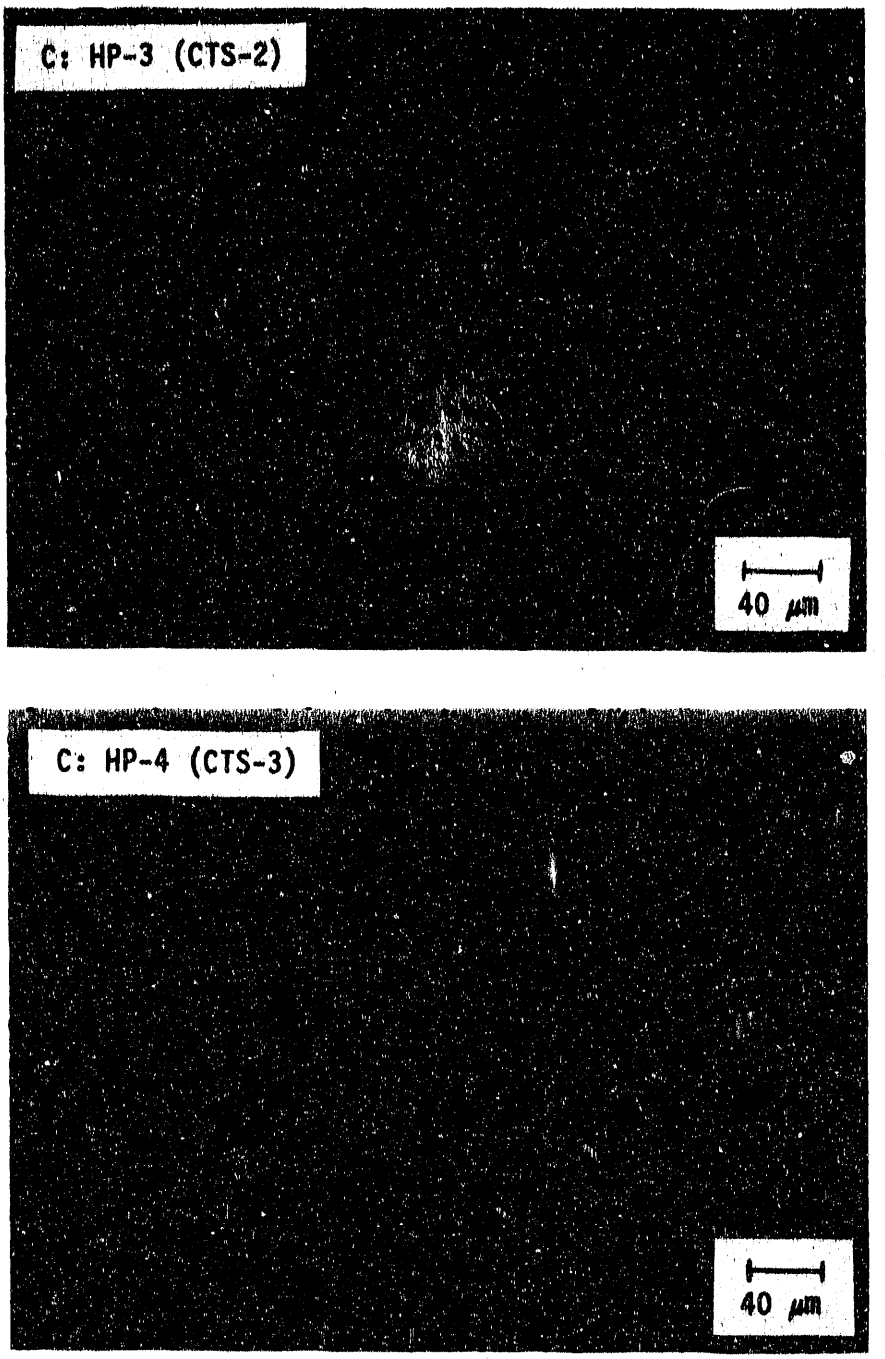

Figure 11. Optical micrographs of small scale zirconia joints produced by hot-forging with calcia-titania-silica CTS interlayers.

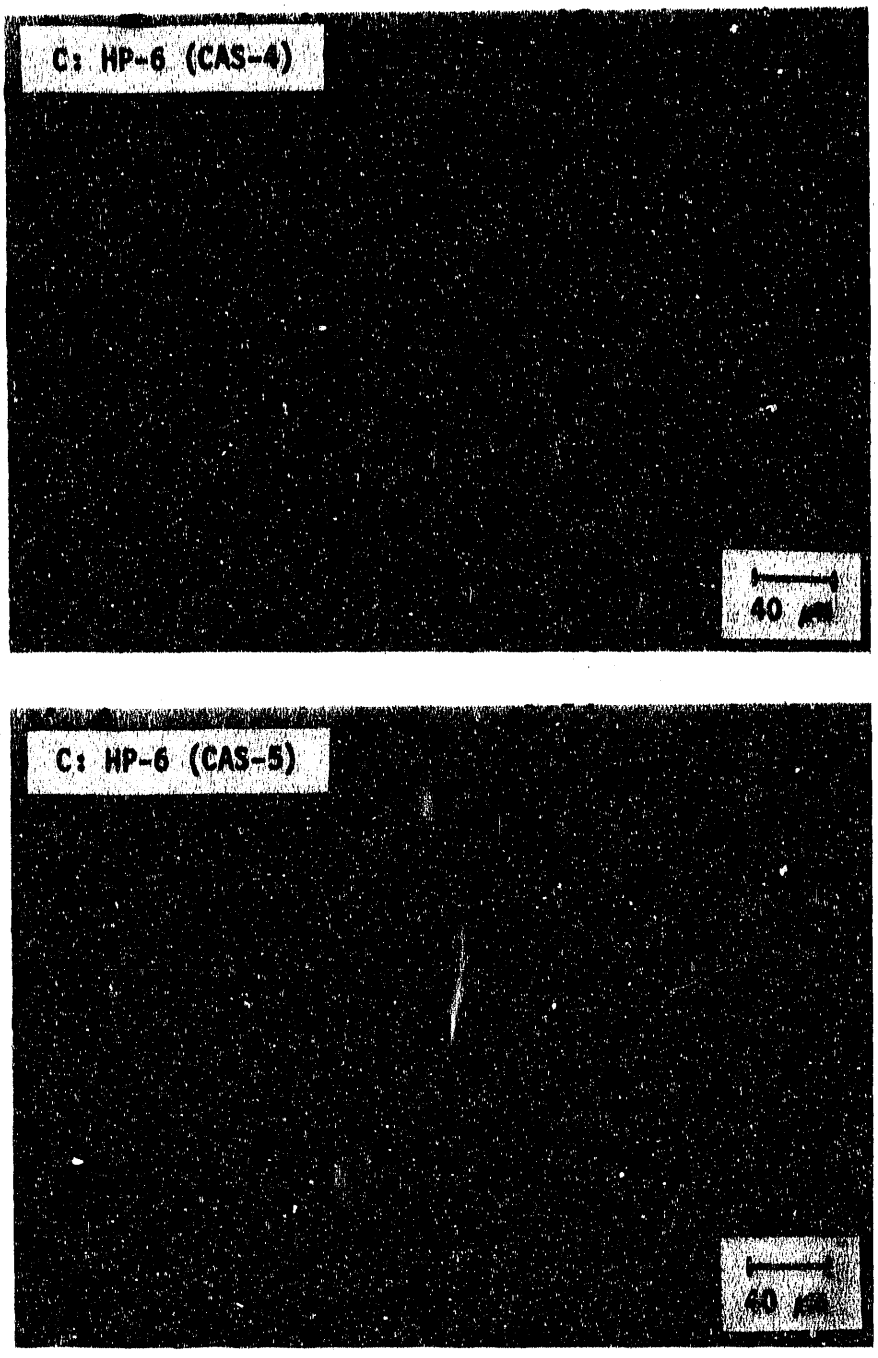

Figure 12. Optical micrographs of small scale zirconia joints produced by hot-forging with calcia-alumina-silica (CAS) interlayers.

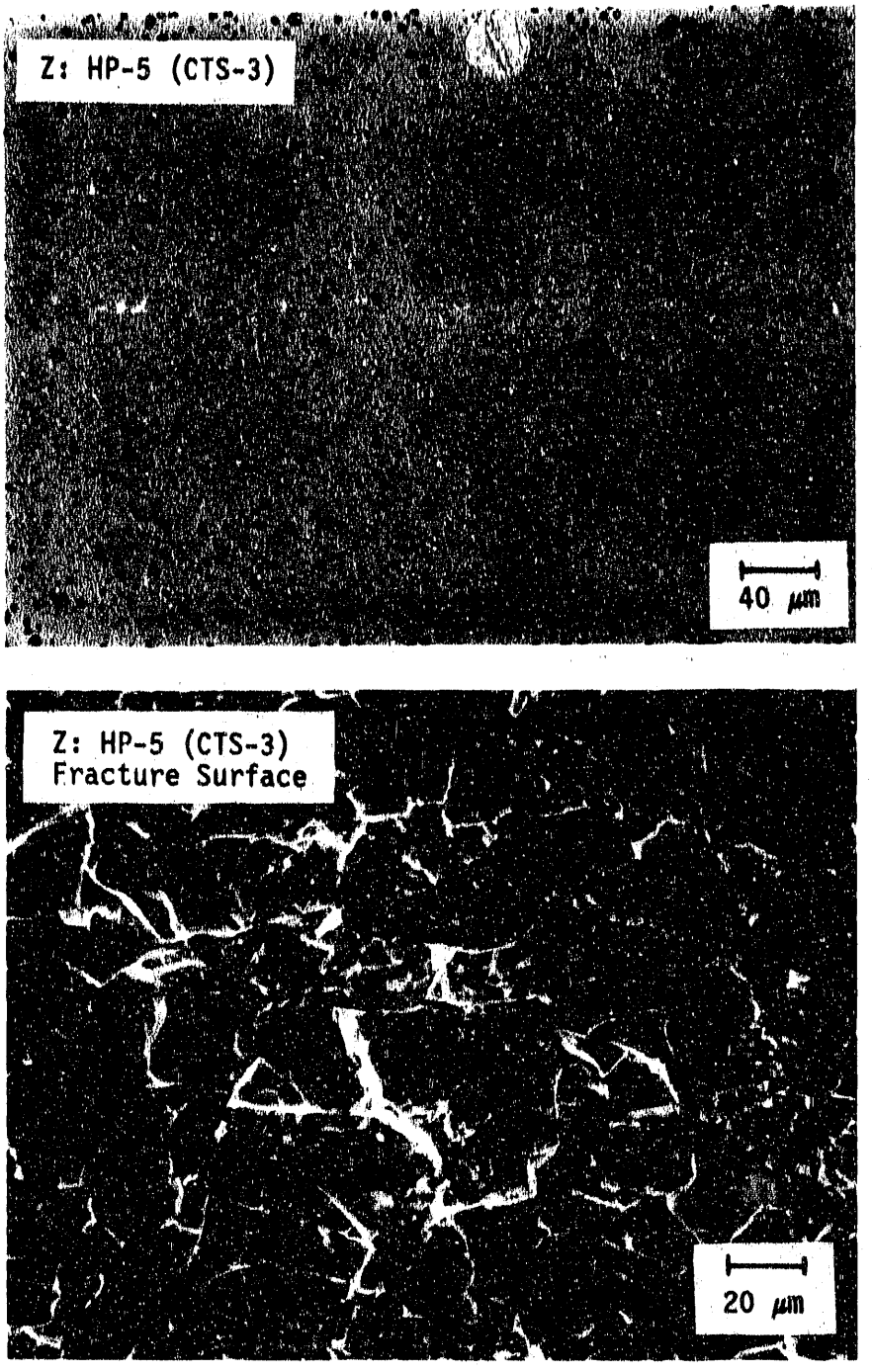

Figure 13. Top: Optical micrograph of large scale zirconia joint produced by hot-forging with the CTS-3 interlayer composition. Bottom: SEM micrograph of the fractured surface of a bend-test specimen produced from the above joint.

crude experiment was conducted to determine whether this material would be useful for joining. Some 9606 glass-ceramic material was crushed into a powder and applied as an interlayer between two pieces of zirconia, which were then heated (without pressure) to a temperature of 1300 C. The two pieces stuck together and survived drop tests.

More controlled joining experiments then were conducted with MAS interlayer powders with the 9606 glass-ceramic composition. Initial experiments with crushed 9606 glass-ceramic powder gave similar results to interlayer powders produced by milling and calcination at 1100 C. The use of MAST interlayers reduced the joining temperature to the range of 1320 to 1365 C. The best joining results were obtained when large amounts of zirconia powder (up to 80 weight percent) were added to the MAS interlayer powder. The family of magnesia-alumina-silica-zirconia interlayers are henceforth referred to as MASZ interlayers. MASZ interlayers with 67 and 80 weight percent zirconia were studied in detail in validation experimentation. The compositions of MASZ interlayers are provided in Table 4. The joining of zirconia ceramics using the MASZ interlayer powders required joining pressures of less than 2 MPa, much lower than those used for the CTS and CAS interlayers. This apparently was due to good wettability and high reactivity of the interlayer with the base zirconia material. The joint strengths achieved with MASZ interlayers also were much improved over CTS and CAS interlayers. For example, the best bend strength obtained for the CTS system was 66 MPa while the average strength of the MASZ-80 system was 158 MPa.

Table 4. MgO-Al_2O_3-SiO_2-TiO_2-Zro_2 (MASZ) interlayer composition.

Powder No.	MgO	Al_2O_3	SiO_3	TiO_2	ZrO_2
MASZ-0	14.9	19.9	56.1	9.1	0
MASZ-33	10.0	13.3	37.6	6.1	33.0
MASZ-50	7.5	10.0	28.0	4.5	50.0
MASZ-67	4.9	6.6	18.5	3.0	67.0
MASZ-80	3.0	4.0	11.2	1.8	80.

The results of a detailed study of the joining of zirconia ceramics produced using MASZ interlayers were reported in two manuscripts which we show reproduced in Appendix B.

2.3 ZIRCONIA/NODULAR CAST IRON JOINTS

Two brazing processes were used in the fabrication of the zirconia/NCI joints. The active-substrate process developed at ORNL was initially selected because of the reported ability to form joints at temperatures sufficiently low to avoid degradation of the NCI[(a)].

(a) Metals and Ceramics Information Center: Structural Alloys Handbook, 1989 ed., Vol. 1.

Repeated attempts to fabricate joints with contact areas on the order of 20 cm^2 using this process failed; these are described in Appendix C. At the suggestion of Dr. M. Santella of ORNL, the active-filler metal process was then employed in the fabrication of the successful joints used for validation studies. The active filler metal had the composition 59.18 Ag, 27.50 Cu, 12.13 In, and 1.18 Ti all in weight percent.

The surfaces of the billets were made flat and uniform by grinding to a 220 grit finish using standard machining practices for the NCI and a resin bonded diamond wheel for the zirconia. The NCI was used in the as-ground state, while (in latter experimentation) the zirconia was polished using a vibratory polisher to a specular finish using successive grades of diamond paste, typically to 9 μm. Prior to assembly, or film deposition, all of the specimens were cleaned using acetone followed by a methanol rinse, typically using an ultrasonic bath. In most cases, filler-metal foils were lightly abraded to remove or break up any native oxide.

Brazing was carried out at OSU in a graphite resistance-heated vacuum hot press. The specimens were placed on a pedestal and brazing was carried out without an applied load. Typical vacuums were in the range of 2×10^{-5} to 1×10^{-4} torr. The heating schedule used with the active filler metal process was: 10-12 C/min to 650 C; 3 to 5 C/min to 735 C; and cooling at about 7 C/min to room temperature. Power was typically cut off when the temperature reached 735 C. It was found empirically that due to the thermal mass of the samples and the radiant properties of the graphite element, this procedure resulted in a maximum temperature very close to 750 C.

All efforts involving the active filler metal process resulted in strong joints. Ultrasonic scanning examination showed that the joints were free of microscopic defects; correspondingly, the unsuccessful joints fabricated using the active substrate process indicated a brain-like structure of the joint composed of large segregated regions of bonds and no bonds. Four large scale joints were brazed and used in the validation studies.

Microstructural analysis was performed on specimens taken from the first active filler metal process braze, using an electron microprobe using a wavelength dispersion spectroscopic (WDS) analyzer. Figure 14 shows a backscattered electron image and WDS element maps of the joint. Ti segregation to the region near the surface of the zirconia is evident (Figure 14b). Interestingly, a two-layer structure involving Ti is observed which is qualitatively very similar to that observed in the microstructure of the 2.0 μm thick Ti-layer active substrate joint. This is reasonable since the relative weight percentages of Ti, Ag and Cu are nearly the same for these systems (see Appendix C). Some differences, however, are apparent. The active substrate process employs Sn, and this element is found in significant proportion in the second Ti enriched region. In the active filler metal process Sn is replaced with In and careful examination of the element maps in Figure 14 reveals that the In is distributed in the Ag-rich phase and the outer Ti enriched region appears to be a Ti-Cu alloy. Also, the Ti-Sn-Cu phase in the active substrate joint is coarse relative to the Ti-Cu phase in the active filler metal joint.

Ti segregation appears to have had other beneficial aspects. Electron microprobe analysis identified a thin Ti enriched phase adjacent to exposed graphite nodules, perhaps involving carbide formation, and several isolated iron bearing particles, presumably milling debris, were encapsulated with a thin layer of Ti enrichment.

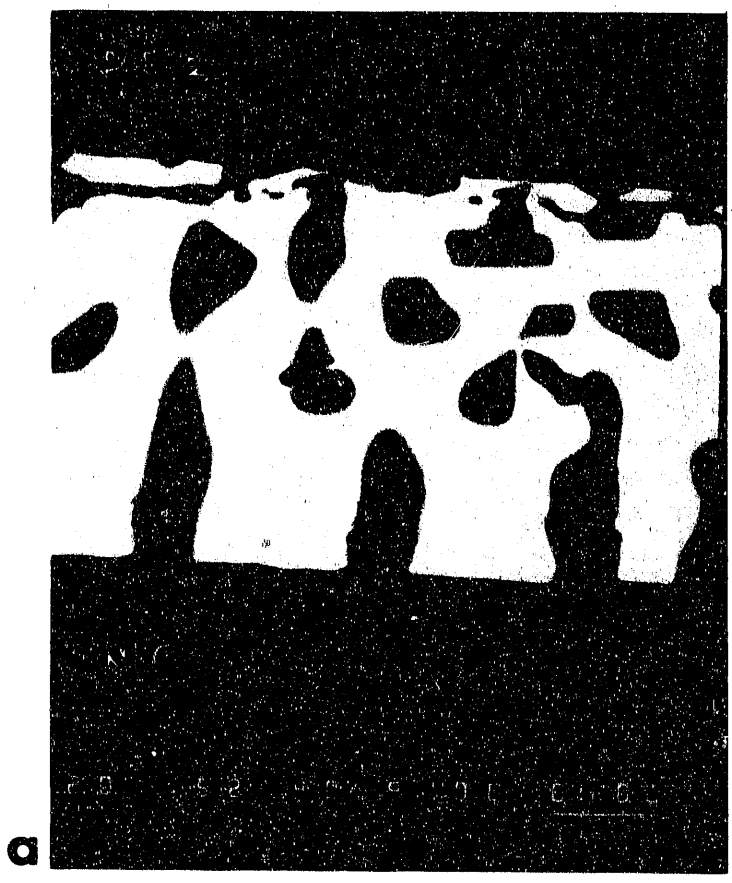

Figure 14a. Backscattered electron image of the interlayer region of an active filler metal joint fabricated using as-ground NCI, polished zirconia, and Incusil-ABA filler metal.

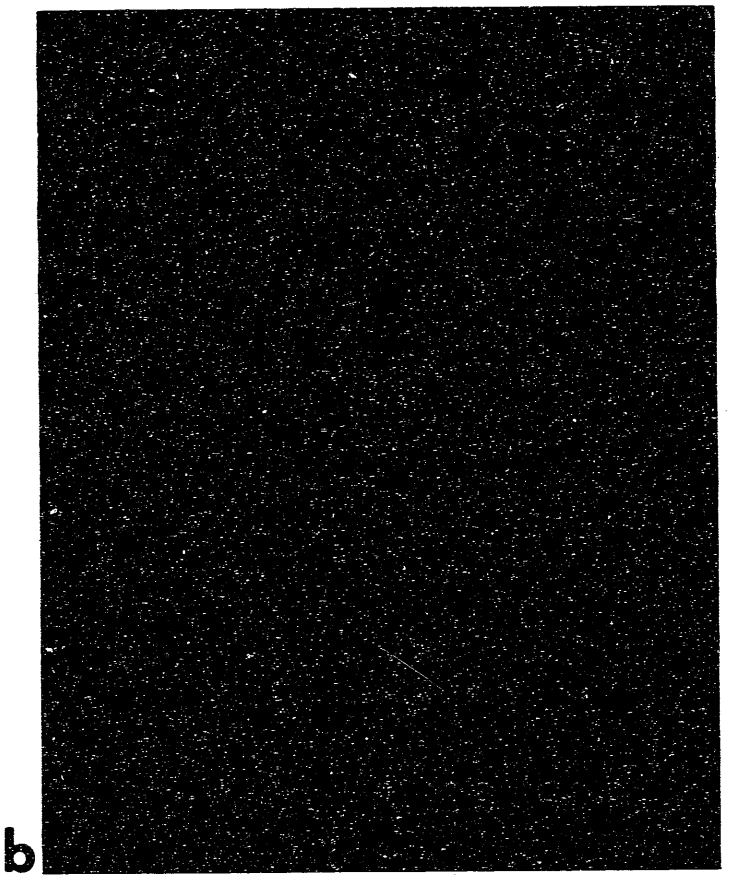

Figure 14b. WDS element map for Ti.

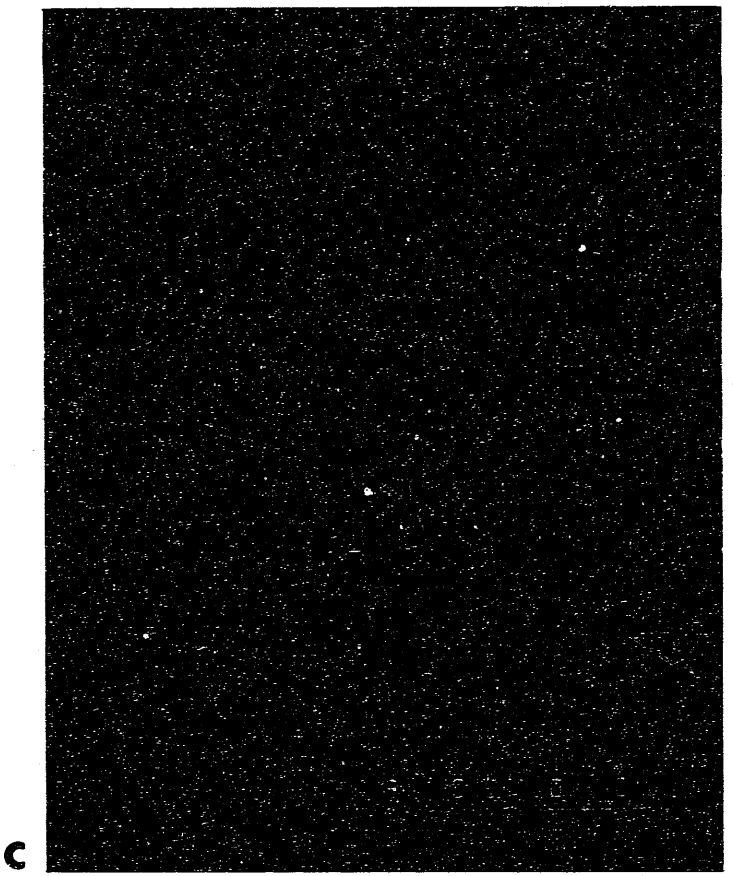

Figure 14c. WDS element map for In.

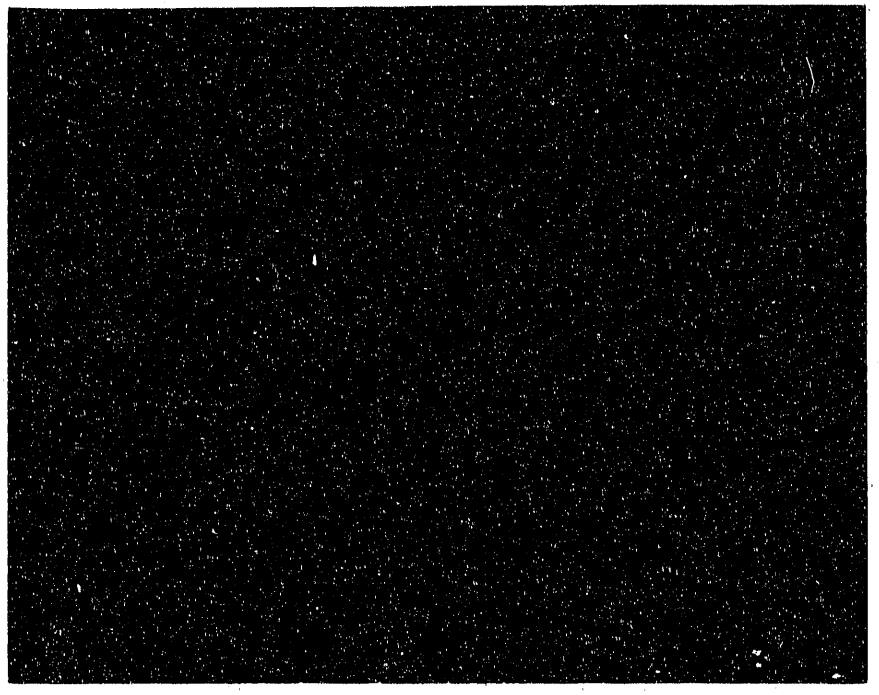

Figure 14e. WDS element map for Ag.

Figure 14d. WDS element map for Cu.

3.0 CHARACTERIZATION OF JOINTS AND CONSTITUENT MONOLITHIC MATERIALS

3.1 OBJECTIVES OF CHARACTERIZATION

Mechanical and thermal characterizations of materials (adherents and interlayers) were performed in support of the joint assessment and design model. The following were the three primary objectives:

1. To obtain constitutive properties of base materials and interlayer materials as input data to the JAD model.

2. To measure the load-bearing capability of small joint specimens (4-point notched/unnotched bend bars) for preliminary validation of the JAD model, and for incorporating appropriate modifications to the model to suit experimental results.

3. To measure the load bearing capability of large joint specimens (cracked disks) as part of the final validation procedure for establishing the JAD model.

The data generated included stress-strain relations and thermal expansion characteristics of base materials (adherents) and interlayer materials for input to the finite element analysis of the joints. Stress-strain data were obtained primarily at room temperature although a few experiments were also performed at elevated temperatures. Based on these results as well as data on the adherents in the published literature, estimates were obtained for the flow stress, ultimate tensile strength, elastic modulus, and Poisson's ratio of the materials as a function of temperature. The higher temperature data were needed primarily for calculating residual stresses, and it is envisaged that for more accurate residual stress estimates it would be necessary to actually perform additional tensile and bend tests at elevated temperatures.

Preliminary validation procedures involved determining the fracture strength and load-displacement behavior of small sized joints, and comparing the results with predictions of the JAD model. Notched bend bars, loaded in 4-point bending, were used for preliminary validation while unnotched 4-point bend bars were used for estimating the efficiency of the joints; efficiency is defined as the ratio of strength of the joint to strength of the monolithic ceramic. Experiments on unnotched specimens also helped in determining the preferred fracture path, namely, whether a crack propagated in the interlayer, the reaction zone of the base material, or through the base material. This served as an input to the JAD model. In this context, it may be noted that although strengths and toughnesses of adherents and interlayer materials can be determined separately, there is currently no straight-forward route for estimating apriori the corresponding properties of the reaction zone, or properties of the interface between the interlayer and adherents. Thus, unless the strength of these regions is greater than the adherent or the interlayer, or there is a convenient way of determining separately the strength and toughness of these regions, it is not possible to predict apriori the location of fracture, which is needed for the JAD model. Fortunately, as will be discussed later, failure of zirconia/zirconia joints occurred primarily through the interlayer, which coincided with the fact that the strength and toughness of the bulk

interlayer (either MASZ-67 or MASZ-80) was always less than the base heat-treated zirconia. On the other hand, in the case of zirconia/NCI joints, failure occurred partly through the reaction zone of the zirconia and partly through the Ti-rich region immediately adjacent to the zirconia. This fracture path could not be predicted based on bulk measurements, nor could the fracture load of notched bend bars be predicted based on data of braze metal or as-received zirconia. Such experiments further confirmed the importance of performing small-scale validation experiments as part of establishing a joint design methodology.

Final validation was performed by testing cracked disk specimens subjected to diametral compression, with the crack (along the joint plane) rotated at various angles to the loading direction. This specimen had a joint area that was 20 times that of the bend bars used in preliminary validation, and served to evaluate the JAD model for a scaled up joint. The disk specimen served two additional purposes. First, because the specimen geometry differed significantly from that of the bend bar, testing of the disk specimen helped in establishing geometry independence of the design methodology. Second, it helped in validating the joint model over a considerable mixed-mode (different combinations of opening and sliding modes) loading domain. This aspect, although not as significant in the fracture of monolithic materials, assumes considerable importance for joints, because of the inherent mixed-mode nature of loading of bimaterial interfaces.

The details of the characterization and analysis task are illustrated by the chart in Figure 15. As shown in the figure, the task has been grouped under the following headings:

1. Materials
2. Specimen designs
3. Key properties characterized
4. Test conditions
5. Microstructure
6. Fractography, particularly for determining the fracture path
7. Preliminary analysis

3.2 EXPERIMENTS

3.2.1 Materials Characterized

The bulk constituent materials characterized for input to the JAD model consisted of the following:

1. As-received partially stabilized zirconia. The data for this material were used for assessing the zirconia/NCI joints, since the thermal cycle associated with the brazing cycle (maximum temperature of 750 C) did not involve any phase

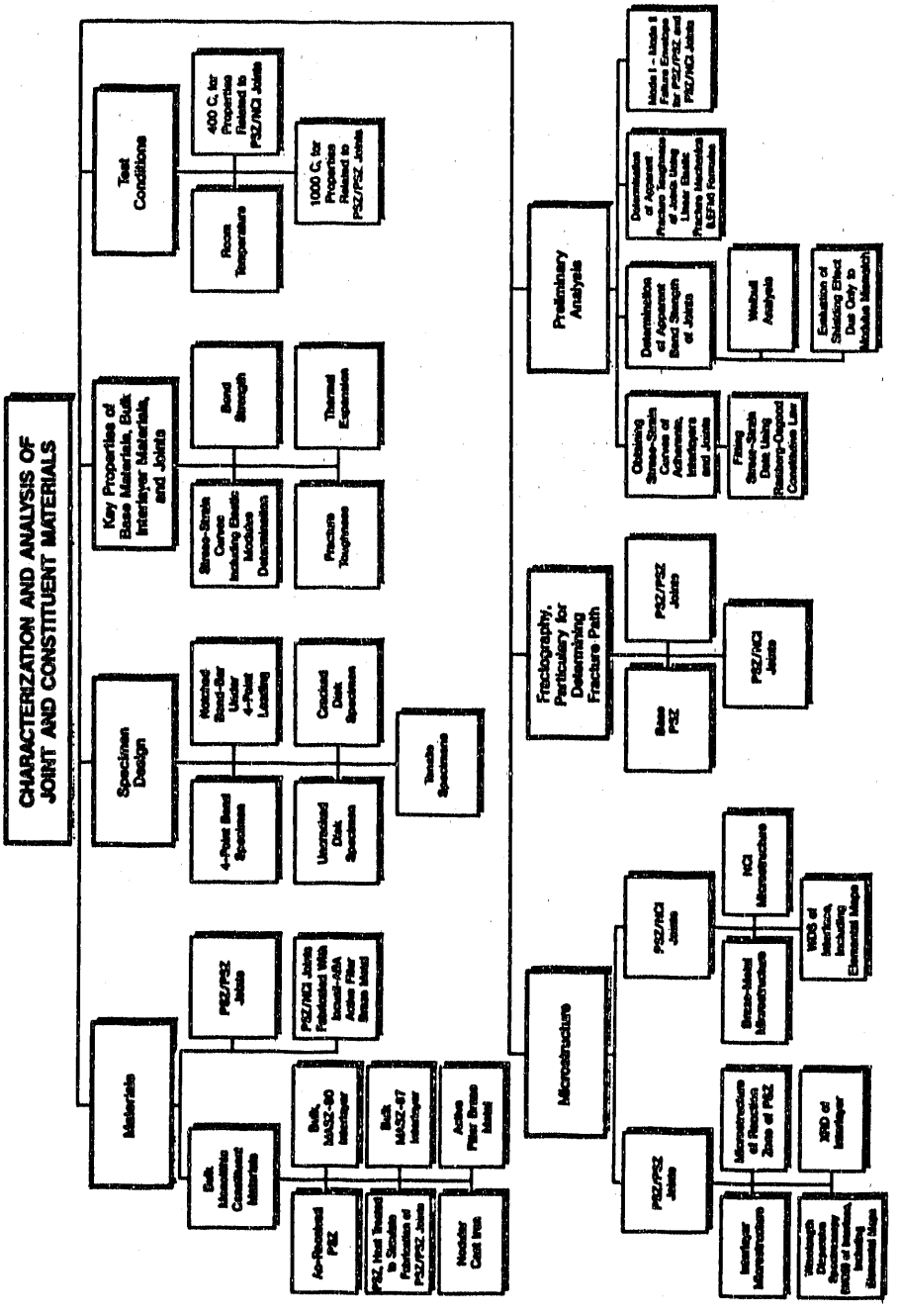

Figure 15. Diagram of characterizations and analyses of materials.

transformation, and was found not to significantly affect the bulk properties[a] of the zirconia.

2. Heat-treated zirconia, involving a soak at 1350 C for 2 hours in air. The heat treatment was used to simulate the thermal cycle involved in the zirconia/zirconia joints. Although the thermal cycle (it involved phase transformations of the zirconia) was found to have negligible effect on the elastic properties of the zirconia it had significant effect on the flow strength, bend strength, and fracture toughness of the material as well as on the overall thermal expansion coefficient. For this reason it was believed appropriate that properties of the heat treated zirconia be used in the JAD model when analyzing zirconia/zirconia joints.

3. Nodular cast iron which was used for the zirconia/NCI joints. No heat treatment was applied to the NCI since the brazing temperature was too low to have any effect on this material.

4. Bulk MASZ-67 and bulk MASZ-80 interlayers. It may be recalled from the previous section that these magnesia-alumina-silica-zirconia interlayers were used for fabricating zirconia/zirconia joints.

5. Incusil-ABA active filler braze metal, used in fabricating zirconia/NCI joints. The active filler metal incorporated Ti, which was found to impart excellent wettability to the zirconia.

In addition to the bulk constituent materials, zirconia/zirconia and zirconia/NCI joints were characterized for validating the JAD model, and also for incorporating modifications as necessary in the model to account for observed phenomena. For example, preliminary validation experiments helped to identify the fracture path, and also to estimate an appropriate strain energy release rate value for zirconia/NCI joints.

The zirconia/zirconia joints that were characterized included joints fabricated using the following interlayer materials at the bonding temperature indicated:

1. Zirconia/zirconia joints fabricated using MASZ-50 interlayer and fabricated at 1350 C.

2. Zirconia/zirconia joints fabricated using MASZ-67 interlayer and fabricated at 1350 C.

(a) However, as will be indicated later, the brazing process involved formation of a reaction zone in the zirconia immediately adjacent to the braze metal. Because it was not possible to obtain bulk specimens from the reaction zone, in the JAD model it was assumed that the reaction zone had the same elastic and thermal properties as the bulk material. The toughness value was obtained by testing a notched bend bar with the crack located in the reaction zone but at a slight distance from the braze-metal/reaction zone interface. This toughness was found to be lower than that of the bulk zirconia.

3. Zirconia/zirconia joints fabricated using MASZ-67 interlayer and fabricated at 1400 C.

4. Zirconia/zirconia joints fabricated using MASZ-80 interlayer and fabricated at 1350 C.

5. Zirconia/zirconia joints fabricated using MASZ-80 interlayer and fabricated at 1400 C.

The zirconia/NCI joint that was characterized was fabricated using Incusil-ABA active filler braze metal at a joining temperature of approximately 750 C.

In addition to the above joint types, many zirconia/zirconia joints such as those fabricated using calcia-titania-silica (CTS) interlayer, or zirconia/NCI joints fabricated using the active substrate process, were characterized but they were not included for further analysis because of poor joint strengths. Those data are not included in this report, although some of the data are available as part of the published papers[3,4] reproduced in Appendix B.

3.2.2 Specimen Design

As illustrated in Figure 15, a number of different specimen geometries were used for characterizing the mechanical behavior of bulk monolithic materials and joints. The specimen types were:

1. Unnotched rectangular bars (Figure 16a), loaded in 4-point pure bending, for determining the bend strength and stress-strain behavior of monolithic ceramic specimens and specimens containing joints.

2. Notched bend specimen (Figure 16b), loaded in 4-point bending, for determining the fracture toughness of monolithic ceramic specimens and specimens containing joints. The machined notch was alligned along the mid-plane of the bond. This specimen geometry was used as part of the preliminary validation procedure.

3. Tensile specimen, used for evaluating the stress-strain behavior of nodular cast iron and braze metal.

4. Uncracked disk specimen, loaded in diametral compression, with the bond plane rotated at an angle of 30 degrees to the load axis. This specimen design was used for evaluating the shear strength of zirconia/zirconia joints.

5. Cracked disk specimen, loaded in diametral compression, with the machined notch/crack at various angles to the loading axis. This specimen geometry was used as part of the final validation procedure, and it had a bond area that was approximately 20 times that of the bend bar used in preliminary validation of the joint assessment model.

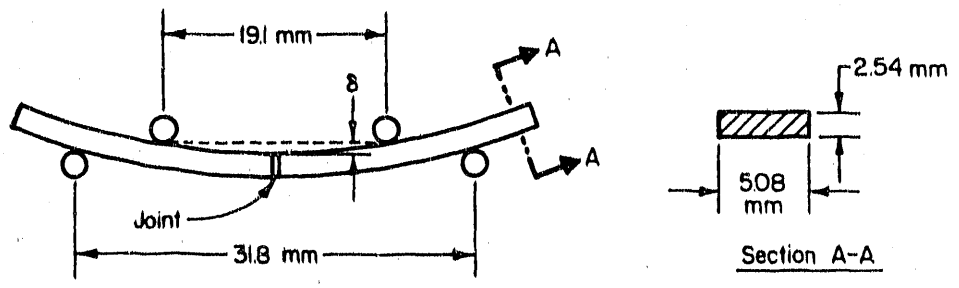

Figure 16a. Bend test geometry for evaluation of the bend strength of joints and of constituent materials. Displacement, δ, was measured between the upper loading pins and the center of the compression face of the bend bar, using a high-resolution LVDT.

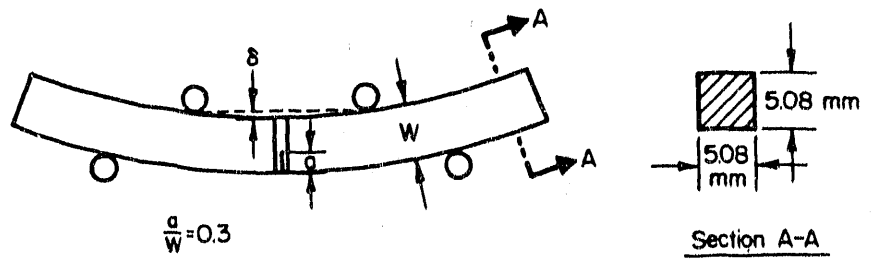

Figure 16b. Notched bend test geometry for evaluating the fracture toughness of constituent materials, and for preliminary validation testing of joints.

The 4-point bend specimen (Figure 16), was of nominal width 5.08 mm, thickness 2.54 mm, and length 38.1 mm. The specimen was finish ground using a 110-grit diamond wheel and was loaded under 4-point bending using a self-allignig fixture that allowed for free rotation in two directions. Figure 17 is a photograph of the experimental setup. The lower loading pins were 31.75 mm apart, while the upper loading pins were 19.05 mm apart. A high accuracy displacement measuring fixture was used to determine the center displacement of the bend bar with respect to the upper loading pins; a displacement of 0.1 μm was easily resolved by the LVDT assembly and calibration procedure. For some of the specimens that were used for generating stress-strain curves, the strain on the tension face of the bend bar was monitored using a strain gage bonded to that face. In this way, it was possible to determine the true stress-strain curve from the measured stress-strain and load-displacement plots.

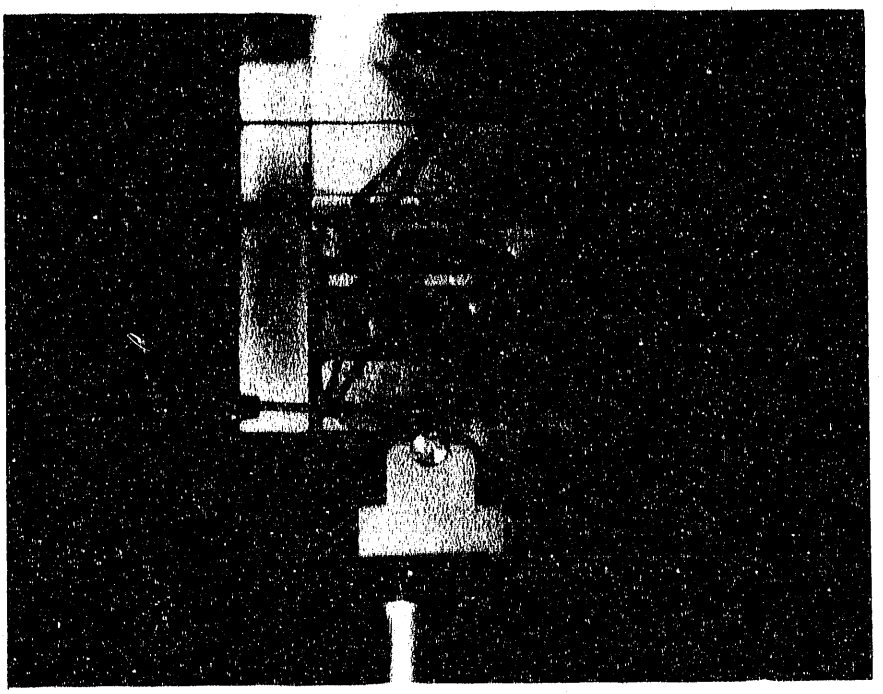

Figure 17. Experimental setup for bend testing of constituent materials and joints. The LVDT core-rod is located at the center, above the specimen.

The notched bend bar specimen is illustrated in Figure 16b. A fine slitting saw was used to make the notch, which was approximately 0.3 mm wide. The ratio (a/W) of crack length (a) to specimen depth (W) was approximately 0.3. Fatigue precracking was not attempted since earlier experiments, involving toughness evaluation of the as-received zirconia using straight notched and chevron notched bend bars as well as chevron-notched disk specimens, indicated that the straight-notched bend specimen provided fracture toughness data that were in excellent agreement with those generated using other specimen geometries.

The machined notch was centered along the mid-plane of the bond in the case of zirconia/zirconia bonds. However, for zirconia/NCI joints it was not always possible to maintain the notch along the mid-plane of the bond. Rather, because of softness of the braze metal, there was always a tendency for the fine slitting saw to deviate into the reaction zone of zirconia, although the extent of deviation was extremely small (typically less than 50 μm). Preliminary experiments indicated that this did not have any significant effect on the fracture toughness value. This was in agreement with the observed fracture path for unnotched bend specimens, which showed that crack propagation occurred partly through the reaction zone of the zirconia and partly through the Ti-interface next to the zirconia. Hence, for consistency purposes, the machined notch was cut in the reaction zone, and within 50 μm of the zirconia/braze interface. Fractographic evidence indicated that this did not prevent the crack from partly weaving through the Ti-rich zone of the braze metal.

The geometries of the uncracked disk and cracked disk specimens are illustrated in Figures 18a and 18b, respectively. The specimens were loaded in compression, with paper cards used to prevent crushing the specimens at the loading points. The uncracked disk specimen was used to determine the shear strength of joints by orienting the crack plane and bond at an angle of 30 degrees to the compression loading axis. For such an angle, the normal stress is zero at the center, and the shear stress (assuming homogeneous material and no residual stresses) is given by:

$$t = \sqrt{3}\ P/\pi RB$$

In the case of the cracked disk specimen, a fine slitting saw was also used to cut the notch, approximately 0.3 mm wide. Figure 19 is a photograph showing the fine slit in a disk specimen. The slit is located well within the dark band which is the reaction zone of the zirconia, although in this particular case the slit is not exactly centered on the bond-line; in some of the specimens, the tip of the notch did coincide with the center-line of the bond, but these specimens did not indicate any significant difference in fracture load compared with slits machined in the manner shown in Figure 19.

The ratio of half-notch length (a) at the specimen faces to the radius (R) of the disk was nominally 0.5, while the ratio of half-length of the chevron notch at mid-thickness to the radius was typically 0.41. For the chevron-notched disk specimen, a stable crack is generally formed that propagates through the entire chevron notch prior to fast fracture. However, it was observed that when the crack angle was large (typically greater than 15 degrees), there was a sharp deviation of the crack from the bond and notch plane even before the crack had propagated through the entire chevron notch. Therefore, in all cases, the crack length at fast fracture was estimated from the fracture surface; i.e., a/R that was used for calculation purposes was obtained from observations of the fracture surface. The crack opening displacements (COD) were measured in a direction perpendicular to the crack plane using a COD gage with strain-gage arms. The knife edges were located on the specimen at equal distances of 3.81 mm on either side of the slit. Figure 20 is a photograph of the experimental setup. The extensometer was calibrated over a maximum span of 25 μm, and this provided a resolution of better than 0.1 μm for monitoring crack opening displacements.

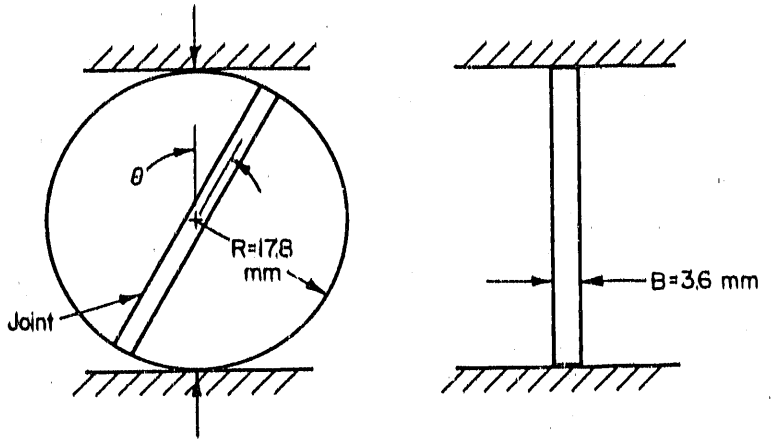

Figure 18a. Un-notched disk specimen for measuring the shear strength of joints.

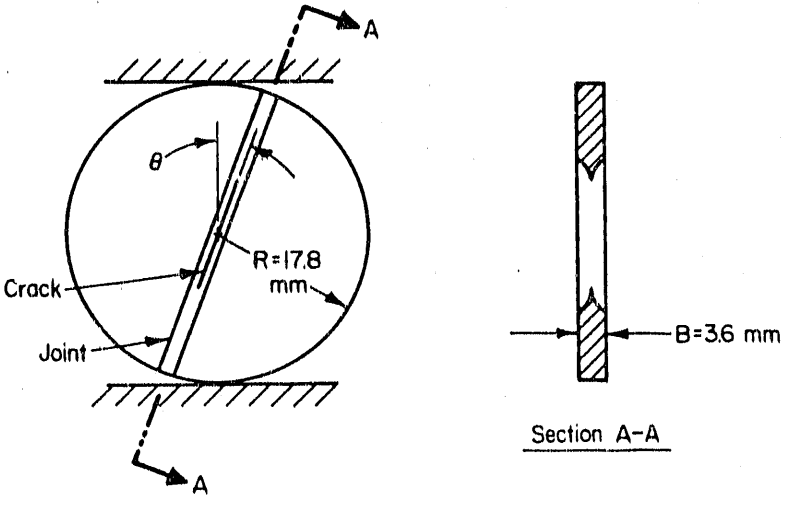

Figure 18b. Chevron-notched cracked disk specimen used in final validation testing of joints.

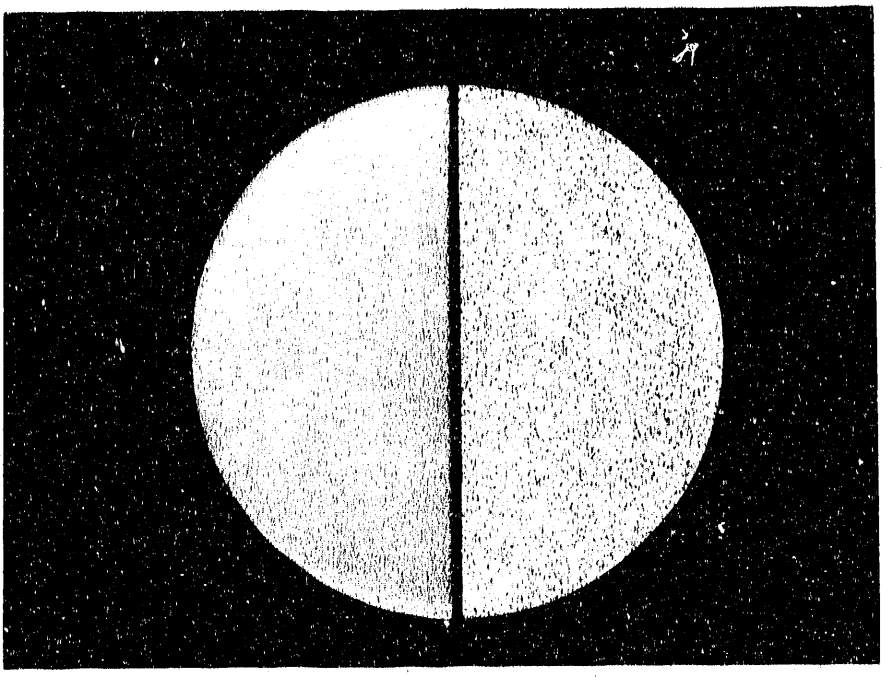

Figure 19. Photograph of zirconia/NCI cracked disk specimen. The zirconia is on the left and NCI is on the right.

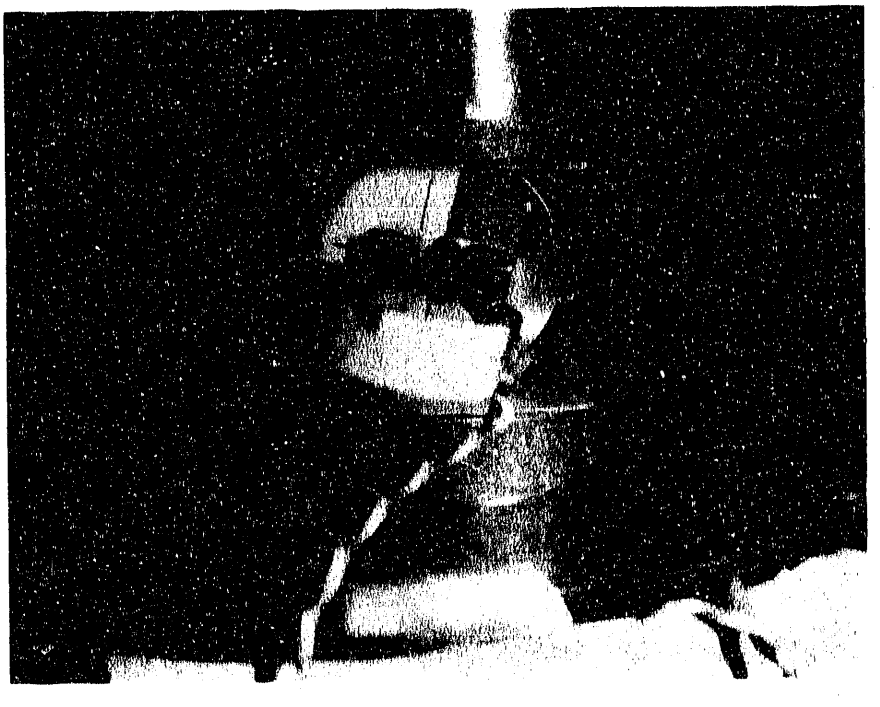

Figure 20. Experimental setup used in final validation testing of joints using cracked disk specimen.

Tensile sheet specimens were used for evaluating the stress-strain behavior of the braze metal and nodular cast iron. These were pulled to failure in a servo-hydraulic testing machine. Strain was monitored with an extensometer employing strain gages.

3.2.3 Key Properties Characterized

Thermal Expansion. The only physical property that was measured was the thermal expansion behavior of adherents and interlayers, and they served as input to the FEM code for evaluating residual stresses. The thermal expansion of as-received zirconia, NCI, and braze metal were determined from room temperature (RT) to 730 C, which was near the processing temperature for zirconia/NCI joints. The thermal expansion trace was essentially linear, and did not indicate any phase transformation over the temperature domain. The thermal expansion behavior of heat-treated zirconia was determined over the temperature range RT to 1350 C. The thermal expansion behavior of the ceramic interlayers, namely MASZ-67 and MASZ-80 interlayers, were only evaluated over the temperature range RT to 1200 C, since they were molten at temperatures above 1300 C. These interlayers indicated phase transformations over the temperature domain of interest.

Stress-Strain Behavior. The stress-strain behavior of adherents, bulk interlayer materials, and specimens containing joints were determined primarily at room temperature. The stress-strain curves of the constituent materials were then fit to a non-linear Ramberg-Osgood constitutive relation. Significant non-linear deformation was observed for the base zirconia material, NCI and braze metal. Even the ceramic interlayer materials indicated some non-linear deformation; for example, the proportional limit for MASZ-67 interlayer was only 63 percent of the material's bend strength. That is why inealstic fracture mechanics principles were used in the JAD model to account for the non-linear deformation response of the constituent materials.

Elevated temperature tests consisted of experiments performed at 200 C and 400 C for braze material and NCI, and at temperatures of 400 C, 750 C, and 1000 C for the zirconia material. These results, along with those available in the published literature were used for estimating the stress-strain response at intermediate temperatures.

Bend Strength. Bend strengths of base materials and joints were obtained from 4-point bend tests. Standard mechanics of material formulas for a homogeneous continuum were used to evaluate the bend strength of the joint from the geometry of the specimen and the failure load. Although this provided only the apparent bend strength of the joint, the error was estimated to be less than 8 percent, because the elastic modulus mismatch of the materials was small for both the zirconia/zirconia and zirconia/NCI systems, and also because of small differences in the thermal expansion coefficient of the constituent materials. Nevertheless, it is useful to keep this point in mind when assessing the joint strengths in the tables listed later in this section.

A sufficient number of specimens were tested to obtain the Weibull modulus of the base materials and joints. This parameter is useful for assessing the variability of data, with a high number indicating lower scatter in strength compared with a material with a low Weibull modulus value. The efficiency of the joint was obtained from the ratio of the average bend strength of the joint with respect to the strength of the base zirconia. In all cases, efficiency was less than unity with the worst efficiency observed for zirconia/zirconia joints fabricated using the MASZ-50 interlayer.

For zirconia/zirconia joints, it was observed that the preferred fracture path was the interlayer material. Because of this crack path, it was possible to relate the bend strength of zirconia/zirconia joints with the bend strength of the corresponding interlayer. For zirconia/NCI joints, failure occurred partly through the reaction zone of the zirconia and partly through the Ti-rich layer of the braze metal. Accordingly, it was not possible to relate the bend strength of the constituent bulk materials to that of the joint.

Fracture Toughness. The fracture toughnesses of base materials and joints were evaluated using notched bend bar and cracked disk specimens. Appropriate formulas were used to determine fracture toughness from the applied load and specimen geometry. The fracture toughness data of constituent materials (adherents and interlayers) were used as input to the JAD model. Mixed-mode fracture toughness data were used for evaluating the dependence of strain energy release rate on mode mixity, expressed in terms of the phase angle Ψ, $\tan^{-1}(Q_{II}/Q_I)$[(a)].

3.2.4 Test Conditions

Mechanical properties of adherents and interlayer materials, and the load-bearing capability of joints were determined at RT, 400 C and at 1000 C. However, most of the experiemnts were performed at room temperature. The 400 C tests were used for evaluating the performance of zirconia/NCI joints at that temperature. 1000 C tests were used for evaluating the performance of zirconia/zirconia joints at that temperature. All tests were performed in air.

3.2.5 Microstructure

The microstructures of zirconia/zirconia and zirconia/NCI joints were observed using optical and scanning electron microscopy (SEM) techniques. Chemical analysis, using wavelength dispersive spectroscopy (WDS) on a JEOL 733 microprobe, was performed to determine the chemical species responsible for good wetting between interlayer and adherents, and also for evaluating any undesirable reaction product that may have formed as a result of the joining process. In addition, limited X-ray diffraction was performed on the MASZ interlayer materials to understand the source of R-curve behavior that was observed for notched zirconia/zirconia joint specimens. Details of some of the microstructures obtained for zirconia/zirconia joints, fabricated either with a CTS interlayer or an MASZ interlayer are provided in the papers[3, 4, 5] in Appendix B.

Most of the microstructural examinations were performed at tne begining of this program, while developing appropriate bonding interlayers and joining conditions for reliable joints. During the validation stage, microstructural examination was limited to determining the thickness of the bonds. For zirconia/zirconia joints, interlayer thickness ranged between 100 and 150 μm, while for zirconia/NCI joints, the interlayer thickness ranged between 50 and 80 μm.

(a) For bimaterial systems, the counterpart to the monolithic fracture toughness parameter K is denoted by Q.

3.2.6 Fractography

The fracture surfaces of representative specimens were examined optically and by using SEM. Limited energy dispersive X-ray analysis (EDS) was conducted to obtain estimates of the chemistry in different regions of the fractue surface. Such observations and measurements helped in identifying the preferred fracture path, namely, whether a crack propagated through the adherents, or through the bonding interlayer, or through the interface between the interlayer and adherent. Additional confirmation of the fracture path was obtained by sectioning fractured samples perpendicular to the fracture surface, metallographically polishing those sections, and observing such polished sections using optical and scanning electron microscopy techniques.

3.2.7 Preliminary Analysis of Data

A preliminary analysis of the data included the following:

1. Reducing the load-versus-displacement data and load-versus-strain-gage data to determine the stress-strain behavior of the constituent materials. All the constituent materials showed some degree of non-linearity at room temperature, and the stress-strain results were mathematically expressed using the elastic-plastic Ramberg-Osgood relation:

$$\epsilon/\epsilon_o = (\sigma/\sigma_o) + D\,(\sigma/\sigma_o)^n$$

where σ denotes stress, ϵ denotes strain, σ_o yield stress, ϵ_o yield strain, σ_o/ϵ_o represents the elastic modulus, E, and D is a constant.

2. Determination of apparent bend strengths of the joints from the load at failure, using the standard bend-bar formula for a homogeneous material. Although such a procedure neglects residual stresses from thermal expansion mismatch and shielding stresses from modulus mismatch, it provides a basis for comparing the strength of the joint with respect to the strength of the base ceramic. This is similar to the JAD model procedure used for notched specimens, where the distance measured, in the direction of the joint assessment vector, from the origin to the failure envelope is compared with the reference load, which is the load required to break a monolithic ceramic specimen.

   The bend strengths of constituent materials and joints were expressed in the form of Weibull plots. The data were arranged in increasing values of strength, and the probability of failure was expressed through the relation:

$$P = i/(N+1)$$

where i is the rank (i = 1 corresponding to the lowest strength), and N is the number of samples tested. The Weibull modulus was obtained by plotting ln (1/(1-P)) versus strength on a log-log plot, and determining the slope of the best fit straight line.

Additional analytical efforts associated with bend strengths of unnotched specimens involved predicting the stength of joints from the strength of the bulk interlayer material. This procedure was feasible for zirconia/zirconia joints because it was observed that failure occurred preferentially in the interlayer. The predictive effort had to incorporate shielding effects, since the modulus of the interlayer was consistently less than the surrounding zirconia, thereby reducing the local stress at the failure location with respect to the far-field applied stress. These shielding effects are discussed in the attached paper[6]. In the case of zirconia/NCI joints, such a predictive procedure could not be used because failure occurred partly through the reaction zone of the zirconia and partly through the Ti-rich zone of the braze metal. In this case, a predictive methodology for bend strength would require measurement of the bend strength of the reaction zone. Although this could be performed in principle, by depositing a Ti-film on the surface of an as-received zirconia bend bar, and then subjecting the sample to a 750 C heat treatment, such experiments were not performed in this program.

3. Evaluating the fracture toughness of notched bend bars using the following LEFM formula for a homogeneous material:

$$K_I = 6MY(a/W)\sqrt{a} / BW^2$$

where K_I is the mode I stress intensity factor, M is the magnitude of a pure bending moment, a is the crack length, W is the beam depth, B is the beam thickness, and Y is a function of a/W given by:

$$Y(a/W) = 1.99 - 2.47(a/W) + 12.97(a/W)^2 - 23.17(a/W)^3 + 24.80(a/W)^4$$

The fracture toughness of constituent materials and the apparent fracture toughness of joints were calculated using the above formulas. Of course, the apparent fracture toughness of joints is denoted by Q_I. The reason that the above formulas provide only apparent fracture toughness of joints is that the formulas do not take into account the elastic and thermal mismatch of the constituents, although the latter was small for the constituent materials considered in this investigation. Nevertheless the apparent toughness values provide an approximate means for comparing the fracture toughness of joints with those of the constituent materials, and are tabulated in Section 3.3. It may be noted, in this context, that the local Q of zirconia/zirconia joints, fabricated with MASZ 67 interlayer material, at failure locations inside the interlayer were calculated to be approximately 68 percent of the apparent Q value; for joints

fabricated with MASZ-80 interlayer material, the local Q was approximately 90 percent of the apparent Q value.

The apparent mixed-mode stress intensity factors for zirconia/zirconia joints were obtained using Atkinson's solution[7] for a cracked disk specimen of a homogeneous material, with the crack oriented at various angles to the compression load line. For the zirconia/NCI disk specimens, the current FEM results for a bimaterial disk specimen provided by Professor C. F. Shih were used for determining the Mode I-Mode II stress intensity factors; Atkinson's analytical results were within 5 percent of the current FEM values, primarily because the modulus mismatch between zirconia and NCI was quite small. The apparent mixed-mode data were reduced using the current analytical results to compute the local Q_I and Q_{II} values at failure. These local Q values were then plotted in the form of G versus mode mixity, (Ψ), ($\Psi = \tan^{-1}(Q_{II}/Q_I)$). Such plots were helpful in developing and assessing an appropriate function which related strain energy release rate to Ψ. Currently there does not exist a universal functional form of G versus Ψ, and the form suggested by Evans and Hutchinson[8] $G(\Psi) = G_o Sec^2\Psi$, had to be modified based on data from monolithic ceramics which suggested that the form $G(\Psi) = G_o Sec^2(\Psi/\Psi_o)$, where Ψ_o is a constant, was more appropriate.

3.3 TEST RESULTS

The presentation of the test results is divided into three sections:

1. Results of mechanical and thermal property measurements that were used for generating baseline data for constituent material properties. These results were used as input data to the FEM code and JAD model.

2. Results of mechanical tests on unnotched and notched bend bars that were used as part of preliminary validation of the JAD model.

3. Results of mechanical tests on cracked disk specimens that were used as part of the final validation of the JAD model.

3.3.1 Properties of Constituent Materials

Thermal Expansion. Figure 21 provides the thermal expansion trace of the base zirconia material over the temperature range 100 C to 1300 C; measurements were made over a gage length of 38.1 mm. The expansion trace provided an average thermal expansion (α_{th}) coefficient of approximately 10.3 x 10^{-6}/C, and this value was used in the analysis of zirconia/zirconia joints. Figure 22 is a thermal expansion trace of the base zirconia over a narrower temperature range, RT to 730 C. The plot shows minimum hysterisis, and here too the average thermal expansion coefficient is 10.3x10^{-6}/C. For NCI an α_{th} of 14.9x10-6/C was obtained. For the Incusil-ABA braze metal, a thermal expansion coefficient of 18.2x10-6/C was obtained from the material supplier.

The thermal expansion trace of bulk MASZ-67 interlayer material, that was used in zirconia/zirconia joining, is shown in Figure 23. In this case significant non-linear expansion may be observed; in particular, the volumetric expansion and contraction that are observed

in the temperature range 550 C to 900 C can be ascribed to a monoclinic to tetragonal (and vice versa) phase transformation mechanism most likely involving the retained zirconia particles in the interlayer material. A similar thermal expansion trace was obtained for the MASZ-80 interlayer. Because of the complexity of the thermal expansion trace, the actual data were used in the computation of residual stresses in the FEM model.

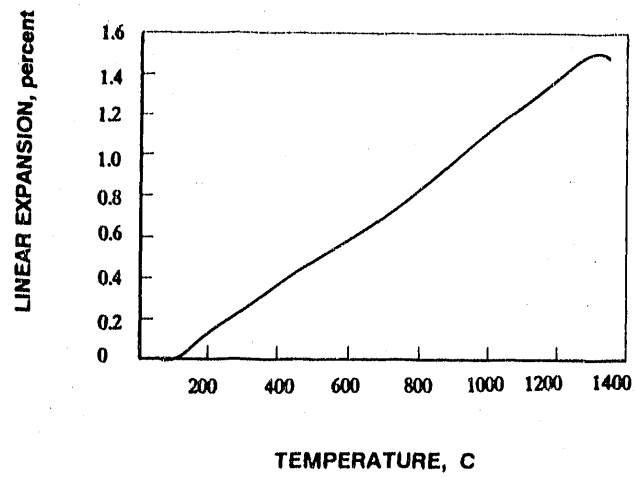

Figure 21. Thermal expansion trace of base zirconia from room temperature to 1300 C.

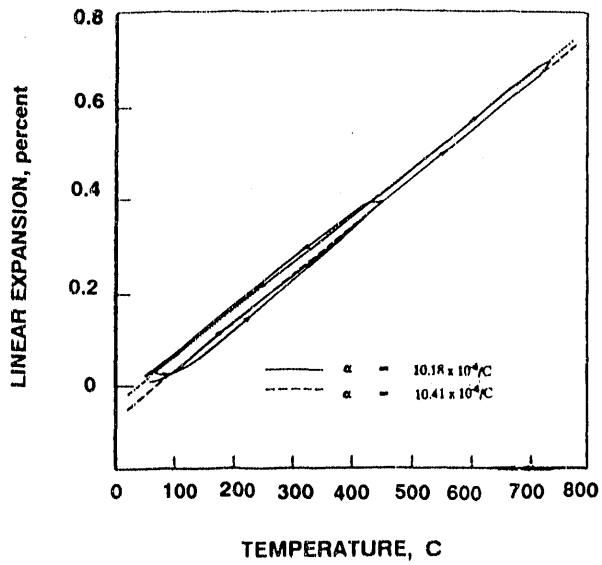

Figure 22. Thermal expansion of base zirconia material from room temperature to 730 C.

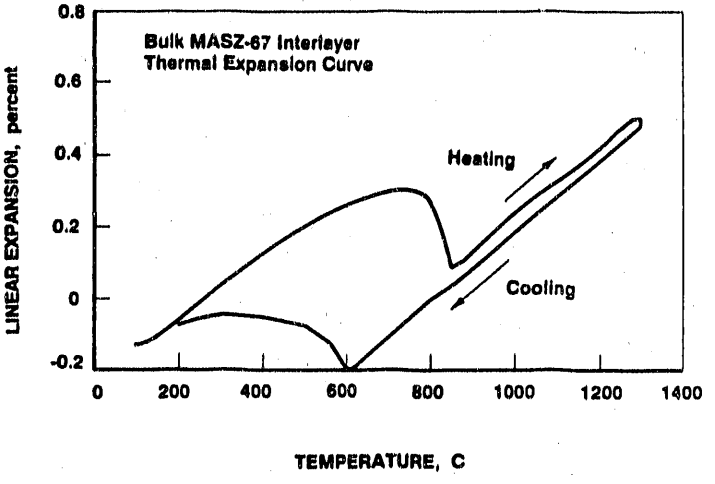

Figure 23. Thermal expansion of MASZ-67 material from room temperature to 1300 C.

For completeness, the thermal expansion trace of a zirconia/NCI joint is shown in Figure 24. The specimen was a bend bar of length 38.63 mm, and the expansion was measured in a direction perpendicular to the joint plane (braze metal thickness was approximately 70 μm). An average α_{th} of 11.84x10-6/C was obtained. This value may be compared with α_{th} of 10.3, 14.9, and 18.2 ppm/C for the zirconia, NCI, and braze metal, respectively.

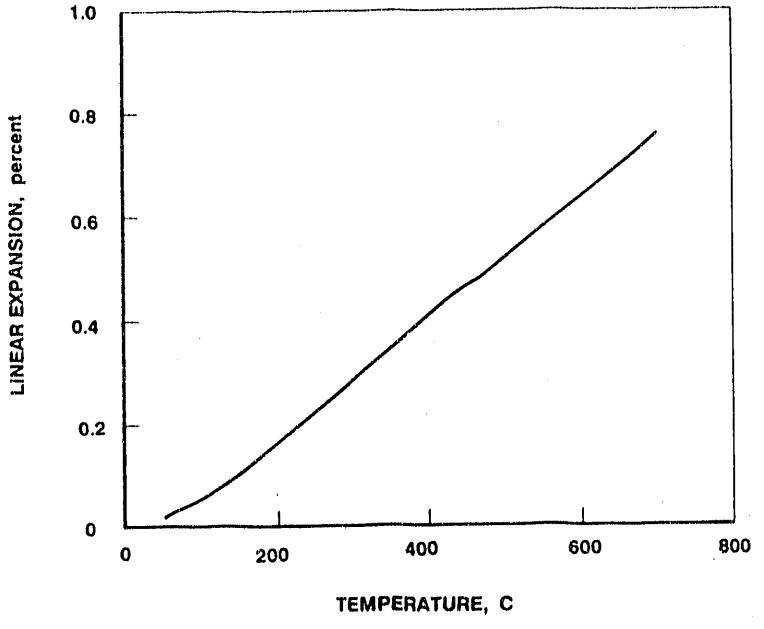

Figure 24. Thermal expansion of zirconia/NCI joint.

Stress-Strain Behavior of Constitutive Materials. Figures 25-30 illustrate the true stress-strain behavior of the following constituent materials at room temperature:

1. As-received zirconia (Figure 25),
2. Heat-treated zirconia, heat treated at 1350 C (Figure 26),
3. Nodular cast iron (Figure 27),
4. Incusil-ABA (Figure 28),
5. Bulk MASZ-67 ceramic interlayer, sintered at 1350 C (Figure 29),
6. Bulk MASZ-80 ceramic interlayer, sintered at 1350 C (Figure 30).

The true stress-strain data were fit using the Ramberg-Osgood relation given earlier in this section. Table 5 provides appropriate parameters used for fitting the stress-strain curves. The Poisson's ratios that are provided in the table were not measured but were obtained from the literature. The table also includes parameters for elevated temperature behavior. Among these latter results, the complete stress-strain behavior was experimentally measured at 400 C for the braze metal and NCI, and at 200 C for the braze metal; wire specimens were used in measuring the stress-strain property of braze metal, since thicker sections were not available. The stress-strain behavior of zirconia at elevated temperature was estimated based on the room temperature results confirmed with data available in the literature; only the elastic modulus and bend strength were measured for zirconia at temperatures of 400 C, 750 C and 1000 C.

The average bend strength of ceramic specimens are also tabulated in Table 5. Bend test results of individual specimens are provided in the master Table 6. Weibull moduli of constituent materials were determined, and they are summarized in a table provided later in this report.

In Tables 6 and 7 the individual specimens are identified by a key which indicates the billet, the specimen type, and location of specimen in the billet prior to machining. The first four characters of the specimen number correspond to the particular joined billet. Thus, a specimen number such as HP22-B13 is a specimen that was machined from joined billet number HP22. The letter identifiers B, F, UD, and CD indicate specimen type; bend bar, notched bend bar (fracture), uncracked disk, and notched disk. The last two digits of the specimen number provide an approximate idea of the specimen location within the billet, with the first digit corresponding to the row number and the second digit corresponding to the column number. This is illustrated in Figure 31, and, except for the as-received zirconia, bulk interlayer materials, and the HP22 block (where row numbering was started with 0 rather than 1), this convention was followed for all the specimens.

Fracture Toughness of Constituent Materials. The fracture toughness of constituent materials and apparent fracture toughness of joints are tabulated in Table 7. Table 8 is based on Table 7, and provides average Q_{Ic} and corresponding G_{Ic} values for the various constituent materials. In this table, the toughness of the reaction zone of zirconia/NCI joints was evaluated from a notched-bend bar test, where the crack propagated entirely through the reaction zone of the zirconia, away from the Ti-rich interface of the braze metal.

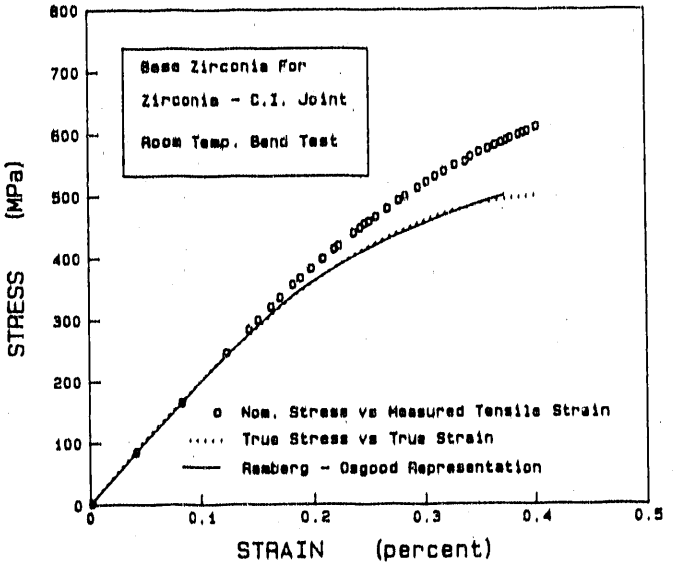

Figure 25. Room temperature stress-strain behavior of as-received zirconia.

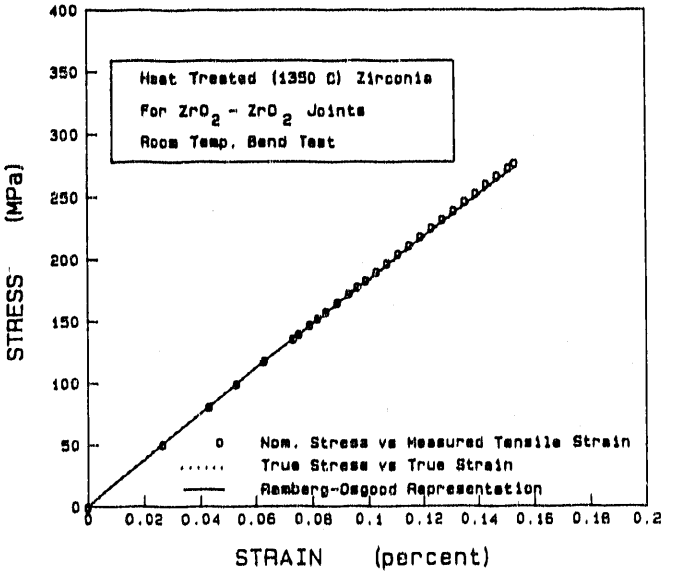

Figure 26. Room temperature stress-strain behavior of heat treated zirconia.

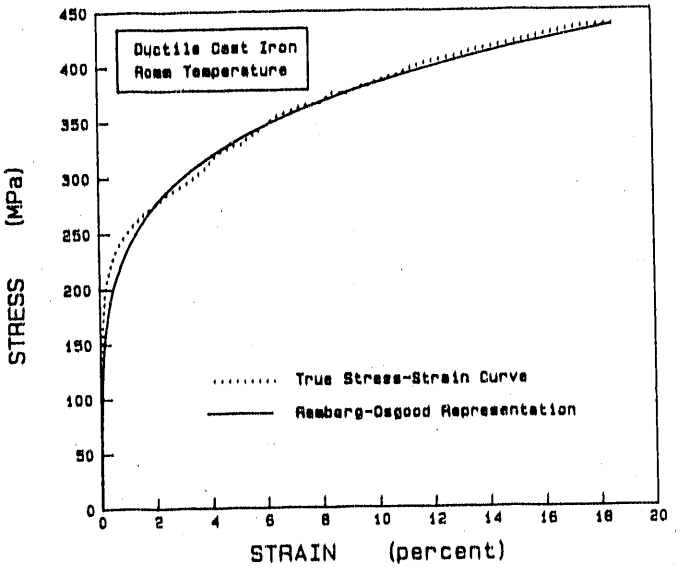

Figure 27. Room temperature stress-strain behavior of nodular cast iron.

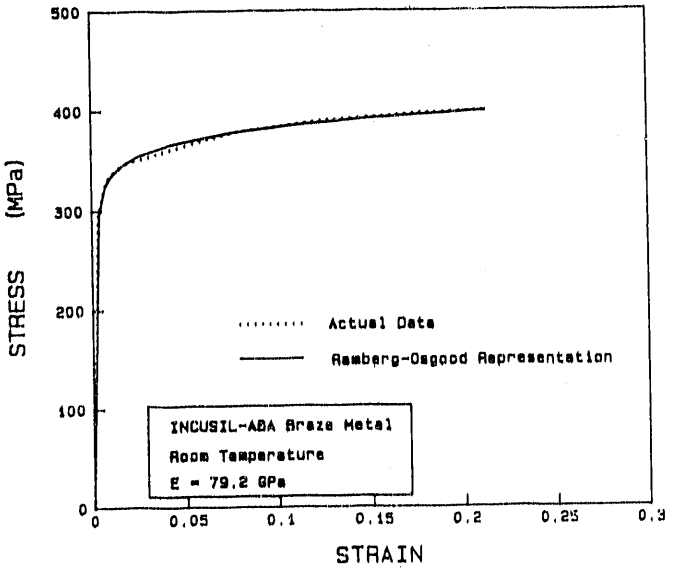

Figure 28. Room temperature stress-strain behavior of Incusil ABA braze metal.

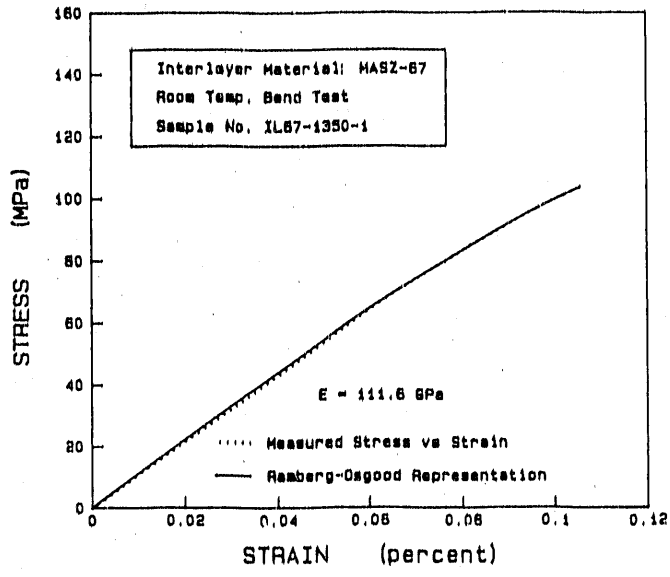

Figure 29. Room temperature stress-strain behavior of MASZ-67 material.

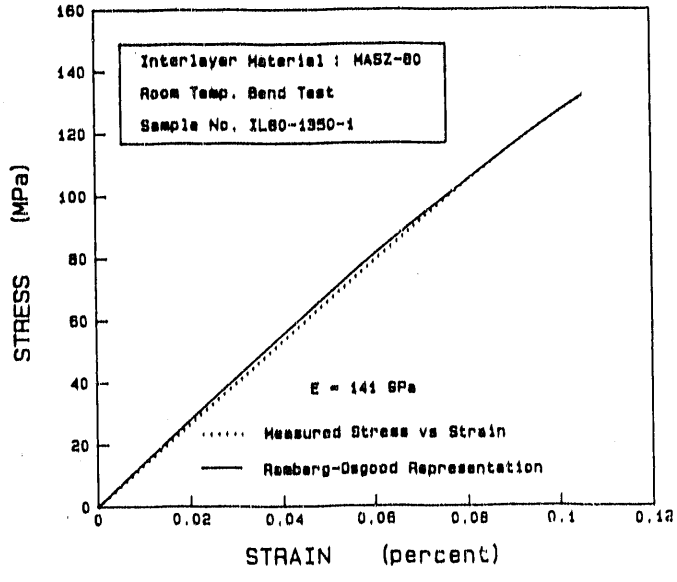

Figure 30. Room temperature stress-strain behavior of MASZ-80 material.

Table 5. Stress-strain parameters for constituent materials used in zirconia/zirconia and zirconia/NCI joining.

Constituent Material	σo MPa	εo	E, GPa	Fracture Strength, MPa	n	α	Poisson's Ratio
Room Temperature Data							
As-Received Zirconia	301.8	0.000150	202.0	589	5.66	0.05	0.22
Heat-Treated Zirconia	140.6	0.000698	201.4	291	1.62	0.08	0.22
Bulk MASZ-67 Interlayer	74.0	0.000662	111.7	122	3.93	0.05	0.22
Bulk MASZ-80 Interlayer	101.7	0.000720	141.2	158	3.15	0.07	0.22
Nodular Cast Iron (NCI)	221.9	0.000136	163.4	437	4.99	4.61	0.28
Incusil-ABA Braze	295.6	0.000373	079.3	402	19.58	0.15	0.36
Elevated Temperature Data							
NCI, 260 C (a)	199.2	0.001245	160.0	431	7.50	2.50	0.28
NCI, 400 C	159.2	0.001010	157.5	276	10.00	0.06	0.28
NCI, 538 C (a)	122.3	0.000870	140.0	240	10.00	0.06	0.28
NCI, 607 C (a)	90.6	0.000686	132.0	200	10.00	0.06	0.28
NCI, 716 C (a)	45.3	0.000390	116.0	170	10.00	0.06	0.28
Incusil-ABA, 200 C	362.7	0.007510	048.2	414	74.20	0.00	0.28
Incusil-ABA, 400 C	101.4	0.007340	013.8	53.4	109.00	0.08	0.28
As-received ZrO2, 200 C (b)	269.5	0.001368	197.0	483	5.70	0.05	0.22
As-received ZrO2, 400 C (b)	232.3	0.001213	191.4 (c)	453 (c)	5.70	0.05	0.22
As-received ZrO2, 600 C (b)	195.1	0.001063	183.5	381	5.70	0.05	0.22
As-received ZrO2, 800 C (b)	158.0	0.000910	173.2	308	5.70	0.05	0.22
As-received ZrO2, 1000 C (b)	120.8	0.000753	160.5 (d)	236 (d)	5.70	0.05	0.22
As-received ZrO2, 1200 C (b)	83.6	0.000575	145.4	163	5.70	0.05	0.22
As-received ZrO2, 1400 C (b)	46.5	0.000363	127.9	91	5.70	0.05	0.22

(a) E and sigma-o estimated from Structural Alloys Handbook [H88], modified to account for current room temperature results. Rest of terms are best estimates.

[H88]: Structural Alloys Handbook, Vol. 1, Ed. J.B. Hallowell, MCIC, Battelle (1988)

(b) Estimates, based on current data and data in the literature, particularly, "Engineering Property Data on Selected Ceramics, Vol. 3, Single Oxides", MCIC Report No. MCIC-HB-07, Battelle Memorial Institute, Columbus, Ohio (1982)

(c) Measured modulus and bend strength were 176.5 GPa and 249 MPa respectively.

(d) Measured modulus and bend strength were 142 GPa and 225 MPa, respectively.

Table 6. Bend test results of constituent materials and joints.

Specimen Number	Temperature C	Width, B mm	Height, W mm	Load, Pf N	Strength* MPa
As-Received Zirconia					
BZ-B0	25	5.01	2.55	983.5	575
BZ-B2	25	4.98	2.56	1041.3	610
BZ-B7	25	5.01	2.56	1001.3	581
BZ-B8	25	5.03	2.55	1014.6	593
BZ-B4	400	5.00	2.56	235.9	249
BZ-B5	750	5.09	2.54	224.7	237
BZ-B3	1000	4.98	2.56	206.9	220
BZ-B9	1000	5.08	2.56	220.3	230
Zirconia/Zirconia Joint With MASZ-67 Interlayer, 1350 C Processed					
HP22-B01	25	5.87	3.08	360.5	123
HP22-B02	25	5.87	3.02	387.2	138
HP22-B03	25	5.86	3.04	369.4	130
HP22-B04	25	5.87	2.95	369.4	138
HP22-B05	25	5.85	2.90	275.9	107
HP22-B11	25	5.32	2.72	222.5	108
HP22-B12	25	5.51	2.72	231.4	108
HP22-B13	25	5.59	2.73	233.6	107
HP22-B14	25	5.36	2.73	264.6	126
HP22-B15	25	5.52	2.73	267.0	123
HP22-B16	25	5.30	2.73	244.8	118
HP22-B21	25	5.15	2.56	214.0	121
HP22-B23	25	5.15	2.56	242.5	137
HP22-B25	25	5.15	2.56	182.5	103
HP22-B26	25	5.15	2.56	264.8	149
HP22-B27	25	5.15	2.56	174.4	98
HP22-B28	25	5.13	2.55	244.8	140
HP23-B22	25	5.08	2.51	213.6	127
HP23-B11	1000	5.06	2.55	58.7	62
HP24-B11	1000	5.09	2.55	51.6	54
HP24-B13	1000	5.08	2.55	55.2	58
HP24-B14	1000	5.07	2.52	62.3	67
HP24-B15	1000	5.09	2.56	60.1	63
Zirconia/Zirconia Joint With MASZ-80 Interlayer, 1350 C Processed					
HP25-B11	25	5.09	2.53	240.3	140
HP25-B12	25	5.08	2.56	284.8	163
HP25-B13	25	5.08	2.55	204.7	118
HP25-B17	25	5.09	2.56	262.6	151
HP25-B21	25	5.08	2.52	329.3	194
HP25-B22	25	5.08	2.55	293.7	170
HP25-B28	25	5.08	2.55	195.8	113
HP25-B23	25	5.08	2.52	329.3	194
HP25-B29	25	5.07	2.55	316.0	182
HP25-B24	1000	5.08	2.55	71.6	75
HP25-B15	1000	5.06	2.55	75.7	80
HP25-B18	1000	5.07	2.55	82.3	87

* For joints, these strengths are apparent bend strengths.

Table 6. (continued)

Specimen Number	Temperature C	Width, B mm	Height, W mm	Load, Pf N	Strength* MPa
Zirconia/Zirconia Joint With MASZ-50 Interlayer, 1350 C processed					
HP27-B13	25	5.07	2.54	93.5	54
HP27-B14	25	5.07	2.54	89.0	52
HP27-B17	25	5.07	2.54	89.0	52
HP27-B21	25	5.09	2.55	77.9	45
HP27-B22	25	5.09	2.54	102.4	59
Base Zirconia, Heat-Treated at 1350 C to Simulate Fabrication of Zirconia/Zirconia Joints					
HP26-B11	25	5.08	2.56	449.5	258
HP26-B12	25	5.07	2.56	491.7	282
HP26-B14	25	5.07	2.55	494.0	286
HP26-B17	25	5.07	2.57	520.7	296
HP26-B19	25	5.07	2.56	498.4	285
HP26-B21	25	5.08	2.57	542.9	309
HP26-B22	25	5.10	2.57	560.7	318
HP26-B23	25	5.09	2.57	525.1	298
HP26-B24	1000	5.09	2.57	212.7	220
HP26-B26	1000	5.07	2.55	195.8	206
Zirconia/Zirconia Joint With MASZ-80 Interlayer, 1400 C Processed					
HP29-B11	25	5.06	2.53	173.6	102
HP29-B11	25	5.06	2.53	182.5	107
HP29-B13	25	5.06	2.53	186.9	109
HP29-B14	25	5.06	2.53	160.2	94
HP29-B21	25	5.09	2.53	204.7	119
HP29-B22	25	5.09	2.53	191.4	112
HP29-B23	25	5.09	2.54	184.7	107
HP29-B24	25	5.09	2.53	173.6	101
HP29-B25	25	5.09	2.53	178.0	104
Zirconia/Zirconia Joint With MASZ-67 Interlayer, 1400 C Processed					
HP30-B11	25	5.09	2.52	104.6	62
HP30-B12	25	5.09	2.53	93.5	55
HP30-B14	25	5.09	2.53	93.5	55
HP30-B15	25	5.09	2.53	111.3	65
HP30-B23	25	5.09	2.54	102.4	59
HP30-B24	25	5.10	2.53	135.7	79
HP30-B25	25	5.10	2.53	102.4	60
Bulk MASZ-50 Interlayer Material, 1350 C Processed					
IL50-1350-1	25	5.08	2.52	104.1	62
IL50-1350-2	25	5.06	2.53	97.9	58
Bulk MASZ-67 Interlayer Material, 1350 C Processed					
IL67-1350-1	25	5.06	2.54	173.6	101
IL67-1350-2	25	5.07	2.55	164.7	95

* For joints, these strengths are apparent bend strengths.

Table 6. (continued)

Specimen Number	Temperature C	Width, B mm	Height, W mm	Load, Pf N	Strength* MPa
IL67-1350-3	25	5.07	2.55	158.0	92
IL67-1350-4	25	5.03	2.55	160.2	93
IL67-1350-5	25	5.01	2.54	160.2	94
IL67-1350-6	25	5.06	2.54	142.4	83
IL67-1350-7	1000	5.07	2.55	65.4	69
IL67-1350-8	1000	5.07	2.54	65.9	70
Bulk MASZ-67 Interlayer Material, 1400 C Processed					
IL67-1400-1	25	5.09	2.55	124.6	72
IL67-1400-2	25	5.09	2.55	142.4	82
IL67-1400-3	25	5.07	2.55	138.0	80
IL67-1400-4	25	5.08	2.55	126.8	73
IL67-1400-5	25	5.09	2.52	135.7	80
IL67-1400-6	25	5.09	2.55	142.4	82
Bulk MASZ-80 Interlayer Material, 1350 C Processed					
IL80-1350-1	25	5.09	2.51	218.1	130
IL80-1350-2	25	5.07	2.52	224.7	133
IL80-1350-3	25	5.07	2.52	235.9	139
IL80-1350-4	25	5.08	2.55	211.4	122
IL80-1350-5	25	5.07	2.53	234.5	138
IL80-1350-6	25	5.07	2.54	249.2	145
IL80-1350-8	1000	5.07	2.54	65.0	69
Bulk MASZ-80 Interlayer Material, 1400 C Processed					
IL80-1400-1	25	5.05	2.54	191.4	112
IL80-1400-2	25	5.06	2.53	213.6	125
IL80-1400-3	1000	5.04	2.54	65.0	69
Zirconia/Nodular Cast Iron Joint					
LMC3-B21	25	5.08	2.57	471.7	267
LMC3-B22	25	5.09	2.34	309.3	212
LMC3-B23	25	5.08	2.54	427.2	248
LMC3-B24	25	5.09	2.53	316.0	185
LMC3-B27	25	5.09	2.52	356.0	210
LMC3-B31	25	5.06	2.56	289.3	166
LMC3-B32	25	5.07	2.56	373.8	215
LMC3-B33	25	5.07	2.56	471.7	272
LMC3-B34	25	5.06	2.56	445.0	256
LMC4-B11	25	5.09	2.34	311.5	214
LMC4-B12	25	5.76	3.28	1068.0	328
LMC4-B21	25	5.07	2.57	371.6	211
LMC4-B22	25	5.07	2.57	342.7	195
LMC4-B24	25	5.07	2.57	391.6	223
LMC4-B28	25	5.07	2.57	467.3	267
LMC4-B31	25	5.09	2.51	331.5	196
LMC4-B32	25	5.10	2.51	498.4	295
LMC4-B33	25	5.09	2.52	252.8	149
LMC4-B36	25	5.10	2.51	369.4	218
LMC5-B13	25	5.08	2.50	218.1	130

* For joints, these strengths are apparent bend strengths.

Table 6. (continued)

Specimen Number	Temperature C	Width, B mm	Height, W mm	Load, Pf N	Strength* MPa
LMC5-B14	25	5.08	2.50	436.1	261
LMC5-B25	25	5.08	2.51	319.5	191
LMC3-B35	400 C	5.07	2.56	104.1	109
LMC5-B12	400 C	5.09	2.55	97.0	102
LMC5-B16	400 C	5.07	2.55	100.1	105

* For joints, these strengths are apparent bend strengths.

Table 7. Fracture toughness test results of constituent materials and joints.

Specimen Number	Temper-ature, C	Width, B mm	Height, W mm	Crack Length, a mm	Fracture Load, Pf, N	Y(a/W)	Q1c*, MPa√m
Zirconia/Zirconia Joint With MASZ-67 Interlayer, 1350 C Processed							
HP22-F15	RT	2.56	5.14	1.53	140.2	1.99	3.07
HP23-F18	RT	5.08	5.10	1.54	209.2	2.00	2.36
HP23-F27	RT	5.09	5.09	1.54	213.6	2.00	2.42
HP24-F15	RT	5.08	5.07	1.63	173.6	2.03	2.07
HP24-F14	1000	5.08	5.09	1.57	80.5	2.01	1.69
HP24-F23	1000	5.10	5.07	1.56	69.9	2.01	1.46
Zirconia/Zirconia Joint With MASZ-80 Interlayer, 1350 C Processed							
HP25-F16	RT	5.09	5.09	1.63	264.8	2.03	3.14
HP25-F26	RT	5.08	5.07	1.63	268.3	2.03	3.19
HP25-F14	1000	5.09	5.07	1.61	82.3	2.02	1.77
Zirconia/Zirconia Joint With MASZ-67 Interlayer, 1400 C Processed							
HP30-F16	RT	5.09	5.08	1.63	107.7	2.03	1.28
HP30-F27	RT	5.09	5.08	1.63	160.2	2.03	1.90
Zirconia/Zirconia Joint With MASZ-80 Interlayer, 1400 C Processed							
HP29-F26	RT	5.09	5.09	1.60	195.8	2.02	2.28
HP29-F27	RT	5.06	5.10	1.63	200.3	2.03	2.37
Base Zirconia, Heat Treated at 1350 C to Simulate Fabrication of Zirconia-Zirconia Joints							
HP26-F16	RT	5.10	5.08	1.71	458.8	2.06	5.67
HP26-F21	RT	5.05	5.08	1.63	458.4	2.03	5.47
Bulk MASZ-50 Material, 1350 C Processed							
IL50-1350-F1	RT	5.07	5.05	1.71	122.4	2.07	1.54

* Q1c=K1c for monolithic materials, and Q1c corresponds to apparent Mode I fracture toughness for joints.

Table 7. (continued)

Specimen Number	Temper-ature, C	Width, B mm	Height, W mm	Crack Length, a mm	Fracture Load, Pf, N	Y(a/W)	Q1c*, MPa√m
Bulk MASZ-67 Interlayer, 1350 C Processed							
IL67-1350-F1	RT	5.09	5.07	1.70	169.1	2.06	2.10
IL67-1350-F3	RT	5.11	5.05	1.70	160.2	2.06	1.99
IL67-1350-F2	1000	5.10	5.07	1.60	68.1	2.02	1.46
Bulk MASZ-80 Interlayer, 1350 C Processed							
IL80-1350-F1	RT	5.12	5.08	1.71	235.9	2.06	2.89
IL80-1350-F3	RT	5.12	5.09	1.65	231.4	2.04	2.75
IL80-1350-F2	1000	5.09	5.09	1.63	73.9	2.03	1.59
Bulk MASZ-67 Interlayer, 1400 C Processed							
IL67-1400-F1	RT	5.12	5.11	1.63	146.9	2.02	1.71
IL67-1400-F2	RT	5.09	5.08	1.63	149.1	2.03	1.77
Bulk MASZ-80 Interlayer, 1400 C Processed							
IL80-1400-F1	RT	5.09	5.09	1.63	445.0	2.03	5.27
Zirconia/ Nodular Cast Iron Joint							
LMC2-F25	RT	5.00	5.09	1.17	529.6	1.89	5.03
LMC3-F25	RT	5.07	5.11	1.63	445.0	2.03	5.23
LMC3-F36	RT	5.12	5.11	1.63	429.4	2.02	5.00
LMC4-F25	RT	5.11	5.07	1.63	600.8	2.03	7.12
LMC4-F26	RT	5.07	5.08	1.60	547.4	2.02	6.42
LMC4-F34	RT	5.09	5.09	1.63	534.0	2.03	6.31
LMC5-F18	RT	5.09	5.09	1.63	422.8	2.03	5.00
LMC5-F26	RT	5.08	5.09	1.60	596.3	2.02	6.97

* Q1c=K1c for monolithic materials, and Q1c corresponds to apparent Mode I fracture toughness for joints.

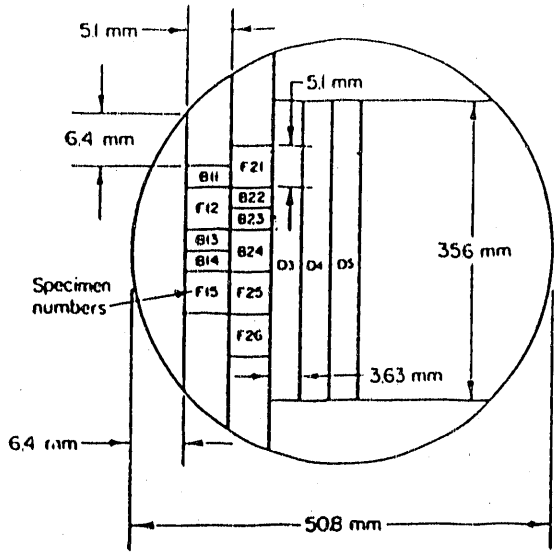

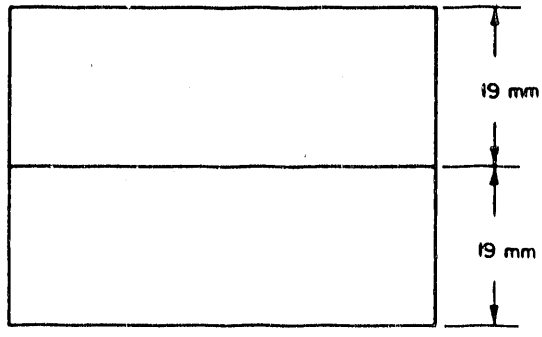

B: Uncracked bend bar, 2.54 x 5.08 x 38.1 mm
F: Notched bend bar, 5.08 x 5.08 x 38.1 mm
D: Cracked or uncracked disk specimen, 35.6 mm dia. x 3.63 mm thick

Figure 31. Source of specimens machined from the joined 2-inch billets.

Table 8. Fracture toughness test results of constituent materials.

Constituent Material	E, GPa	Poisson's Ratio	Klc, MPa√m	Glc, N/m	Avg. Approx. Th. Exp. Coeff., x10-6/C
Room Temperature					
As-received zirconia	202.0	0.22	9.2	394.4	10.3
Heat-treated zirconia	201.4	0.22	5.6	146.6	13.1
Nodular cast iron	163.4	0.28	85.0	40750.1	14.9
Incusil ABA	79.3	0.36	30.0	9878.4	18.2
Bulk MASZ-50, 1350 C processed	109.0	0.22	1.5	20.4	9.5
Bulk MASZ-67, 1350 C processed	111.7	0.22	2.1	35.8	9.5
Bulk MASZ-80, 1350 C processed	141.2	0.22	2.8	53.6	9.5
Bulk MASZ-67, 1400 C processed*	111.7	0.22	1.7	25.8	10.0
Bulk MASZ-80, 1400 C processed*	141.2	0.22	5.3	187.2	10.0
Reaction zone of zirconia (in zirconia/NCI joints)**	202.0	0.22	7.1	237.5	10.3
1000 C					
Bulk MASZ-67, 1350 C processed***	71.7	0.22	1.5	28.3	9.5
Bulk MASZ-80, 1400 C processed*	90.6	0.22	1.6	26.6	9.5

* E and Poisson's ratio are only estimates, based on present data. Klc actually measured.

** Data obtained by testing a notched bend bar containing a zirconia/NCI joint, where the crack propagated only in the reaction zone of the zirconia.

*** Poisson's ratio was estimated.

3.3.2 Preliminary Validation Results

Bend Test Results. Table 6 provides bend test results of constituent materials as well as zirconia/zirconia and zirconia/NCI joints. No significant correlation was found between the specimen strength and its location within the joined billet, suggesting uniformity of bonding, and small residual stress effects (after machining) at least at a distance of 6.5 mm from the billet periphery.

Table 6 includes data generated at room temperature as well as those generated at elevated temperatures; namely, 400 C for zirconia/NCI joints and 1000 C for zirconia/zirconia joints. Test results obtained with different processing temperatures, namely 1350 C and 1400 C for zirconia/zirconia joints, are also included in the table.

Figure 32 is a Weibull plot which provides a comparison of the room temperature bend strengths of zirconia/zirconia joints fabricated using MASZ-67 interlayer with those of the constituent materials. Although the average strength of the joint is less than that of the heat-treated zirconia, it is higher than the strength of the bulk MASZ-67 interlayer. Nevertheless, failure of zirconia/zirconia joints occurred primarily in the ceramic interlayer. As shown in reference[6], this behavior can be rationalized in terms of shielding of the joint interlayer by the surrounding higher modulus zirconia adherent.

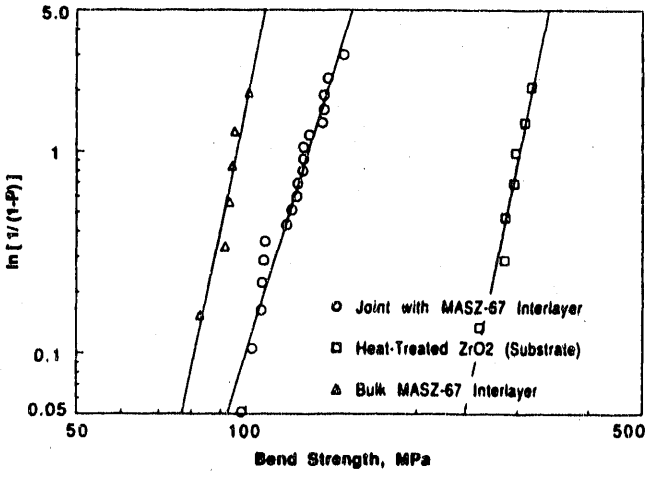

Figure 32. Weibull plot showing comparison of strength of zirconia/zirconia joints and bulk constituent materials.

Figure 33 is a Weibull plot comparing bend strengths of various zirconia/zirconia joints with their corresponding interlayer materials. The actual data points are not included in the plot for the purpose of clarity. This plot indicates that for both the MASZ-67 and MASZ-80 interlayer systems, joints perform better than their corresponding interlayer materials.

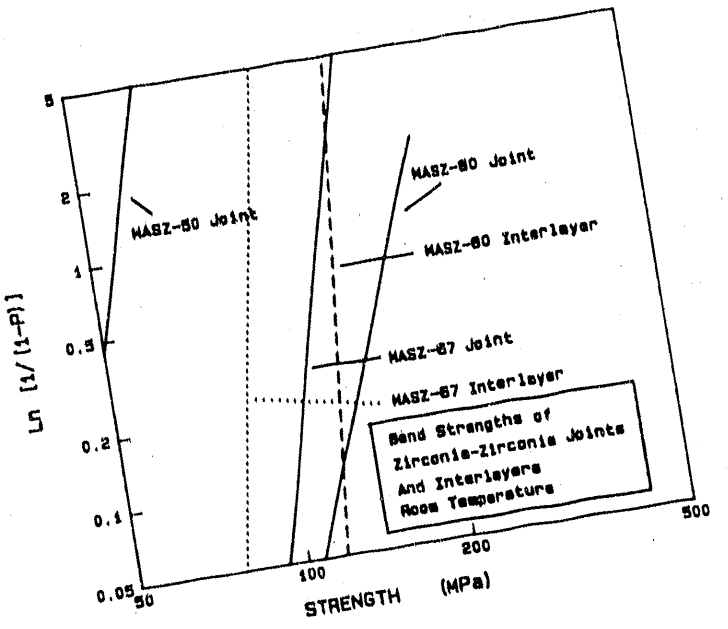

Figure 33. Weibull plot showing comparison of zirconia/zirconia joints and constituent materials as a function of percent zirconia powder in interlayer.

Figure 34 is a Weibull plot of the bend strength of zirconia/NCI joints. The average strength of the joint was 223 MPa compared with an average strength of 589 MPa for the as-received zirconia. A major reason for the strength degradation was the formation of the reaction zone in the zirconia due to oxygen depletion of the Ti-rich interface. As has been noted above, the crack path was partly through the reaction zone and partly through the Ti-rich interface with approximate percentage areas of each ranging between 40 and 60 percent. Fracture toughness measurements, to be discussed later, indicated that the fracture location had lower toughness (6 to 7 MPa√m) than the base zirconia (approximately 9.2 MPa√m). However, this difference cannot account for the large decrease in strength for the joined bend bar. Rather, it is believed that the joining process introduced defects primarily at the braze/zirconia interface, and these larger defects acted to reduce the strength of the joint. This argument is qualitatively in agreement with the observation that the Weibull modulus of the joint was 5.4, while the base zirconia typically has a Weibull modulus of 9.5; in fact, our limited data on the as-received zirconia provide an approximate Weibull modulus of 8.6, while the heat-treated zirconia had a Weibull modulus of 13.4, indicating a rather tight flaw population, i.e., small scatter in flaw size.

Bend strengths of constituent materials and joints are summarized in Table 9. The efficiency of the joints was calculated by dividing the strength of the joint by the strength of the adherent, and they are also tabulated in Table 9.

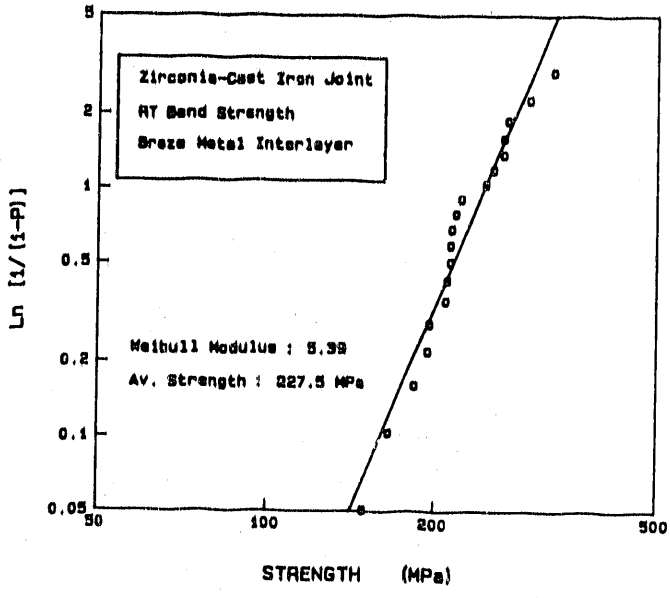

Figure 34. Weibull plot for zirconia/NCI joints.

Table 9. Average bend strength of zirconia/zirconia and zirconia/NCI joints.

	Bulk Material		Joints		
Material	Average Strength, MPa	Weibull Modulus	Average Strength, MPa	Weibull Modulus	Efficiency*, percent
Heat-Treated ZrO_2 Substrate	293	13.4	-	-	-
MASZ - 80	134	20.8	158	6.0	54
MASZ - 67	93	13.6	122	9.0	42
MASZ - 50	59	-	52	-	18
Zirconia/NCI	-	-	223	5.4	38**

* Joint Efficiency = Strength of Joint / Strength of Substrate

** Efficiency of zirconia/NCI joint based on strength of 589 MPa for as-received zirconia.

The load versus displacement data for a joint fabricated with MASZ-67 interlayer, and those of the constituent materials are illustrated in Figure 35. As expected, the load versus displacement plot for the joint agrees very well with that of the heat-treated zirconia, since the thickness of the interlayer was negligible compared with the adherent. Figure 36 is a similar plot for a zirconia/NCI joint. This plot indicates significant non-linearity before fracture and the observed non-linearity is consistent with the fact that the specimen failed at a stress of 261 MPa, while the flow stress of zirconia was only 221.9 MPa. FEM calculations were not performed to check whether there was agreement between the observed load-displacement behavior and calculated elastic-plastic results.

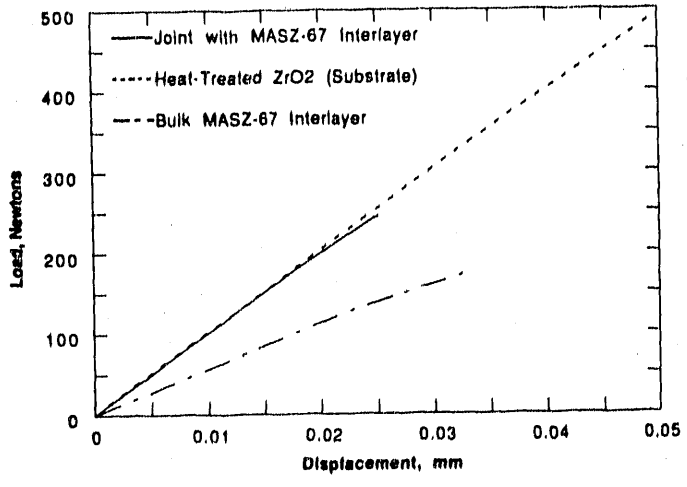

Figure 35. Load versus displacement plots for bend bars fabricated with MASZ-67 interlayer and its constituent materials.

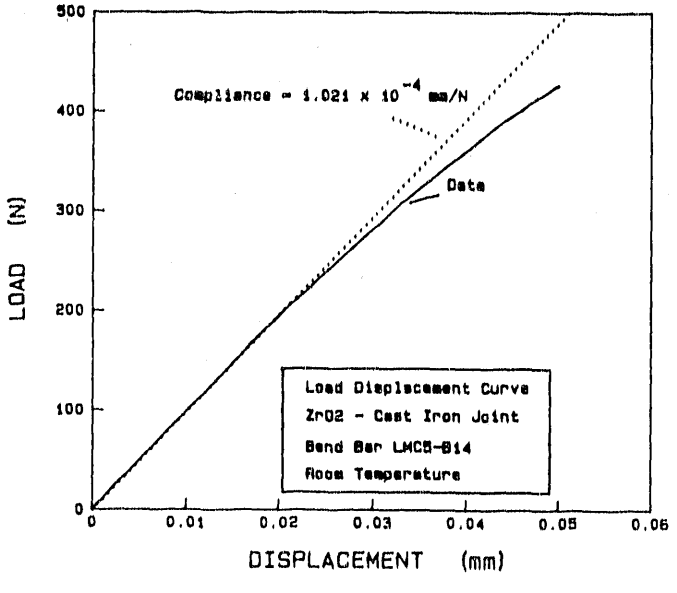

Figure 36. Load versus displacement plot for a zirconia/NCI joint.

Notched Bend Bars and Disk Specimens. The apparent fracture toughnesses corresponding to notched bend bars with joints have already been presented in Table 7. Table 10 provides comparisons of average fracture toughness results of zirconia/zirconia joints, and it has been arranged to show a comparison of the joint apparent toughness with that of the corresponding interlayer material. Similar to unnotched bend bars, there is a slight increase in the toughnesses of zirconia/zirconia joints (fabricated at 1350 C) compared with those of the corresponding interlayer materials. Although the higher toughness of the joint compared with the bulk interlayer can partly be explained[6] by a shielding effect, it appears that there was degradation of the interlayer material for zirconia/zirconia joints fabricated with MASZ-67 interlayer. For this material system, the apparent toughness of the joint was 2.5 MPa√m, and analytical results indicate that this would correspond to a local stress intensity of 1.7 MPa√m at the interlayer location of the joint. On the other hand, the bulk interlayer had a toughness of 2.1 MPa√m; this would imply a 19 percent loss in toughness of the interlayer material due to the joining process. In the case of the MASZ-80 system, however, there did not appear to be any degradation in toughness of the interlayer material due to the joining process.

Table 10 indicates that the zirconia/zirconia joints fabricated at 1400 C behaved differently, in that joint toughnesses were lower than bulk interlayer toughnesses. This was particularly true for the MASZ-80 interlayer fabricated at 1400 C, which has potential as a good structural material by itself. The lower joint toughnesses compared with interlayers can probably be explained by the observation that the crack propagated primarily through the reaction zone of the zirconia; i.e., the reaction zone was the weakest link rather than the ceramic interlayer material. Use of the JAD model indicated that the measured failure load for those specimens would require a G_{Ic} that lay between 10 and 30 N/m for the reaction zone, and these G_{Ic} values would correspond to a toughness between 1.46 MPa√m and 2.1 MPa√m for the reaction zone of the base zirconia (significantly lower than 5.6 MPa√m for the heat-treated zirconia). Thus, 1400 C was obviously too high a temperature for zirconia/zirconia joining in that it caused intensive degradation of the base zirconia material.

For zirconia/NCI joints, the toughness of the joint was much less compared with either the base zirconia, NCI, or the braze metal. The explanation lies in the fact that the crack propagated partly through the reaction zone of the zirconia and partly through the Ti-rich interface at the braze-metal/zirconia interface. These locations were not available as bulk materials for independent toughness measurements. Because of this problem, it was recognized that the toughness of the braze metal or the base zirconia was not suitable for incorporation in the JAD model, because they did not represent local fracture energies. Therefore, an indirect approach was followed in that the load to failure of zirconia/NCI notched bend bars was used for back-calculating the local G_c at the failure location. It was understood that because of this approach, the JAD model could not utilize the results of notched bend bar tests, performed on zirconia/NCI joints, for validation purposes. However, the approach allowed for validation using the cracked disk specimen for zirconia/NCI joints. The fracture energy of the zirconia/NCI joint was determined as 184.5 N/m using the above procedure. This value was in good agreement with a test where failure in a notched zirconia/NCI specimen occurred entirely through the reaction zone of the zirconia; this particular specimen indicated a G_{Ic} of 237.5 N/m for the reaction zone.

Table 10. Average toughness values of constituent materials.

Material	Specimen Geometry	Qlc*, MPa√m
Zirconia/Zirconia Joints		
Joint (MASZ-67, 1350 C)	Notched Bend Bar	2.48
Joint (MASZ-67, 1350 C)	Cracked Disk	2.12
Bulk MASZ-67, 1350 C	Notched Bend Bar	2.05
Joint (MASZ-80, 1350 C processed)	Notched Bend Bar	3.17
Joint (MASZ-80, 1350 C processed)	Cracked Disk	2.46
Bulk MASZ-80, 1350 C processed	Notched Bend Bar	2.82
Joint (MASZ-67, 1400 C processed)	Notched Bend Bar	1.59
Bulk MASZ-67, 1400 C processed	Notched Bend Bar	1.74
Joint (MASZ-80, 1400 C processed)	Notched Bend Bar	2.33
Bulk MASZ-80, 1400 C processed	Notched Bend Bar	5.27
Heat-Treated Zirconia, 1350 C processed	Notched Bend Bar	5.57
Zirconia/NCI Joints		
Zirconia/NCI Joint	Notched Bend Bar	5.89
Zirconia/NCI Joint	Cracked Disk, 0-degree	6.63
As-Received Zirconia	Notched Bend Bar**	9.70
As-Received Zirconia	Cracked Disk, 0-degree	8.60

* Qlc = Klc for monolithic materials, and it corresponds to apparent Mode I fracture toughness for joints.
** Chevron-notched bend bar.

For predicting mixed-mode fracture conditions, it is important to determine the variation of the critical strain energy release rate, G_o, as a function of mode mixity, Ψ. Evans and Hutchinson[8] have suggested a function of the form,

$$G_o / (Cos^2 \psi + k\, Sin^2 \psi) \tag{38}$$

for joints, where G_o is the critical strain energy release rate under pure Mode I loading and k is a material constant. The analysis of data on monolithic ceramic materials indicated that a function of the form

$$G_c = G_o Sec^2 (\psi/\psi_o) \tag{39}$$

represents the monolithic data very well, where Ψ_o is a constant depending upon the material. Based on this evaluation, the functional form given by Equation (39) was selected apriori for the JAD model. The value of G_o was determined from testing bulk interlayer cracked bend bars (for zirconia/zirconia joints), and from the preliminary validation results using cracked bend bars (for zirconia/NCI joints). However, the value of Ψ_o was not known.

It was decided that the data from cracked disk specimens would be used for determining Ψ_o. Because the cracked disk specimen data were also used for validation of the JAD model, it was decided that only one data-point from the disk specimens would be used for evaluating Ψ_o, and then the rest of the disk data would be used for comparing predicted and measured fracture loads.

Table 11 provides the apparent mixed-mode fracture toughness data for the cracked disk specimens. The analytical results of Atkinson et al.,[7] for homogeneous material were used for computing the apparent stress-intensity factors from the failure loads. As already indicated, Atkinson's results were within 3 percent of the FEM results on zirconia/NCI cracked specimens, primarily because of the good matching of the elastic constants of zirconia and NCI. From the apparent stress-intensity values, the local stress intensity factors and G at the interlayer location were calculated using the JAD model calculations, and these local G values were plotted versus Ψ. Figures 37 and 38 are plots of local $G(\Psi)$ versus Ψ for zirconia/zirconia and zirconia/NCI joints, respectively. Although there is only one data-point corresponding to each value of non-zero Ψ, the results at $\Psi = 0$ show a degree of scatter in the joint toughness. The solid curves in Figures 37 and 38 were obtained by using the data at $\Psi = 72.3$ degrees, and equating G_o with the average of G at $\Psi = 0$ degree ($G(0) = 20.9$ N/m for zirconia/zirconia joints, and 237.7 N/m for zirconia/NCI joints), thereby calculating Ψ_o according to Equation (39) above. An angle of 72.3 degrees was selected for determining Ψ_o because it was a sufficiently large angle to estimate mixed-mode effects, and also because it was sufficiently removed from 90 degrees, where crack-face rubbing could mask out true toughness values. However, any other angle could in principal be chosen (such as, say, 45 degrees), although an angle between 65 and 80 degrees is desirable because it spans a reasonably large range of Ψ.

Using the above approach, values of Ψ_o of 1.14 and 1.49 were obtained for the zirconia/zirconia and zirconia/NCI joints, respectively. These values, together with the G(0) data, were substituted into Equation (39) to obtain the solid curves in Figures 37 and 38. Figure 37 shows that the solid curve appears to represent the data trend quite well, except at conditions approaching 90 degrees. The lack of agreement may partly be due to the fact

Table 11. Results of fracture tests on cracked and uncracked disk specimens.

Specimen Number	Thickness, B mm	Diameter, D mm	Crack Length, 2a mm	Angle, Degrees	Load, P N	QI*, MPa√m	QII*, MPa√m	Ψ Degrees	G, local** N/m
Zirconia/Zirconia Joint With MASZ-67 Interlayer									
Uncracked Disk Specimen									
HP22-UD1	2.41	27.43	0.00	30.0	5785.0	-	Sh. St.=96.5 MPa	-	
HP22-UD4	2.43	27.43	0.00	10.0	7120.0	-	No Failure	-	
Cracked Disk Specimen									
HP22-CD3	2.53	27.43	12.70	0.0	1441.8	2.47	0.00	0.0	27.9
HP22-CD1	2.43	27.43	11.51	30.0	2202.8	-1.21	6.07	101.3	98.4
HP22-CD4	2.53	27.43	11.94	15.0	2225.0	1.96	3.99	63.8	78.6
HP23-CD2	3.59	35.56	16.51	0.0	2047.0	2.08	0.00	0.0	19.8
HP23-CD3	3.59	35.56	16.51	0.0	2314.0	2.35	0.00	0.0	25.2
HP24-CD2	3.62	35.56	16.51	0.0	1691.0	1.72	0.00	0.0	13.5
HP24-CD3	3.61	35.56	16.51	0.0	1958.0	1.98	0.00	0.0	17.9
HP24-CD4	3.60	35.56	15.49	22.5	3168.4	0.27	4.86	86.8	78.9
HP24-CD5	3.63	35.56	16.51	10.0	2296.2	1.88	2.02	47.1	32.7
HP23-CD4	3.63	35.56	14.99	18.0	3982.8	1.60	5.02	72.3	103.8
Zirconia/Zirconia Joint With MASZ-80 Interlayer									
HP25-CD4	3.63	35.56	16.51	0.0	2420.8	2.46	0.00	0.0	-
Zirconia/Nodular Cast Iron Joint									
LMC3-CD2	3.63	35.56	17.78	0.0	4138.5	4.73	0.36	4.4	116.2
LMC3-CD3	3.69	35.56	16.00	15.0	6630.5	3.67	7.80	64.8	334.1
LMC4-CD1	3.59	35.56	17.78	0.0	6764.0	7.82	0.60	4.4	317.7
LMC4-CD4	3.63	35.56	17.78	0	6408.0	7.33	0.56	4.4	279.13
LMC5-CD3	3.61	35.56	17.78	10	6319.0	5.46	5.86	47.0	311.66
LMC5-CD6	3.62	35.56	16.51	20	8544.0	2.18	12.88	80.4	687.25
LMC5-CD7	3.63	35.56	14.99	18	8588.5	3.44	10.78	72.3	541.06

* QI and QII correspond to apparent Mode I and Mode II stress intensity factors for joints.

** G, local = (fs^2)*{(QI^2)+(QII^2)}/E', is the local strain energy release rate in the interlayer location. fs is a shielding factor that local stress intensity factor, and arises from modulus mismatch effects.

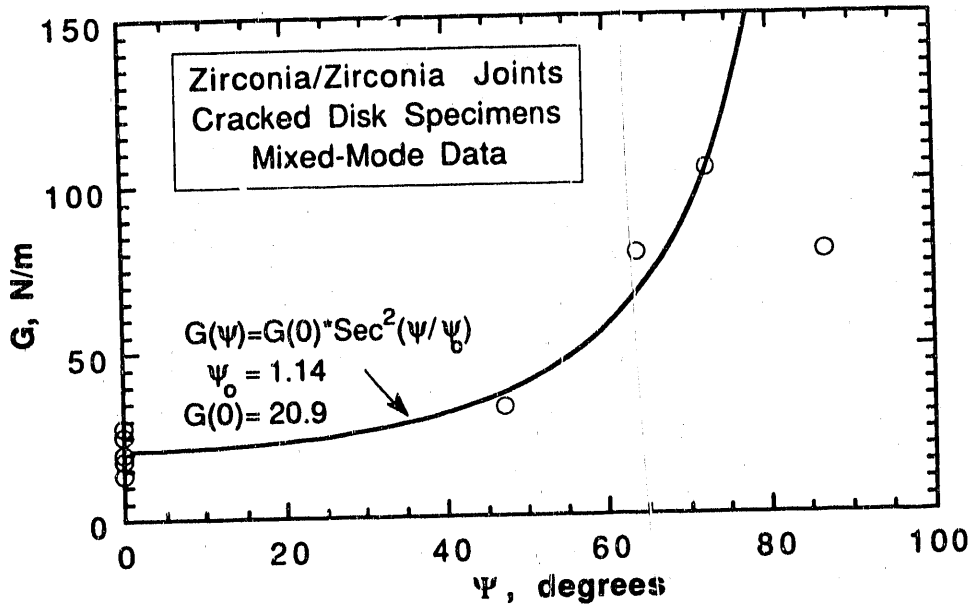

Figure 37. Strain energy release rate as a function of mode mixity for zirconia/zirconia specimens.

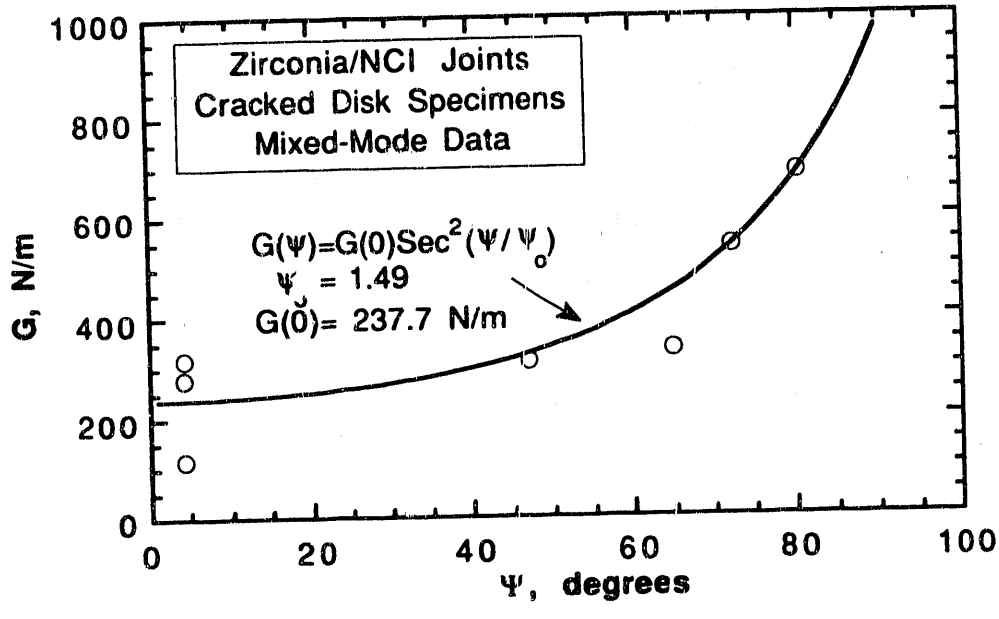

Figure 38. Strain energy release rate as a function of mode mixity for zirconia/NCI specimens.

that at angles approaching 90 degrees, closure of crack surfaces can provide erroneous results. More likely, a larger data base is necessary to evaluate whether the data at 86.8 degrees is indeed an outlier or whether the functional form shown in Equation (39) needs to be modified. For the zirconia/NCI joints, the solid curve provided excellent correlation with most of the data.

In the final validation of the JAD model, the above values of Ψ_o, together with values of G_o obtained earlier from experiments on bulk interlayer material, were used for assessing fracture under mixed-mode conditions; note that average G(0) (at $\Psi = 0$ degree) for disk specimens were not used in the final validation of the JAD model.

Figures 39 to 42 are load-displacement plots of zirconia/zirconia and zirconia/NCI disk specimens. The COD displacements were measured across the crack mouth at a distance of 3.81 mm on either side of the slit. Some amount of non-linearity is observed for the zirconia/NCI joint (Figure 42), and may have been the result of small scale plasticity prior to fast fracture. The experimental and predicted load-displacement plots were not compared in this program. However, the experimental traces are provided for future reference and for further validation of the JAD analysis.

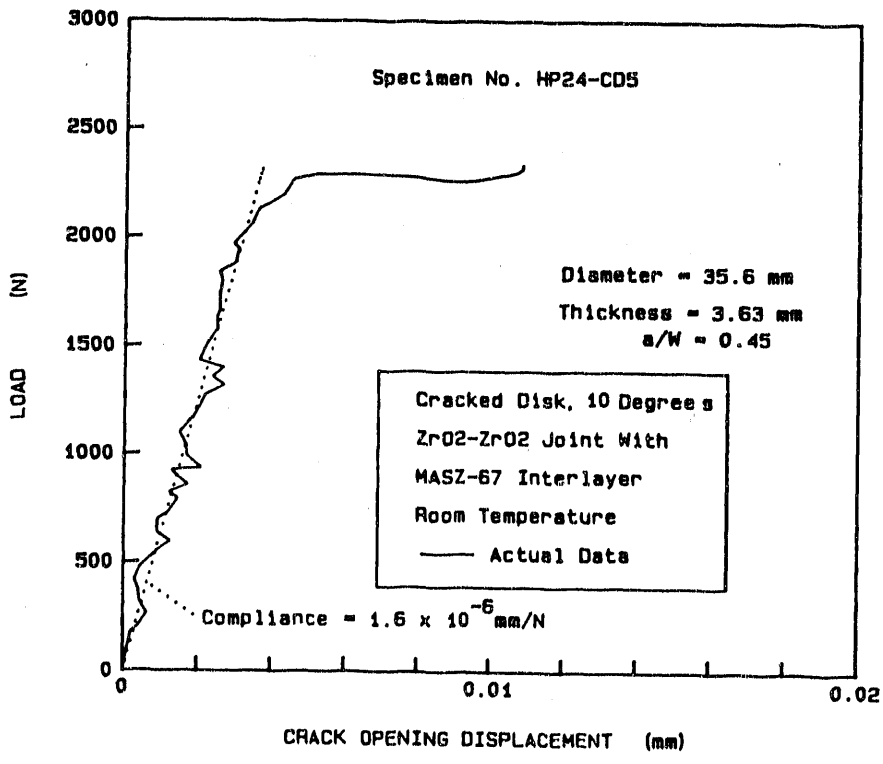

Figure 39. Load versus crack opening displacement plot for a zirconia/zirconia cracked disk specimen. Specimen loaded at 10 degrees to joint.

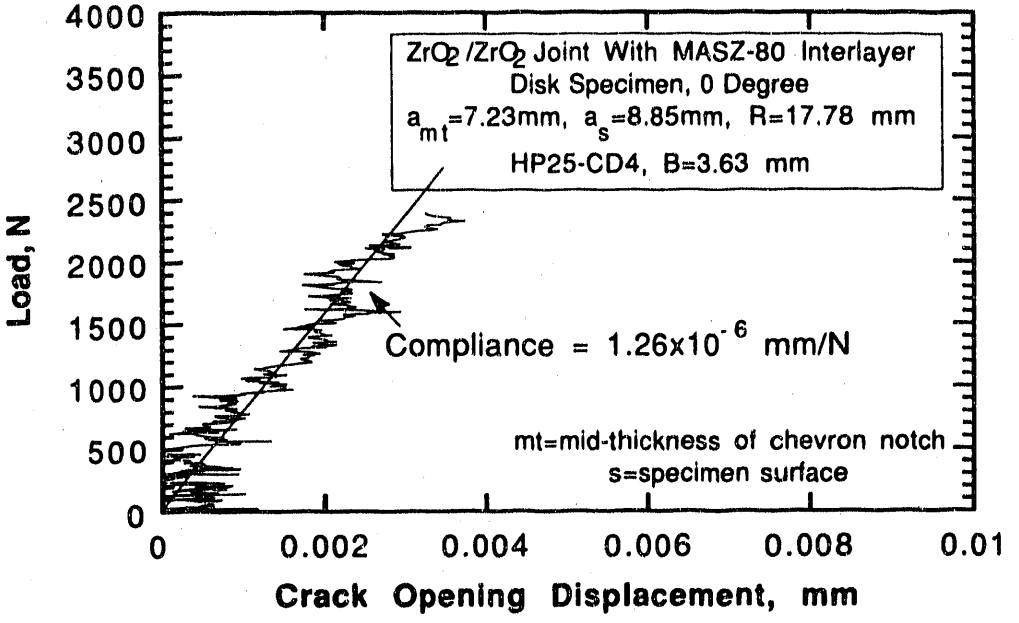

Figure 40. Load versus disk crack opening displacement plot for a zirconia/zirconia disk specimen.

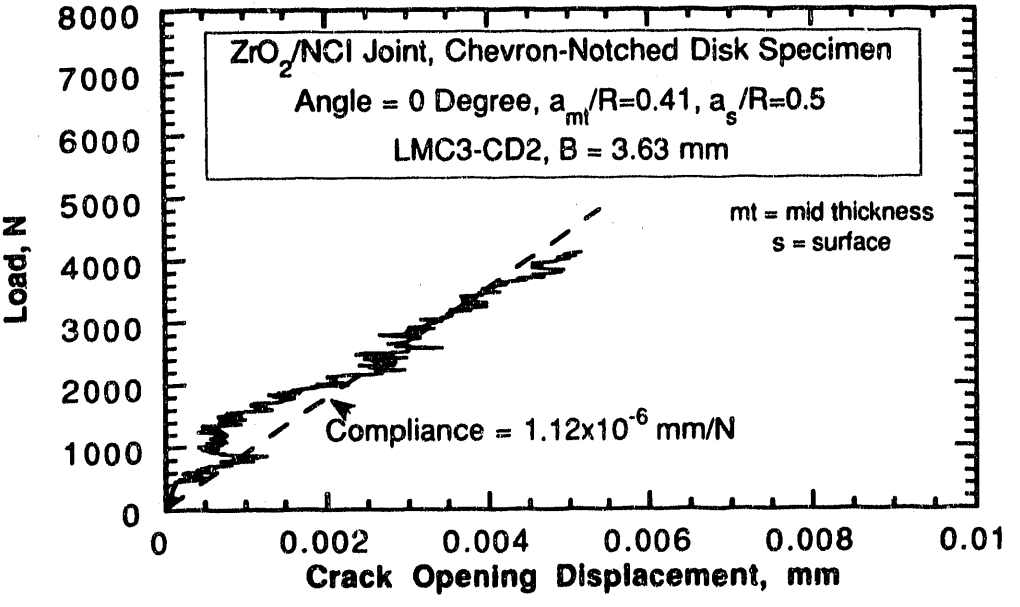

Figure 41. Load versus disk crack opening displacement plot for a zirconia/NCI cracked disk specimen. Specimen loaded at 0 degrees to joint.

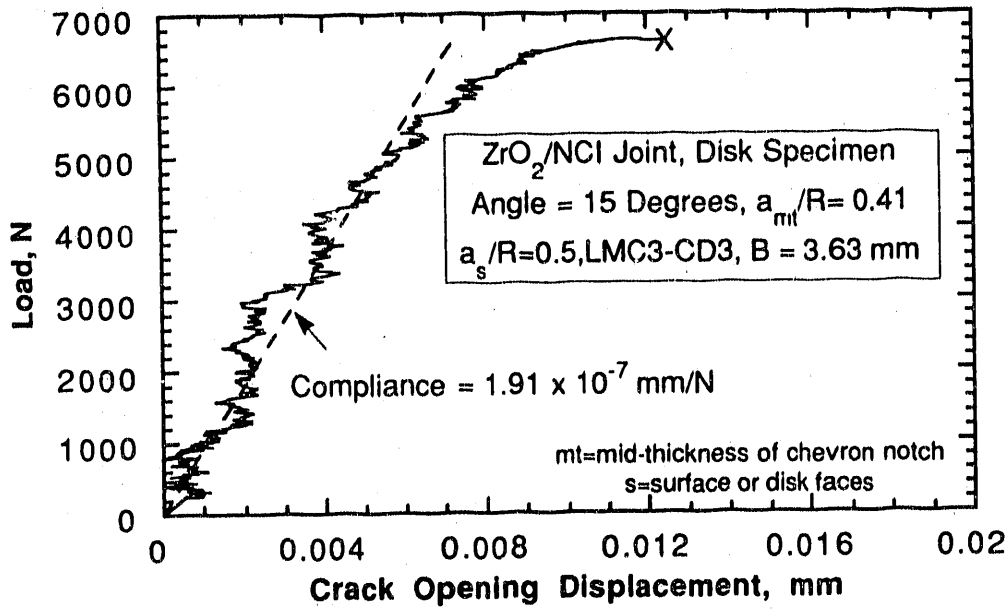

Figure 42. Load versus disk crack opening displacement plot for a zirconia/NCI cracked disk specimen. Specimen loaded at 15 degrees to joint.

3.3.3 Microstructure and Fractography of Joints

Zirconia/Zirconia Joints. Figure 43 is a microprobe back scattered electron (BSE) image of a joint fabricated with MASZ-67 interlayer at 1350 C. The figure shows that the joint had a thickness of approximately 150 μm, and the diffused reaction zones extended approximately 50 μm from the joint surfaces. The three largest dark areas in Figure 43 correspond to pores or joint defects, but the smaller dark regions are not pores. Those regions appear dark in the figure because of the higher concentration of lighter atomic-weight elements.

Higher magnification micrographs[5] indicated that the bright white circular particles in the figure were retained zirconia particles. X-ray diffraction results[6] showed that the particles were primarily tetragonal zirconia rather than monoclinic zirconia, although nominally pure zirconia powder was used in preparing the MASZ interlayer. These retained tetragonal zirconia particles explain why improved joint properties were observed with increased zirconia concentration in the interlayer. The dark phase in Figure 43 contained a high concentration of magnesia, and the blocky grey phase was evaluated to be zircon ($ZrSiO_4$), most likely produced by the reaction of zirconia with silica. The undesirable formation of zircon reduced the bond properties, and explains why a minimum of 67 weight-percent zirconia was needed in the interlayer material for producing acceptable bond strengths. Microprobe investigations also indicated that Mg and Si were primarily responsible for good wettability between the interlayer and the substrate.

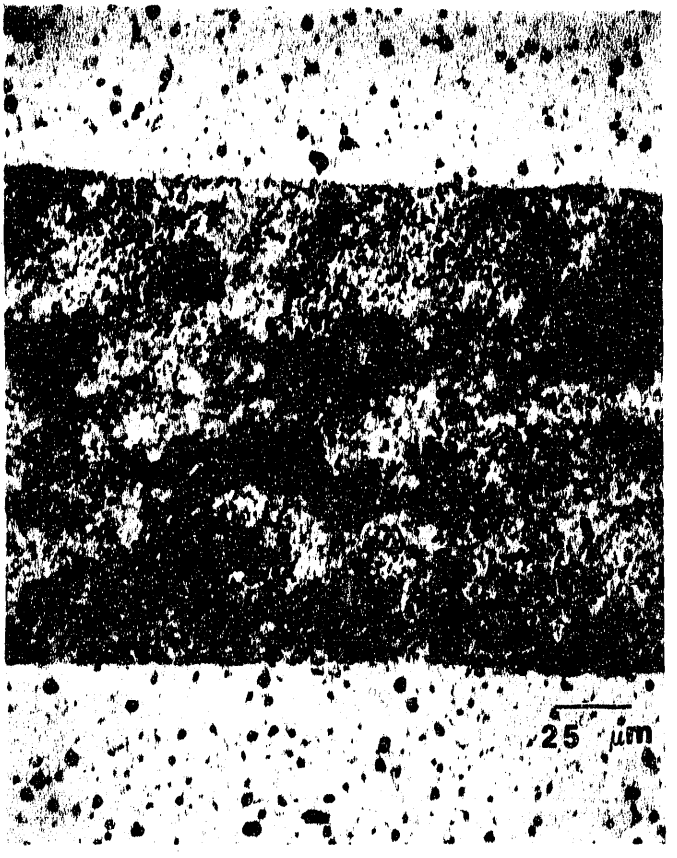

Figure 43. Microprobe BSE image of a large scale zirconia/zirconia joint fabricated using MASZ-67 interlayer.

Figure 44 is a fractograph of the base zirconia, and it shows that the base material had a substantial concentration of pores. These pores were located primarily at grain boundary triple points. For the joining experiments, the pores acted as preferential sites for accumulation of Mg and Si, since high concentrations of those elements were observed in metallographic specimens in the broad reaction zones on either side of the joint.

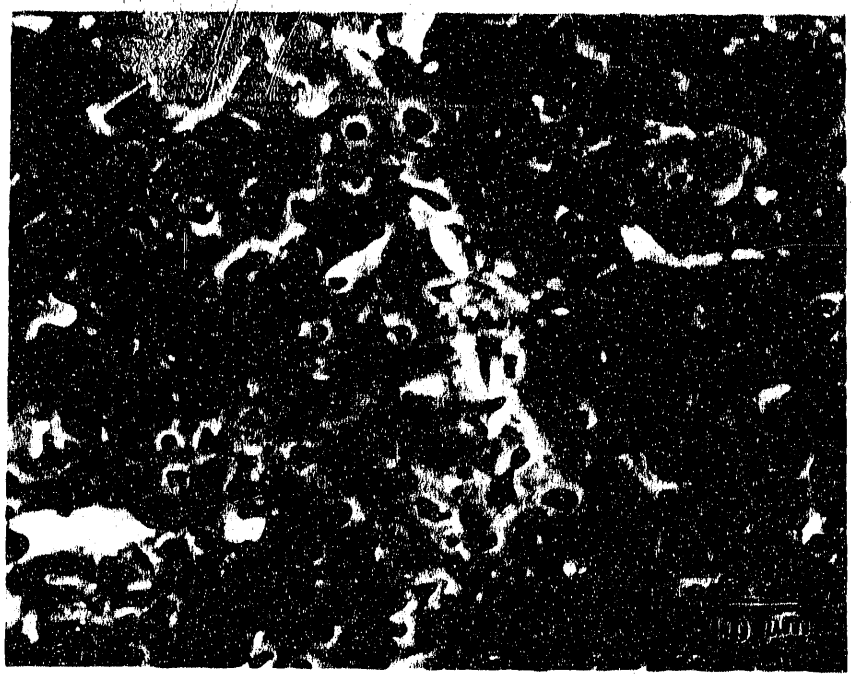

Figure 44. SEM micrograph of fracture surface of as-received zirconia.

On a macroscopic scale, the fracture surfaces of zirconia/zirconia joints were quite rough, indicating good fracture toughness. Figure 45 illustrates the fracture surface of a joint fabricated with the MASZ-67 interlayer. The fracture surface has a close resemblance to the microstructure of the interlayer material in that fine particles can be observed in a smooth-textured matrix. Energy dispersive spectroscopic (EDS) analyses provided the following approximate elemental composition (weight percent) of the fracture surface: 5.6 Mg, 7.1 Al, 14.4 Si, 5.7 Ti, 67.2 Zr. From the elemental composition, and the fracture surface morphology, it was concluded that the failure propagated primarily through the interlayer material.

Although most of the bend bars showed that the preferred fracture path was through the interlayer, there were a few instances where the crack appeared to propagate partly through the reaction zone. However, the bend strengths in these instances were not

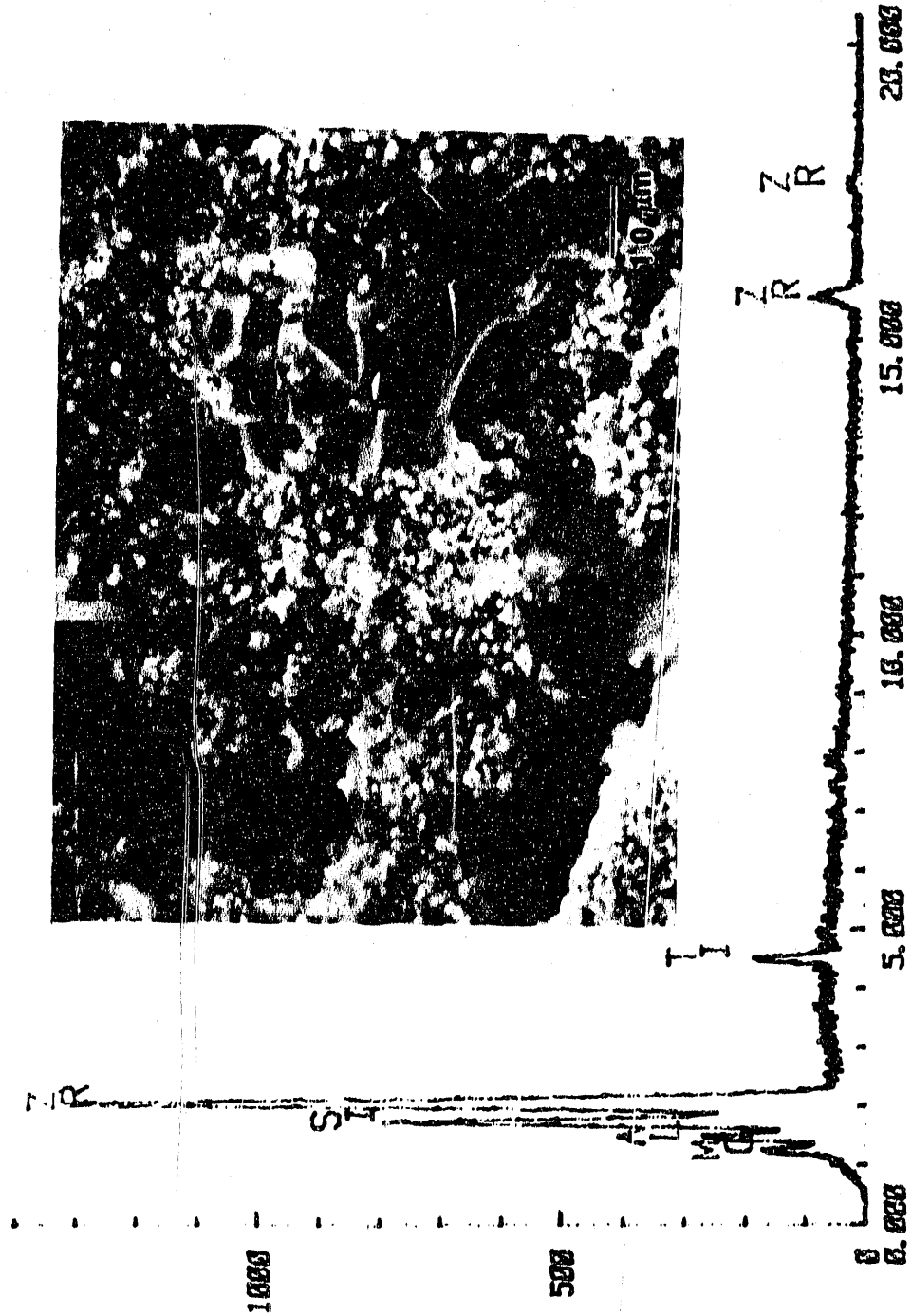

Figure 45. SEM micrograph and corresponding EDS trace of a zirconia/zirconia joint fabricated with MASZ-67 interlayer. The micrograph and EDS trace indicate that the crack propagated through the MASZ-67 interlayer.

significantly different compared with the case where the crack propagated completely through the interlayer, indicating that the reaction zone had a strength that was similar to the interlayer. In the particular case of a zirconia/zirconia joint fabricated with MASZ-80 interlayer at 1400 C, the failure propagated completely through the reaction zone rather than the interlayer. This behavior was consistent with the fact that the bulk interlayer fabricated at that temperature had a toughness of greater than 5 MPa√m, whereas the reaction zone was estimated to a have a toughness of only 2.4 MPa√m (much less than the heat treated zirconia, 5.6 MPa√m).

Zirconia/NCI Joints. Figure 46 contains electron microprobe images of a zirconia/NCI joint. Figure 46b is a BSE image based on Figure 46a, and shows the braze-metal/zirconia interface at a high magnification. The white region in this figure is primarily Ag, although Cu and In are also present. Figures 46c and 46d are Ti and Cu elemental maps, respectively, corresponding to Figure 46b. These figures indicate that there is primarily a pure Ti-layer (may contain oxygen) at the zirconia interface, followed by a Cu-Ti layer immediately adjacent to the pure Ti-layer. Clearly Ti was responsible for good bonding between the zirconia and the braze metal. Although the zirconia next to the braze metal did not appear to be microstructurally different from the as-received zirconia, a dark-brown band (0.3-0.4 mm wide) could easily be observed in the zirconia next to the braze metal; the as-received zirconia had a yellow color. This region corresponded to the reaction layer, and work done at ORNL indicated that the reaction zone corresponds to non-stoichiometric zirconia (ZrO_{2-x}) with depleted oxygen content.

Figures 47a and 47b are fractographs of the NCI side and the zirconia side, respectively, of a zirconia/NCI joint broken under Mode I loading. EDS analyses indicated that the void containing projections (region A3) in Figure 47a were composed of pure zirconia, indicating that the propagating crack dug into the reaction zone of the zirconia. The flatter regions, such as A4, contained primarily Ti and Cu, with Ti being the dominant element. On the zirconia side (Figure 47b), regions such as A2 corresponded to some braze metal pockets held back by the zirconia. The smooth regions (such as A1a) corresponded to the zirconia surface, but it was found to contain Ti and Cu, with Ti again being the dominant element. On the other hand, regions such as A1B corresponded to pure zirconia, being exact counterparts of the projected regions shown in Figure 47a. Thus, these fractographs indicate that the crack propagated partly through the reaction zone of the zirconia and partly through the extremely fine Ti-rich layer between the braze metal and the zirconia. Based on an examination of a number of fracture surfaces, the reaction-zone and Ti-rich layer each occupied between 40 and 60 percent of the area of the fracture surface.

Figure 48 illustrates the microstructure of a surface obtained by sectioning perpendicular to the fracture plane. The left side contains the NCI and braze metal, the central region corresponds to a space, and the right side corresponds to zirconia. The fracture halves were not correctly positioned when preparing the metallurgical sample, so that the fracture regions are not matching halves. Nevertheless, the micrographs illustrate the general fracture morphology. The micrograph shows that the crack propagated partly through the reaction zone of the zirconia and partly through the Ti-rich zone of the braze-metal/zirconia interface.

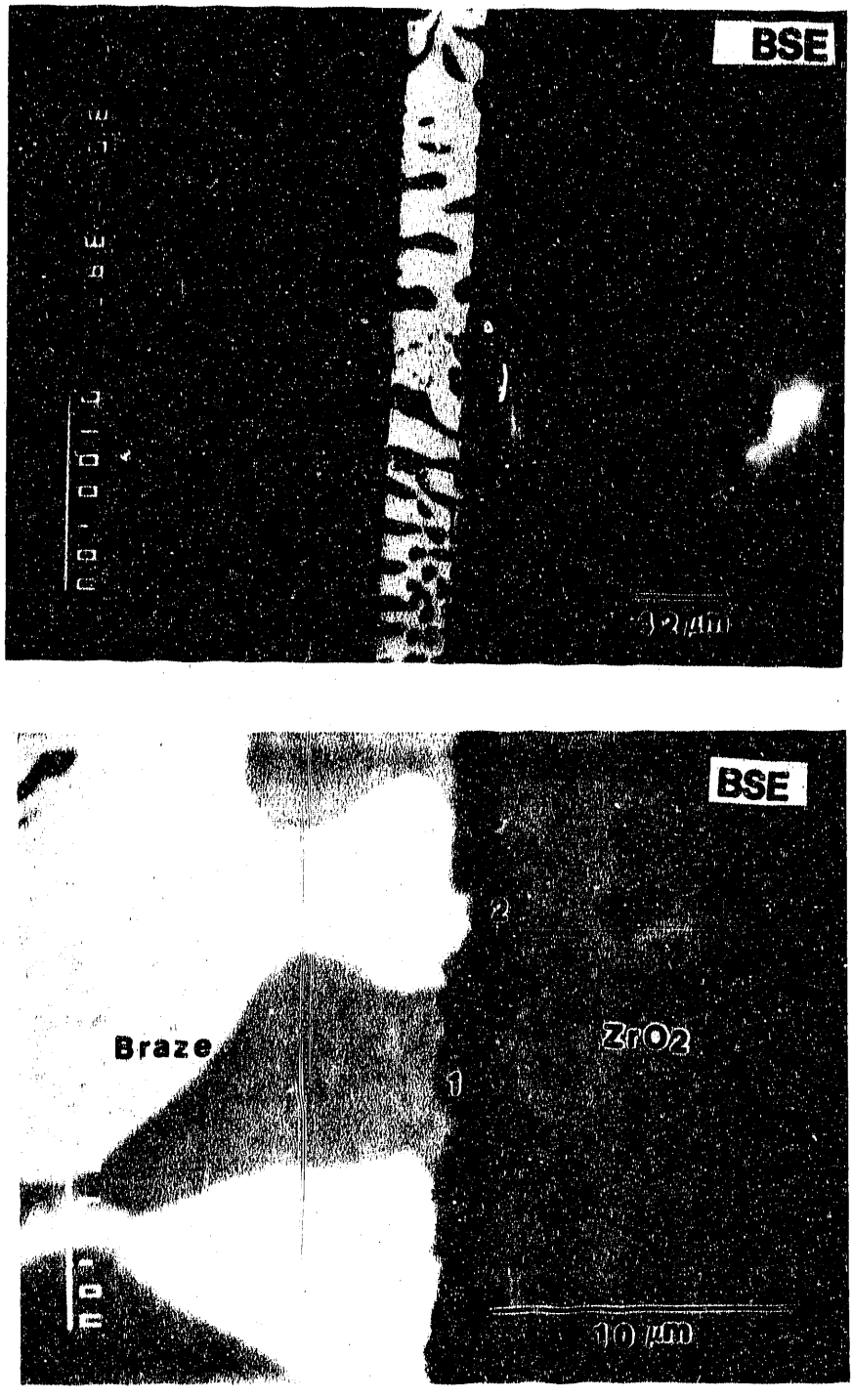

Figure 46. Microprobe BSE image and elemental maps for a zirconia/NCI joint. (a) low magnification micrograph with NCI on left side, braze in the middle, and zirconia on the right side. (b) BSE image of the braze/zirconia interface at a high magnification. (c) and (d) are Ti and Cu maps, respectively, of the same region as (b).

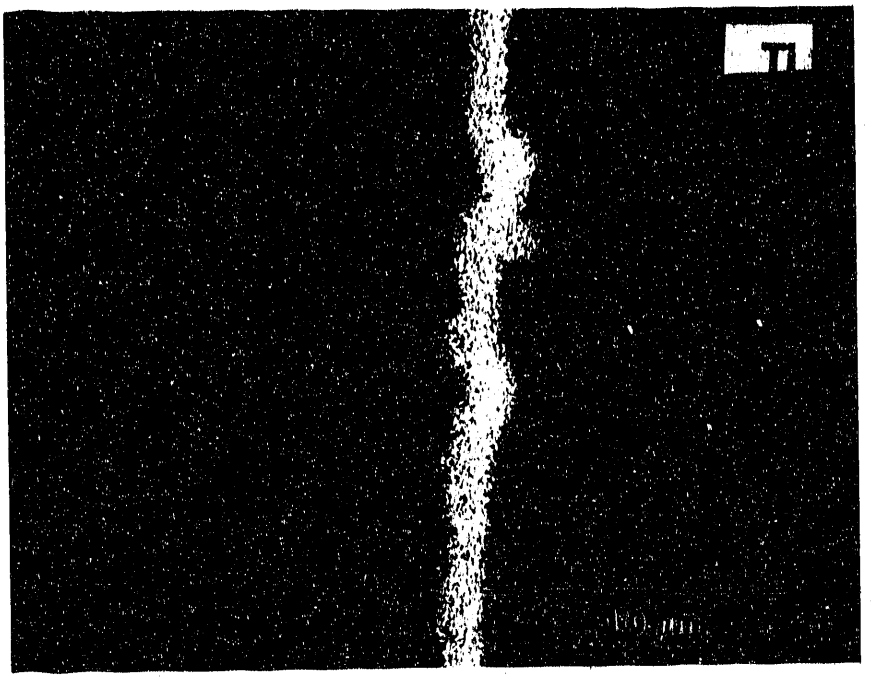

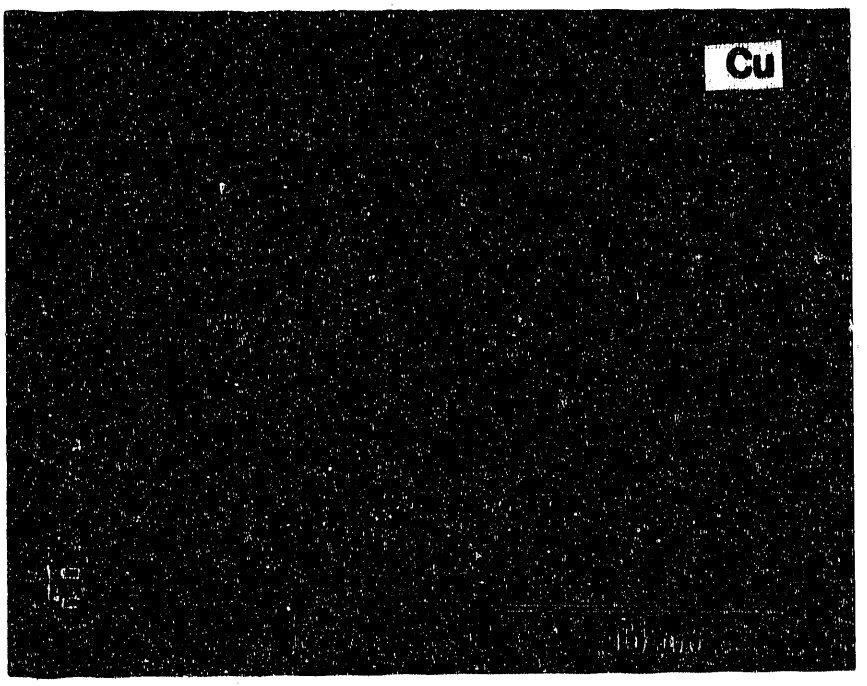

Figure 46. Cont.

NCI Side

(a)

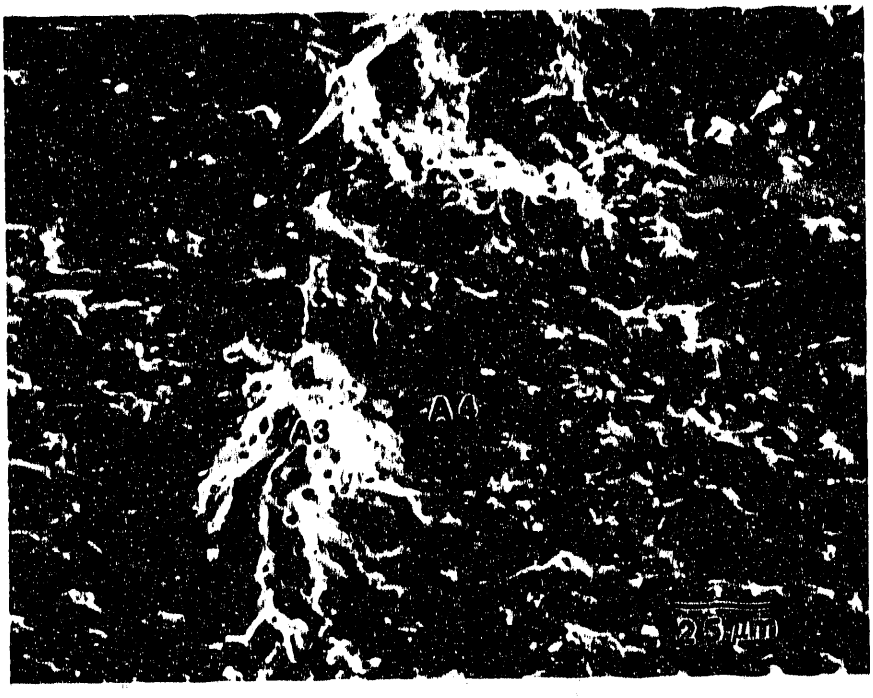

84139

ZrO_2 Side

(b)

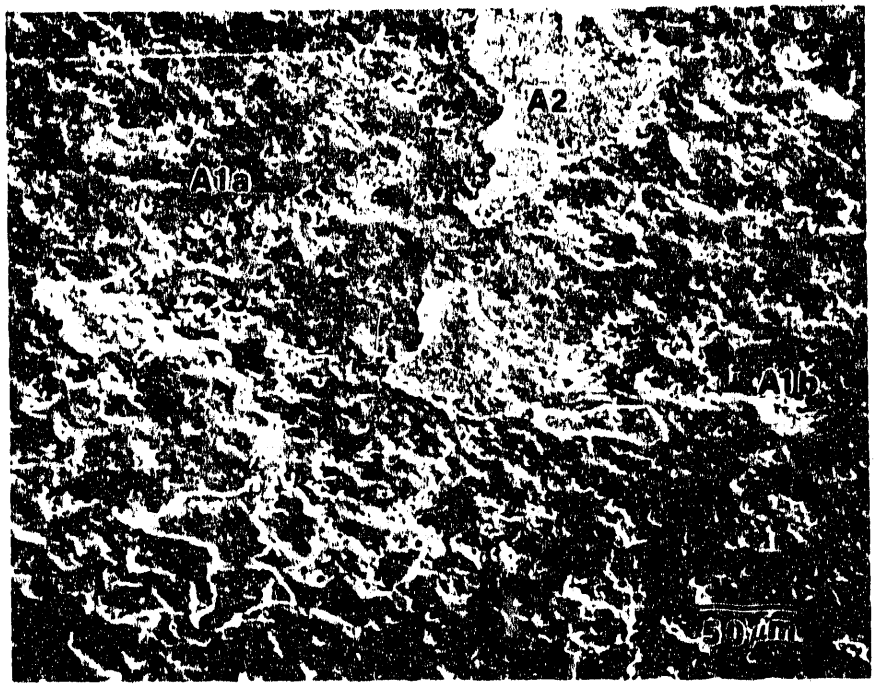

84141

Figure 47. Fracture surfaces of a zirconia/NCI joint for a notched bend bar. (a) NCI side of the fracture surface. (b) zirconia side of the fracture surface.

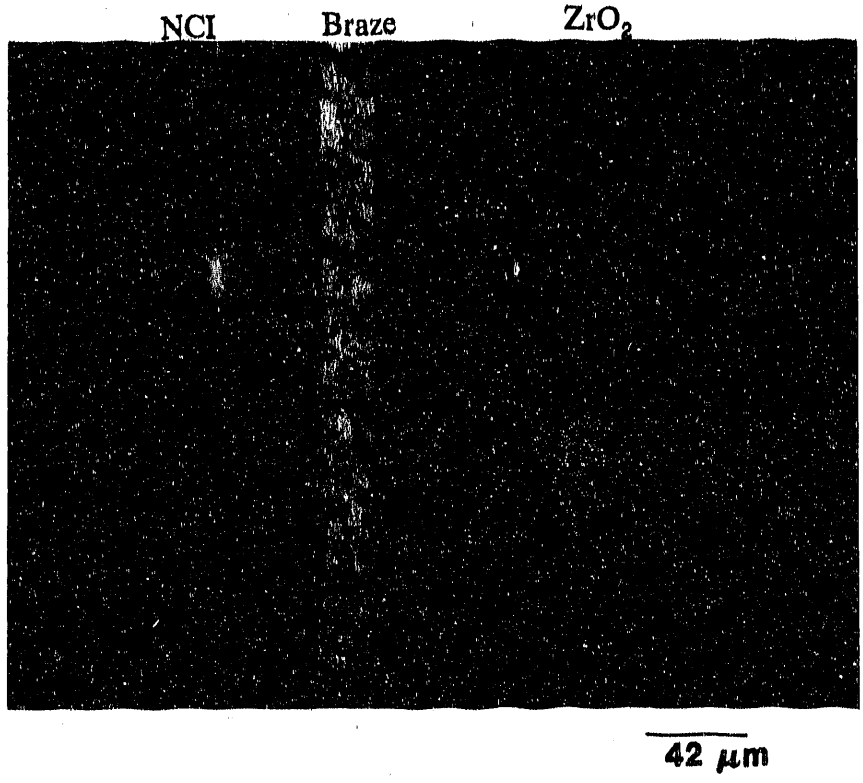

Figure 48. Microstructure of the NCI (left) and zirconia (right) immediately adjacent to the fracture surface. the cross-sections are not matching halves of the fracture surface.

With increased mixity of loading (increasing ψ), there was a gradual change in the fracture path and fracture morphology. On the zirconia side of the disk specimen, the crack deviated from the notch plane and propagated towards the loading point. This behavior was similar to what has been observed for monolithic ceramic specimens. The extent of crack growth along the bond-line prior to crack deviation (for zirconia side) depended on the loading angle, being approximately 6 mm for an angle of 10 degrees, and being less than 1 mm above 15 degrees. On the NCI side, however, the crack could not propagate into the NCI; rather the crack propagated all along the bond line. Figures 49a and 49b correspond to the NCI side and zirconia side, respectively, of the fracture surfaces of a disk specimen where the crack propagated through the bond line. The sample was loaded with the notch at an angle of 20 degrees with respect to the load line (ψ = 80.4 degrees). EDS analysis indicated that on the NCI side the surface layer was rich in Ti and Cu, with Ti being the dominant element. However, contrary to Mode I fracture, hardly any zirconia was found on the fracture surface. The wavy structure seen in Figure 49a probably corresponds to shear deformation of the Ti-rich layer and of the braze metal beneath it. On the zirconia side, the primary elements detected were Zr and Ti and Cu. Here too, unlike Figure 47b, very little zirconia appeared to have been pulled out by the braze metal during fracture. Overall, it appeared that under shear loads there was significant plastic shear deformation of the braze metal, including the Ti-rich layers, and these resulted in shear failure of the interface without any significant accompanying failure of the reaction zone of the interlayer. Such fracture morphology differences with the Mode I loading probably were responsible for elevating the G_c with increasing ψ.

(a)

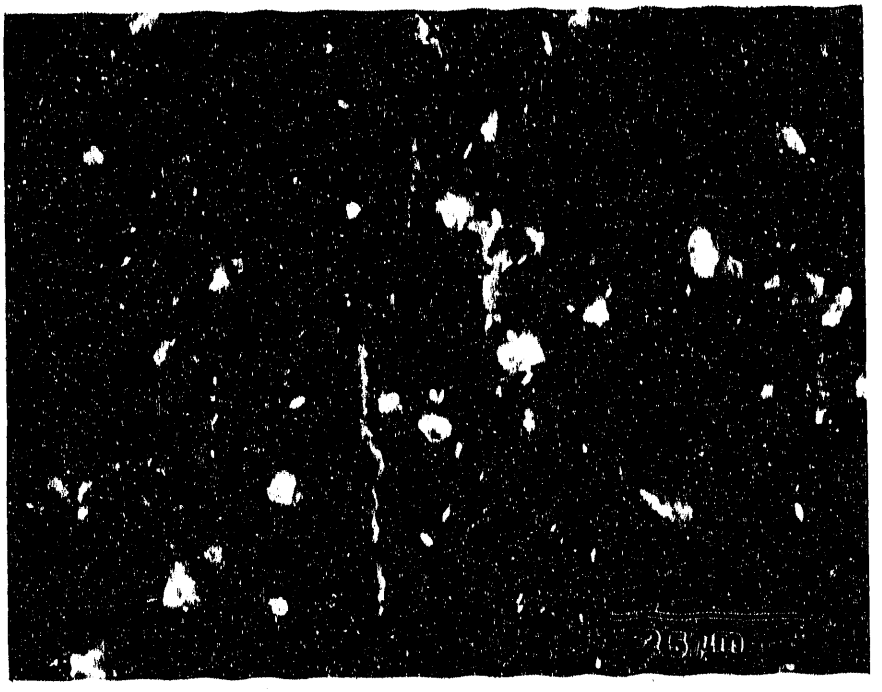

86172

(b)

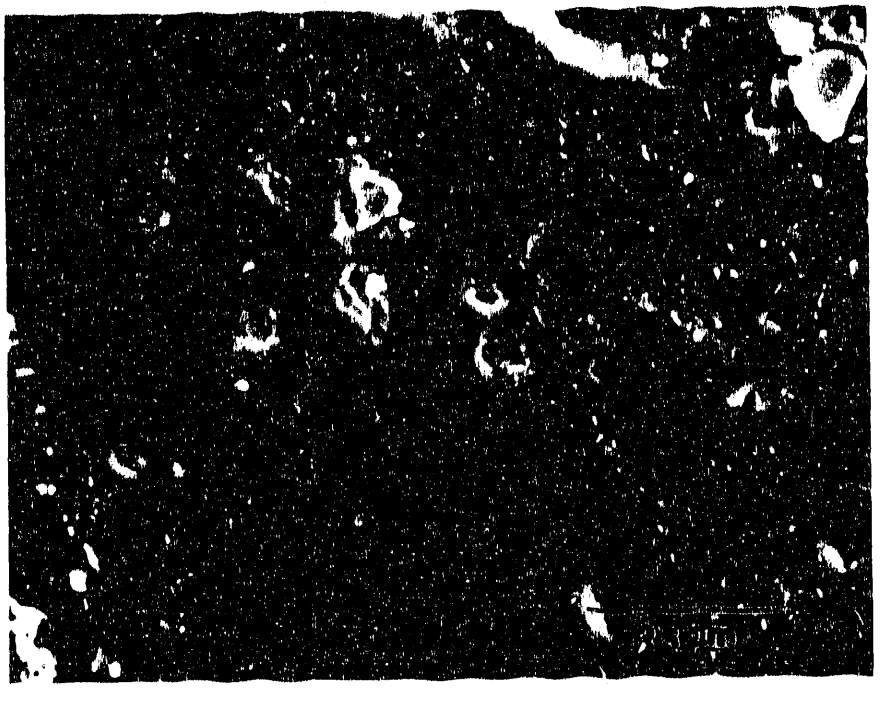

86167

Figure 49. Fracture surfaces of a zirconia/NCI joint for a cracked disk specimen, with the crack at an angle of 20 degrees (Ψ = 80.4 degrees) with respect to the load line. (a) NCI side of the fracture surface. (b) Zirconia side of the fracture surface.

4.0 VALIDATION

Validation of the JAD model was performed in two steps:

1. Preliminary validation, where the model predictions were compared with measured failure loads of notched and unnotched bend bars.

2. Final validation using cracked disk specimens that contained 20 times more bonding area than bend bars, and comparing the predicted failure loads with measured failure loads.

The joint assessment diagrams for four representative specimens were presented earlier. Calculations like those were conducted to predict the failure loads of cracked disk and bend bar specimens. Predictions of the strength of unnotched bend bars were performed only on zirconia/zirconia joints and they were based on the strength of the ceramic interlayer, appropriately modified to account for shielding effects due to moduli mismatch.

Figure 50 provides comparisons of measured and predicted failure loads and is a plot of the data displayed in Table 12. The figure includes data from zirconia/zirconia and zirconia/NCI joints, unnotched and notched bend bars, and cracked disk specimens loaded at various angles to the crack. Each data point is an average of several readings, particularly for the bend bar specimens. Thus, the plot contains an extensive database.

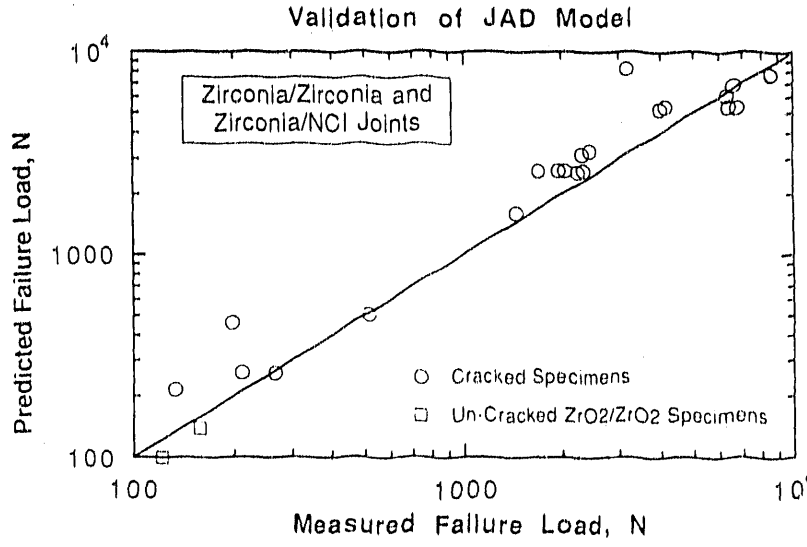

Figure 50. Results of validation analyses and testing with zirconia/zirconia and zirconia/NCI joints. The bend bars were used for preliminary validation and the disk specimens were used for final validation.

In Table 12, the geometric data needed to calculate the failure loads are also displayed. Shown for each experiment, where applicable, are the joining temperature, the specimen width, B, and depth, W, the half-crack length, a, the radius of the disk. R, the angle between the loading points and the crack, ϕ, the percent zirconia in the MASZ interlayer, and the calculated angle the assessment vector makes with the P_r-axis.

The comparisons between predicted and calculated failure loads are encouraging. The exceptions that appear are believed not to be due to errors in model calculations. Rather, we believe them to be the result of differences in failure path (for example, failure in the reaction zone of zirconia/zirconia joints fabricated at 1400 C) which could not be predicted a priori, and also degradation of the MASZ-67 interlayer in zirconia/zirconia joints. Note that the measured failure loads are consistently below the predicted failure loads for zirconia/zirconia joints fabricated using MASZ-67 interlayer. For these joints, if the results of preliminary validation are used to modify the G_c of the interlayer, then better agreement is obtained in the final validation. The exceptions in Table 12 point out the need to evaluate the crack path as part of any preliminary investigations, and to include some form of the process parameters in the JAD model calculations.

Overall, the degree of correlation between predicted and measured failure loads of different joints and with different specimen geometries strengthens the validity of the joint design model.

Joint Type	MASZ percent	Joining Temperature	Beam Depth, W mm	Width, B mm	Half-Crack Length, a, mm (a)	Radius, R mm	Crack Angle, Degrees	ϕ Degrees	Failure Load Computed, N	Failure Load Measured, N
Preliminary Validation (Bend Bars)										
Zirconia/Zirconia(b)	67	1350 C	5.08	1.55	1.55	-	-	64	260	211
Zirconia/Zirconia(b)	80	1350 C	5.08	1.63	1.63	-	-	70	260	267
Zirconia/Zirconia(b)	67	1400 C	5.08	1.63	1.63	-	-	64	215	134
Zirconia/Zirconia(b)	80	1400 C	5.08	1.60	1.60	-	-	80	460	198
Zirconia/Zirconia(c)	67	1350 C	2.54	2.54	-	-	-	-	100	122
Zirconia/Zirconia(c)	80	1350 C	2.54	2.54	-	-	-	-	140	158
Zirconia/NCI (b)	-	760 C	5.08	5.08	1.60	-	-	75	505	514
Final Validation (Cracked Disks)										
Zirconia/Zirconia	67	1350 C	-	2.53	6.35	13.72	0	79	1600	1442
Zirconia/Zirconia	67	1350 C	-	3.59	8.26	17.78	0	80	2600	2047
Zirconia/Zirconia	67	1350 C	-	3.59	8.26	17.78	0	80	2600	2314
Zirconia/Zirconia	67	1350 C	-	3.62	8.26	17.78	0	80	2600	1691
Zirconia/Zirconia	67	1350 C	-	3.61	8.26	17.78	0	80	2600	1958
Zirconia/Zirconia	67	1350 C	-	3.63	8.26	17.78	10	79	3135	2296
Zirconia/Zirconia	67	1350 C	-	2.53	5.97	13.72	15	77	2550	2225
Zirconia/Zirconia	67	1350 C	-	3.63	7.50	17.78	18	78	5200	3982
Zirconia/Zirconia	67	1350 C	-	3.60	7.75	17.78	22.5	75	8200	3168
Zirconia/Zirconia	80	1350 C	-	3.63	8.26	17.78	0	81	3250	2421
Zirconia/NCI	-	760 C	-	3.63	8.89	17.78	0	85	5350	4139
Zirconia/NCI	-	760 C	-	3.59	8.89	17.78	0	85	5291	6764
Zirconia/NCI	-	760 C	-	3.63	8.89	17.78	0	85	5350	6408
Zirconia/NCI	-	760 C	-	3.61	8.25	17.78	10	85	6100	6319
Zirconia/NCI	-	760 C	-	3.69	8.00	17.78	15	85	6850	6631
Zirconia/NCI	-	760 C	-	3.63	7.50	17.78	18	85	7750	8589
Zirconia/NCI	-	760 C	-	3.62	8.26	17.78	20	86	7690	8544

(a) a is the full crack length for notched bend bars, and half crack length for disk specimens.
(b) Average of multiple tests reported here.
(c) Un-cracked (smooth) bend bars. Average of multiple tests reported here.

Table 12. Validation results - comparisons of predicted and measured failure loads of joints.

5.0 CONCLUSIONS AND RECOMMENDATIONS

The most significant accomplishment of the work described in the present report is the development of an engineering model applicable to design improvement and structural integrity assessment of ceramic/ceramic and metal/ceramic joints. A novel modeling approach was adopted which marries state-of-the-art knowledge in mechanics of material interfaces with engineering fracture mechanics concepts. This resulted in a model which provides a rational link between constituent material properties and oining process variables, and load carrying capacity of a joint. As shown in Figure 51, the JAD model can be used for (a) assessing a given joint's load carrying capacity and (b) designing improvement by systematically changing constituent properties and joining process variables.

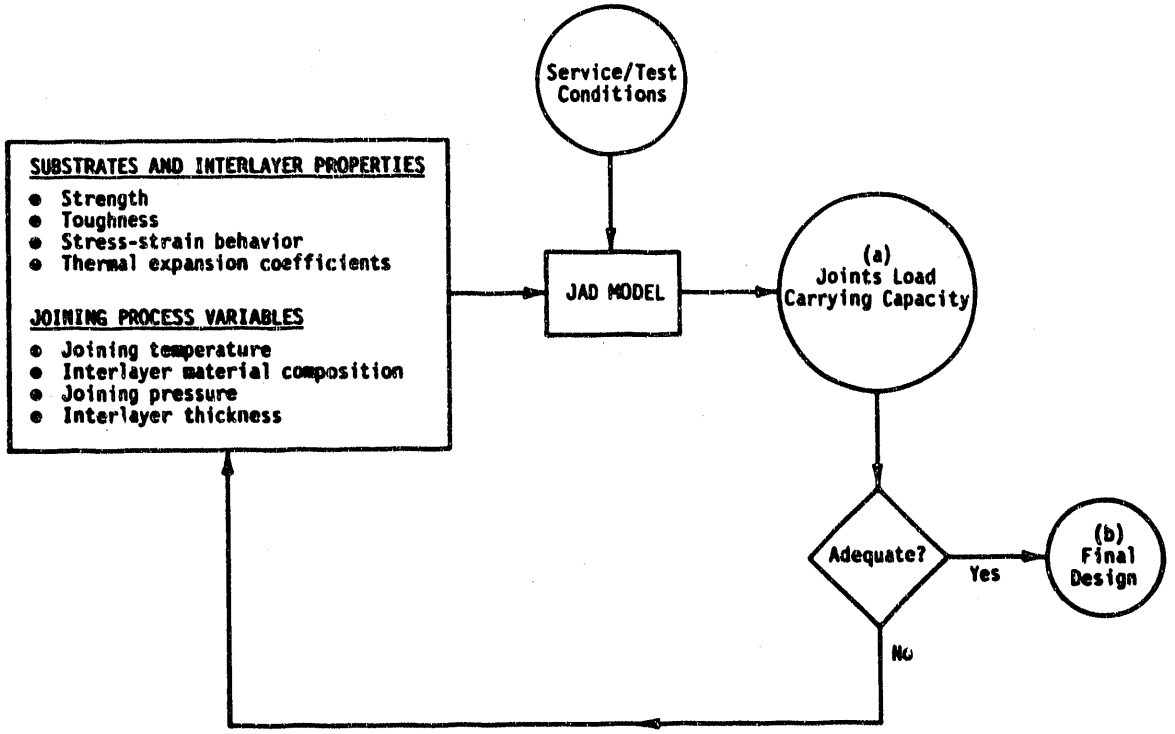

Figure 51. Role of JAD model: (A) structural integrity assessment and (b) joint design.

Besides the analytical modeling effort, extensive laboratory experimentation was performed involving fabrication and testing of zirconia/zirconia and NCI/zirconia joints. Remarkable success was achieved in fabricating zirconia/zirconia joints by a novel hot forging method. A versatile test specimen in the shape of a disk was introduced for characterizing joints. In addition to experiments on joints, which provided data for validating JAD model predictions, laboratory tests were performed to generate thermo-mechanical property data for each constituent material: zirconia, cast iron, braze and the interlayer material for zirconia/zirconia joints. These constituent property data were used as part of the input to the model.

The JAD model was validated by comparing predictions with the measured load carrying capacity of two significantly different joint configurations - the bend bar and the disk. The reasonably good agreement between predictions and measurements for both configurations indicates that the model is not geometry specific. Therefore, it would be useful in engineering applications involving other joint configurations.

Overall, the work represents a major step toward the development of an analytical design methodology for ceramic/ceramic and metal/ceramic joints. Nevertheless, the model does need additional validation and to be augmented to formulate a more generally useful joint design methodology.

Additional validation of the JAD model is most needed at elevated temperatures which are representative of engine operating conditions. Also, the model needs to be validated for crack sizes smaller than those used in the present work and more representative of typical flaw sizes anticipated in as-fabricated joints. It would also be worthwhile to assess the accuracy of the JAD model predictions for joints between other metals and ceramic materials than those included in the present work. For this purpose, the recent experiments by GTE Laboratories, Inc. and the Norton Company involving silicon nitride and Inconel joints may provide the needed data.

In its current state of development, the JAD model is only applicable for joints subjected to quasi-static, monotonically increasing loads. In engine applications, a joint is more likely to experience conditions which may consist of load reversals as well as dwell periods giving rise to relatively low sustained loads. Thus, creep, fatigue and possible subcritical crack growth under such conditions may give rise to failure mechanisms not considered in the present work. We recommend that future research be directed toward augmenting the JAD model to include creep and fatigue considerations.

Finally, it is recommended that the JAD model should be formulated in a probabilistic analysis framework to more meaningfully address the issue of joint reliability. Anticipating at the beginning of the present work that a probabilistic design model would eventually be needed, the JAD model was purposefully formulated in a manner such that its incorporation in a probabilistic analysis framework would be relatively straightforward. Because application of the JAD model does not require case by case finite element analyses, the model readily lends itself to practically useful probabilistic analyses which could be performed using a personal computer. In fact, the JAD model has already been implemented in a PC code which can be readily adapted for this purpose.

ACKNOWLEDGEMENTS

The authors would like to acknowledge the support and contributions of a number of people who have been influential to the progress of this work.

Foremost, we would like to acknowledge Dr. M. Santella of Oak Ridge National Laboratories who was the technical monitor on the program. He gave encouragement, technical guidance, and laboratory assistance in using the active substrate brazing technique. We would also like to recognize Dr. D. R. Johnson of Oak Ridge National Laboratories whose clarification of the program goals was largely responsible for the final form of our joint assessment and design methodology.

Others who made substantial contributions to the work are Dr. Frank. S. Honecy of the Surface Science Branch, NASA Lewis Research Center, Cleveland, Ohio, who provided (gratis) the RF-sputtered titanium coatings on the zirconia billets used in the active substrate brazing work; Drs. K. Sorenson and R. Salzbrenner of Sandia National Laboratories who contributed the nodular cast iron; Professor C. F. Shih of Brown University for providing finite element solutions for zirconia/NCI disk specimens and for valuable advice on interface fracture mechanics; Dr. William Lee of Cambridge University, England, who assisted in the design and microstructural characterization of zirconia/nodular cast iron joints; Mr. Paul Held of Battelle who conducted the material characterization and validation experiments; Mr. Andrew Skidmore of Battelle who performed the microscopy; Mr. George Wall of Battelle who performed the high temperature validation experiments; Mr. Roger Beal of Battelle who joined the zirconia/zirconia disks by hot forging; Mr. John Hunt of the Edison Welding Institute who prepared many metallographic specimens; and Ms. Connie Keels of Battelle whose care and accuracy in manuscript preparation are evident in this report.

Research sponsored by the U.S. Department of Energy, Assistant Secretary for Conservation and Renewable Energy, Office of Transportation Technologies, as part of the Ceramic Technology Project of the Advanced Materials Development Program, under contract DE-AC05-84OR21400 with Martin Marietta Energy Systems, Inc.

REFERENCES

1. C. F. Shih, V. Kumar, and M. D. German, "Studies on the Failure Assessment Diagram Using the Estimation Scheme and J-Controlled Crack Growth Approach", General Electric Company, TIS Report, (1981).

2. I. MIlne, et al, "Assessment of the Integrity of Structures Containing Defects", Central Electrify Generating Board Report, South Wester Region, CEGB, Bristol, U.K. (1978).

3. S. L. Swartz, B. S. Majumdar, and B. C. Mutsuddy, "Joining of Zirconia Ceramics", Proceedings of the 26th Automotive Technology Development Contractors Coordination Meeting, Dearborn, Michigan (1988).

4. S. L. Swartz, B. S. Majumdar, A. Skidmore, and B. C. Mutsuddy, "Joining of Zirconia Ceramics with a CaO-TiO_2-SiO_2 Interlayer", Material Letters, Vol. 7, No. 11, (1989).

5. B. S. Majumdar, S. L. Swartz, and A. T. Hopper, "Zirconia-Zirconia Joints - Part I, Fabrication and Microstructural Characterization", Submitted to J. American Ceramic Society (1990).

6. B. S. Majumdar, J. Ahmad, and A. R. Rosenfield, "Zirconia-Zirconia Joints - Part II, Mechanical Characterization and Analysis, submitted to J. American Ceramic Society (1990).

7. C. Atkinson, R. E. Smelser, and J. Sanchez, "Combined Mode Fracture via the Cracked Brazilian Disk Test", International J. of Fracture, Vol. 18, No. 4, pp. 279-291 (1982).

8. A. G. Evans and J. W. Hutchinson, "Effects on Non-planarity of the Mixed Mode Fracture Resistance of Bimaterial Interfaces", to be published in Acta Metall. (1990).

ORNL/Sub/87-SB046/1

INTERNAL DISTRIBUTION

1-2. Central Research Library
3. Document Reference Section
4-5. Laboratory Records Department
6. Laboratory Records, ORNL RC
7. ORNL Patent Section
8-10. M&C Records Office
11. L. F. Allard, Jr.
12. L. D. Armstrong
13. P. F. Becher
14. R. F. Bernal
15. T. M. Besmann
16. P. J. Blau
17. A. Bleier
18. E. E. Bloom
19. K. W. Boling
20. R. A. Bradley
21. C. R. Brinkman
22. V. R. Bullington
23. R. S. Carlsmith
24. P. T. Carlson
25. G. M. Caton
26. S. J. Chang
27. R. H. Cooper, Jr.
28. B. L. Cox
29. D. F. Craig
30. S. A. David
31. J. H. DeVan
32. J. L. Ding
33. M. K. Ferber
34. F. M. Foust
35. W. Fulkerson
36. R. L. Graves
37. D. L. Greene
38. M. H. Harris
39. E. E. Hoffman
40. C. R. Hubbard
41. M. A. Janney
42. M. G. Jenkins
43. D. R. Johnson
44. W. F. Jones
45. D. Joslin
46. R. R. Judkins
47. M. A. Karnitz
48. M. R. Kass
49-53. B. L. P. Keyes
54. H. D. Kimrey, Jr.
55. T. G. Kollie
56. K. C. Liu
57. E. L. Long, Jr.
58. W. D. Manly
59. R. W. McClung
60. D. J. McGuire
61. J. R. Merriman
62. D. L. Moses
63. T. A. Nolan
64. A. E. Pasto
65. J. L. Rich
66. C. R. Richmond
67. J M Robbins
68. M. L. Santella
69. A. C. Schaffhauser
70. S. Scott
71. G. M. Slaughter
72. E. J. Soderstrom
73. D. P. Stinton
74. R. W. Swindeman
75. V. J. Tennery
76. T. N. Tiegs
77. J. R. Weir, Jr.
78. B. H. West
79. F. W. Wiffen
80. S. G. Winslow
81. J. M. Wyrick
82. C. S. Yust

EXTERNAL DISTRIBUTION

83. James H. Adair
University of Florida
Materials Science and
Engineering
317 MAE Bldg.
Gainesville, FL 32611-2066

84. Donald F. Adams
University of Wyoming
Mechanical Engineering
Department
P. O. Box 3295
Laramie, WY 82071

85. Jalees Ahmad
AdTech Systems Research, Inc.
1342 North Fairfield Road
Dayton, OH 45432-2698

86. Yoshio Akimune
NISSAN Motor Co., Ltd.
Materials Research Laboratory
1 Natsushima-Cho
Yokosuka 237
JAPAN AIR MAIL

87. Mufit Akinc
Iowa State University
322 Spedding Hall
Ames, IA 50011

88. Ilhan A. Aksay
University of Washington
Materials Science and Engineering
Department, FB-10
Seattle, WA 98195

89. R. G. Alexander
BASE
26 Malvern Close
Kettering Northants NN16 AJP
UNITED KINGDOM AIR MAIL

90. Richard L. Allor
Ford Motor Company
Material Systems
Reliability Department
20000 Rotunda Drive
P.O. Box 2053, Room S-2031
Dearborn, MI 48121-2053

91. Richard T. Alpaugh
U.S. Department of Energy
Advanced Propulsion Division
CE-322, Forrestal Building
Washington, DC 20585

92. Joseph E. Amaral
Instron Corporation
Corporate Engineering Office
100 Royale Street
Canton, MA 02021

93. Edward M. Anderson
Aluminum Company of America
North American Industrial
Chemicals Division
P.O. Box 300
Bauxite, AR 72011

94. Norman C. Anderson
Ceradyne, Inc.
Ceramic-to-Metal Division
3169 Redhill Avenue
Costa Mesa, CA 92626

95. Don Anson
Battelle Columbus Laboratories
Thermal Power Systems
505 King Avenue
Columbus, OH 43201-2693

96. Thomas Arbanas
G.B.C. Materials Corporation
580 Monastery Drive
Latrobe, PA 15650-2698

97. Frank Armatis
3M Company
3M Center
Building 60-1N-01
St. Paul, MN 55144-1000

98. Everett B. Arnold
Detroit Diesel Corporation
Mechanical Systems Technology
13400 Outer Drive, West
Detroit, MI 48239-4001

99. Richard M. Arons
PA Consulting Group
279 Princeton Road
Hightstown, NJ 08550

100. Bertil Aronsson
Sandvik AB
S-12680
Stockholm Lerkrogsvagen 19
SWEDEN AIR MAIL

101. Dennis Assanis
University of Illinois
Department of Mechanical Engineering
1206 W. Green Street
Urbana, IL 61801

102. William H. Atwell
Dow Corning Corporation
3901 South Saginaw Road
MS:540
Midland, MI 48686-0995

103. V. S. Avva
North Carolina A&T State University
Department of Mechanical Engineering
Greensboro, NC 27411

104. Patrick Badgley
Adiabatics, Inc.
3385 Commerce Drive
Columbus, IN 47201

105. Sunggi Baik
Pohang Institute of Science & Technology
Department of Materials Science and Engineering
P.O. Box 125
Pohang 790-600
KOREA AIR MAIL

106. John M. Bailey
Caterpillar, Inc.
Technical Center
Building L
P.O. Box 1875
Peoria, IL 61656-1875

107. Bob Baker
Ceradyne, Inc.
3169 Redhill Avenue
Costa Mesa, CA 92626

108. Frank Baker
Aluminum Company of America
Alcoa Technical Center
Alcoa Center, PA 15069

109. J. G. Baldoni
GTE Laboratories Inc.
40 Sylvan Road
Waltham, MA 02254

110. Clifford P. Ballard
Allied-Signal, Inc.
Ceramics Program
P.O. Box 1021
Morristown, NJ 07962-1021

111. M. Balu
Amoco Performance Products Inc.
4500 McGinnis Ferry Road
Alpharetta, GA 30202

112. B. P. Bandyopadhyay
Toyohashi University of Technology
School of Production Systems Engineering
Tempaku-Cho Toyohashi 440
JAPAN AIR MAIL

113. P. M. Barnard
Ruston Gas Turbines Limited
Metallurgical Laboratory
P. O. Box 1
Lincoln LN2 5DJ
ENGLAND AIR MAIL

114. Harold N. Barr
Hittman Corporation
9190 Red Branch Road
Columbia, MD 21045

115. Renald D. Bartoe
Vesuvius McDanel
510 Ninth Avenue
Box 560
Beaver Falls, PA 15010-0560

116. Donald M. Bartos
Dow Corning Corporation
Advanced Ceramics Program
Midland, MI 48686-0995

117. David L. Baty
Babcock & Wilcox-LRC
P.O. Box 11165
Lynchburg, VA 24506-1165

118. Donald F. Baxter, Jr.
ASM International
Advanced Materials and
Processes
Materials Park, OH 44073-0002

119. M. Brad Beardsley
Caterpillar, Inc.
Advanced Materials Technology
Technical Center Bldg. E
P.O. Box 1875
Peoria, IL 61656-1875

120. Robert Beck
Teledyne CAE
Materials Engineering/Programs
1330 Laskey Road
P.O. Box 6971
Toledo, OH 43612

121. John C. Bell
Shell Research Limited
Thornton Research Centre
P.O. Box 1
Chester, Ch1 3SH
ENGLAND AIR MAIL

122. Albert H. Bell, III
General Motors Technical Center
30200 Mound Road
Engineering Building/W3 Turbine
Warren, MI 48090-9010

123. M. Bentele
Xamag, Inc.
259 Melville Avenue
Fairfield, CT 06430

124. Larry D. Bentsen
BF Goodrich Company
R&D Center
9921 Brecksville Road
Brecksville, OH 44141

125. Joseph C. Bentz
ENCERATEC
2525 Sandcrest Drive
Columbus, IN 47203

126. Louis Beregszazi
Defiance Precision Products
P.O. Drawer 428
Defiance, OH 43512

127. Tom Bernecki
Northwestern University
BIRL
1801 Maple Avenue
Evanston, IL 60201-3135

128. Charles F. Bersch
Institute for Defense Analyses
1801 North Beauregard Street
Alexandria, VA 22311

129. Ram Bhatt
NASA Lewis Research Center
21000 Brookpark Road
Cleveland, OH 44135

130. Deane I. Biehler
Caterpillar, Inc.
Engineering and Research
Materials
Technical Center, Building E
P.O. Box 1875
Peoria, IL 61656-1875

131. John. W. Bjerklie
Consolidated Natural Gas
Service Co., Inc.
Research Department
CNG Tower
Pittsburgh, PA 15222-3199

132. William D. Bjorndahl
TRW, Inc.
One Space Park
Building 01, Room 2040
Redondo Beach, CA 90278

133. Keith A. Blakely
Advanced Refractory
Technologies, Inc.
699 Hertel Avenue
Buffalo, NY 14207

134. Edward G. Blanchard
Netzsch Inc.
119 Pickering Way
Exton, PA 19341

135. Keith Blandford
Boride Products, Inc.
2879 Aero Park Drive
Traverse City, MI 49684

136. Bruce Boardman
Deere and Company Technical Center
3300 River Drive
Moline, IL 61265

137. Russell Bockstedt
Hoechst Celanese Corporation
150 JFK Parkway
Short Hills, NJ 07078

138. M. Boehmer
DLR German Aerospace Research Establishment
Postfach 90 60 58
D-5000 Koln 90
GERMANY AIR MAIL

139. Lawrence P. Boesch
EER Systems Corp.
1593 Spring Hill Road
Vienna, VA 22182-2239

140. Donald H. Boone
Boone & Associates
2412 Cascade Drive
Walnut Creek, CA 94598-4313

141. Tom Booth
Allied-Signal Aerospace Company
AiResearch Los Angeles Division
2525 West 190th Street
Torrance, CA 90509-2960

142. Tibor Bornemisza
Sundstrand Power Systems
4400 Ruffin Road
San Diego, CA 92186-5757

143. J.A.M. Boulet
University of Tennessee
Department of Engineering Science and Mechanics
310 Perkins Hall
Knoxville, TN 37996-2030

144. H. Kent Bowen
Massachusetts Institute of Technology
77 Massachusetts Avenue
Room E40-434
Cambridge, MA 02139

145. Leslie J. Bowen
Materials Systems
53 Hillcrest-Road
Concord, MA 01742

146. Steven C. Boyce
Air Force Office of Scientific Research
AFOSR/NA Bldg. 410
Bolling AFB DC 20332-6448

147. Gary L. Boyd
CEC
400 Howell Avenue, No. 4
Warland, WY 82401

148. Steve Bradley
UOP Research Center
50 East Algonquin Road
Des Plaines, IL 60017-6187

149. Michael C. Brands
Cummins Engine Company, Inc.
P.O. Box 3005
Mail Code 50179
Columbus, IN 47201

150. Raymond J. Bratton
Westinghouse Science and Technology Center
1310 Beulah Road
Pittsburgh, PA 15235

151. John J. Brennan
United Technologies Corporation
Research Center
Silver Lane, MS:24
East Hartford, CT 06108

152. Jeff D. Bright
Ceramatec, Inc.
2425 South 900 West
Salt Lake City, UT 84108

153. Terrence K. Brog
Coors Ceramics Company
Corporate Development and Technology
4545 McIntyre Street
Golden, CO 80403

154. Gunnar Broman
317 Fairlane Drive
Spartanburg, SC 29302

155. Al Brown
High-Tech Materials Alert
P.O. Box 882
Dayton, NJ 08810

156. Jesse Brown
Virginia Polytechnic Institute and State University
Center for Advanced Ceramic Materials
Blacksburg, VA 24061-0256

157. Sherman D. Brown
University of Illinois
Materials Science and Engineering Department
105 South Goodwin Avenue
204 Ceramics Building
Urbana, IL 61801

158. S. L. Bruner
Ceramatec, Inc.
2425 South 900 West
Salt Lake City, UT 84119

159. Adolfo Brusaferro
Keramont Corporation
4231 South Fremont Avenue
Tucson, AZ 85714

160. W. Bryzik
U.S. Army Tank Automotive Command
R&D Center
Propulsion Systems Division
Warren, MI 48397-5000

161. S. T. Buljan
GTE Laboratories, Inc.
40 Sylvan Road
Waltham, MA 02254

162. S. J. Burden
GTE Valenite
1711 Thunderbird
Troy, MI 48084

163. Curt V. Burkland
AMERCOM, Inc.
8928 Fullbright Avenue
Chatsworth, CA 91311

164. Bill Bustamante
AMERCOM, Inc.
8928 Fullbright Street
Chatsworth, CA 91311

165. Oral Buyukozturk
Massachusetts Institute of Technology
77 Massachusetts Avenue
Room 1-280
Cambridge, MA 02139

166. David A. Caillet
Ethyl Corporation
451 Florida Street
Baton Rouge, LA 70801

167. Frederick J. Calnan
Heany Industries, Inc.
249 Briarwood Lane
P.O. Box 38
Scottsville, NY 14546

168. Roger Cannon
Rutgers University
Ceramics Department
P.O. Box 909
Piscataway, NJ 08855-0909

169. Scott Cannon
P.O. Box 567254
Atlanta, GA 30356

170. Harry W. Carpenter
19945 Acre Street
Northridge, CA 91324

171. David Carruthers
Kyocera Industrial Ceramics Company
P.O. Box 2279
Vancouver, WA 98668-2279

172. Calvin H. Carter, Jr.
Cree Research, Inc.
2810 Meridian Parkway
Durham, NC 27713

173. J. David Casey
35 Atlantis Street
West Roxbury, MA 02132

174. Jere G. Castor
J. C. Enterprise
5078 North 83rd Street
Scottsdale, AZ 85250

175. James D. Cawley
Case Western Reserve University
Materials Science and
Engineering Department
Cleveland, OH 44106

176. Thomas C. Chadwick
Den-Mat Corporation
P.O. Box 1729
Santa Maria, CA 93456

177. Ronald H. Chand
Chand Kare Technical Ceramics
2 Coppage Drive
Worcester, MA 01603

178. Robert E. Chaney
EG&G Idaho, Inc.
Idaho National Engineering
Laboratory
P.O. Box 1625
Idaho Falls, ID 83415-3525

179. Frank C. Chang
U.S. Army Materials
Technology Laboratory
AMTL-EMM
405 Arsenal Street
Watertown, MA 02172

180. Robert M. Chapman
Allied-Signal Aerospace
Company
1530 Wilson Boulevard,
10th Floor
Arlington, VA 22209

181. William Chapman
Williams International
Corporation
2280 West Maple Road
Walled Lake, MI 48390-0200

182. Charlie Chen
LECO Corporation
P.O. Box 211688
Augusta, GA 30917

183. Albert A. Chesnes
U.S. Department of Energy
Transportation Technologies
CE-30, Forrestal Building,
6B-094
Washington, DC 20585

184. Kaiyin Chia
Carborundum Company
P.O. Box 832
Niagara Falls, NY 14302

185. Frank Childs
EG&G Idaho, Inc.
Idaho National Engineering
Laboratory
P.O. Box 1625
Idaho Falls, ID 83415-3527

186. William J. Chmura
Torrington Company
59 Field Street
Torrington, CT 06790-4942

187. Tsu-Wei Chou
University of Delaware
Center for Composite
Materials
201 Spencer Laboratory
Newark, DE 19716

188. R. J. Christopher
Ricardo Consulting Engineers
Bridge Works
Shoreham-By-Sea West Sussex
BN43 5FG
ENGLAND AIR MAIL

189. Joel P. Clark
Massachusetts Institute of
Technology
Room 8-409
Cambridge, MA 02139

190. Giorgio Clarotti
Commission of the European Communities
DGXII-C3, M075, 1-53;
200 Rue de la Loi
B-1049 Brussels
BELGIUM AIR MAIL

191. W. J. Clegg
ICI Advanced Materials
P.O. Box 11
The Heath, Runcorn Cheshire
WA7 4QE
ENGLAND AIR MAIL

192. Joseph Cleveland
GTE Products Corporation
Hawes Street
Towanda, PA 18848-0504

193. Gloria M. Collins
ASTM
1916 Race Street
Philadelphia, PA 19103

194. William C. Connors
Sundstrand Aviation Operations
Materials Science and Engineering Department
4747 Harrison Avenue
P.O. Box 7002
Rockford, IL 61125-7002

195. John A. Coppola
Carborundum Company
P.O. Box 156
Niagara Falls, NY 14302

196. Normand D. Corbin
Norton Company
Advanced Ceramics
Goddard Road
Northboro, MA 01532-1545

197. Douglas Corey
Allied-Signal Aerospace Company
2525 West 190th Street
MS:T52
Torrance, CA 90504-6099

198. Keith P. Costello
Chand/Kare Technical Ceramics
2 Coppage Drive
Worcester, MA 01603-1252

199. Ed L. Courtright
Pacific Northwest Laboratory
MS:K3-59
Richland, WA 99352

200. Anna Cox
Mitchell Market Reports
P.O. Box 23
Monmouth Gwent NP5 4YG
UNITED KINGDOM AIR MAIL

201. Thomas Coyle
Unocal Corporation
Unocal Science & Technology Division
376 South Valencia Avenue
Brea, CA 92621

202. Art Cozens
Instron Corporation
3414 Snowden Avenue
Long Beach, CA 90808

203. Robert C. Craft
American Ceramic Society, Inc.
757 Brooksedge Plaza Drive
Westerville, OH 43081

204. Mark Crawford
New Technology Week
4604 Monterey Drive
Annandale, VA 22003

205. Richard A. Cree
Markets & Products, Inc.
P.O. Box 14328
Columbus, OH 43214-0328

206. Les Crittenden
Vesuvius McDanel
Box 560
Beaver Falls, PA 15010

207. William J. Croft
U.S. Army Materials
Technology Laboratory
405 Arsenal Street
Watertown, MA 02172

208. M. J. Cronin
Mechanical Technology, Inc.
968 Albany-Shaker Road
Latham, NY 12110

209. Gary M. Crosbie
Ford Motor Company
1430 Culver Avenue
S-2079, SRL Building
Dearborn, MI 48121-4036

210. Floyd W. Crouse, Jr.
U.S. Department of Energy
Morgantown Energy
Technology Center
Collins Ferry Road
P.O. Box 880
Morgantown, WV 26505

211. John Cuccio
Allied-Signal Aerospace
Company
Garrett Auxiliary Power
Division
P.O. Box 5227, MS:1302-2Q
Phoenix, AZ 85010

212. Raymond Cutler
Ceramatec, Inc.
2425 South 900 West
Salt Lake City, UT 84119

213. Charles D'Angelo
GTE Laboratories, Inc.
40 Sylvan Road
Waltham, MA 02154

214. Stephen C. Danforth
Rutgers University
Ceramic Engineering Department
P.O. Box 909
Piscataway, NJ 08855-0909

215. Sankar Das Gupta
Electrofuel Manufacturing
Co., Ltd.
9 Hanna Avenue
Toronto Ontario MGK-1W8
CANADA AIR MAIL

216. Charles Davis
Sverdrup Technology,
Inc., MSFC
620 Discovery Drive
Huntsville, AL 35806

217. Frank Davis
Allied Signal Aerospace Co.
7550 Lucerne Dr., # 203
Middleburg Heights, OH 44130

218. Robert F. Davis
North Carolina State
University
Materials Engineering
Department
229 Riddick Laboratory
P.O. Box 7907
Raleigh, NC 27695

219. Thomas DeAngelis
Carborundum Company
Niagara Falls R&D Center
P.O. Box 832
Niagara Falls, NY 14302

220. George DeBell
Ford Motor Company
Material Systems Reliability
Department
20000 Rotunda Drive
P.O. Box 2053, Room S-2023
Dearborn, MI 48121-2053

221. Michael DeLuca
AMP-AKZO
West Lane
Aquebogue, NY 11931

222. Gerald L. DePoorter
Colorado School of Mines
Metallurgical and Materials
Engineering Department
Golden, CO 80401

223. J. F. DeRidder
Omni Electro Motive, Inc.,
12 Seely Hill Road
Newfield, NY 14867

224. Nick C. Dellow
Materials Technology
Publications
40 Sotheron Road
Watford Herts WD1 2QA
UNITED KINGDOM AIR MAIL

225. L. R. Dharani
University of Missouri-Rolla
224 M.E.
Rolla, MO 65401

226. Douglas A. Dickerson
Union Carbide Specialty
Powders
1555 Main Street
Indianapolis, IN 46224

227. John Dodsworth
Vesuvius Research &
Development
Technical Ceramics Group
Box 560
Beaver Falls, PA 15010

228. B. Dogan
Institut fur Werkstofforschung
GKSS-Forschungszentrum
Geesthacht GmbH
Max-Planck-Strasse
D-2054 Geesthacht
GERMANY AIR MAIL

229. Jean-Marie Drapier
FN Moteurs S.A.
Material and Processing
B-4041 Milmort (Herstal)
BELGIUM AIR MAIL

230. Kenneth C. Dreitlein
United Technologies
Research Center
Silver Lane
East Hartford, CT 06108

231. Robin A.L. Drew
McGill University
Department of Mining and
Metallurgical Engineering
3450 University Street
Montreal Quebec H3A 2A7
CANADA AIR MAIL

232. Winston H. Duckworth
BCL
Columbus Division
505 King Avenue
Columbus, OH 43201-2693

233. Edmund M. Dunn
Texel Company
6 Third Street
Lexington, MA 02173

234. Bill Durako
Sundstrand Aviation Operations
Department 789-6
4747 Harrison Avenue
P.O. Box 7002
Rockford, IL 61125-7002

235. Ernest J. Duwell
212 Elm Street
Hudson, WI 54016

236. Chuck J. Dziedzic
Coors Ceramics Company
Structural Products Group
17750 West 32nd Avenue
Golden, CO 80401

237. Robert J. Eagan
Sandia National Laboratories
Engineered Materials &
Processes Center
Org 1700
P.O. Box 5800
Albuquerque, NM 87185-5800

238. Jeffrey Eagleson
Lanxide Corporation
1001 Connecticut Avenue, N.W.
Washington, DC 20036

239. Harry E. Eaton
United Technologies Corporation
Research Center
Silver Lane
East Hartford, CT 06108

240. Harvill C. Eaton
Louisiana State
University
Office of Research
and Economic Development
240 Thomas Boyd Hall
Baton Rouge, LA 70803

241. Christopher A. Ebel
Carborundum Company
Technology Division
P.O. Box 337
Niagara Falls, NY 14302

242. J. J. Eberhardt
U.S. Department of Energy
Office of Transportation
Materials
CE-34, Forrestal Building
Washington, DC 20585

243. Jim Edler
Eaton Corporation
26201 Northwestern
Highway
P.O. Box 766
Southfield, MI 48037

244. William A. Ellingson
Argonne National Laboratory
Materials Science & Technology
Division
9700 South Cass Avenue
Argonne, IL 60439

245. William S. Ellis
Machined Ceramics
629 N. Graham St.
N. Industrial Park
Bowling Green, KY 42101

246. Glen B. Engle
Nuclear & Aerospace Materials
Corporation
16716 Martincoit Road
Poway, CA 92064

247. Jeff Epstein
Ceramic Technologies, Inc.
2107 Jamara Lane
Houston, TX 77077

248. Kenneth A. Epstein
Dow Chemical U.S.A.
Ceramics and Advanced
Materials
800 Building
Midland, MI 48667

249. Art Erdemir
Argonne National Laboratory
Materials and Components
Technology Division
9700 South Cass Avenue
Argonne, IL 60439

250. E. M. Erwin
Lubrizol Corporation
1819 East 225th Street
Euclid, OH 44117

251. Kenji Esaki
Toyota Technical Center
U.S.A., Inc.
2000 Town Center, Suite 500
Southfield, MI 48075

252. Jose L. Escalante
Anglo-Mex-Tech. Inc.
3923 N.W. 24th Street
Miami, FL 33142

253. John N. Eustis
U.S. Department of Energy
Industrial Energy Efficiency
Division
CE-221, Forrestal Building
Washington, DC 20585

254. Robert C. Evans
NASA Lewis Research Center
Terrestrial Propulsion Office
21000 Brookpark Road, MS:86-6
Cleveland, OH 44135

255. W. L. Everitt
Kyocera International, Inc.
8611 Balboa Avenue
San Diego, CA 92123

256. Gordon Q. Evison
332 South Michigan Avenue
Suite 1730
Chicago, IL 60604

257. John W. Fairbanks
U.S. Department of Energy
Advanced Propulsion Division
CE-322, Forrestal Building
Washington, DC 20585

258. Tim Fawcett
Dow Chemical Company
Central Research, Advanced Ceramics Laboratory
1776 Building
Midland, MI 48674

259. Robert W. Fawley
Sundstrand Power Systems
Division of Sundstrand Corporation
4400 Ruffin Road
P.O. Box 85757
San Diego, CA 92186-5757

260. John J. Fedorchak
GTE Products Corporation
Hawes Street
Towanda, PA 18848-0504

261. Jeff T. Fenton
Vista Chemical Company
900 Threadneedle
Houston, TX 77079

262. Larry Ferrell
Babcock & Wilcox
Old Forest Road
Lynchburg, VA 24505

263. Raymond R. Fessler
BIRL
Industrial Research Lab
1801 Maple Avenue
Evanston, IL 60201

264. Michelle Finch
E. I. DuPont de Nemours & Company, Inc.
Experimental Station
Information Center E302/301
Wilmington, DE 19898

265. Arthur D. Fine
United Technologies Corporation
Pratt & Whitney Aircraft
400 Main Street
MS:163-10
East Hartford, CT 06108

266. Ross F. Firestone
Ross Firestone Company
188 Mary Street
Winnetka, IL 60093-1520

267. Sharon L. Fletcher
Arthur D. Little, Inc.
15 Acorn Park
Cambridge, MA 02140-2390

268. Thomas F. Foltz
Textron Specialty Materials
2 Industrial Avenue
Lowell, MA 01851

269. Renee G. Ford
Materials and Processing Report
P.O. Box 72
Harrison, NY 10528

270. John Formica
Supermaterials
2020 Lakeside Avenue
Cleveland, OH 44114

271. Jennifer M. Fox
Dyson Refractories Limited
R&D Laboratory
Owler Bar
Sheffield S17 3BJ
UNITED KINGDOM AIR MAIL

272. Edwin Frame
Southwest Research Institute
Division 2
P.O. Drawer 28510
San Antonio, TX 78284

273. Armanet Francois
French Scientific Mission
4101 Reservoir Road, N.W.
Washington DC 20007-2176

274. R. G. Frank
Technology Assessment Group
10793 Bentley Pass Lane
Loveland, OH 45140

275. David J. Franus
Forecast International
22 Commerce Road
Newtown, CT 06470

276. Marc R. Freedman
NASA Lewis Research Center
21000 Brookpark Road
MS:49-3
Cleveland, OH 44135

277. Douglas Freitag
LTV Missiles Division
P.O. Box 650003
MS:WT-21
Dallas, TX 75265

278. Brian R.T. Frost
Argonne National Laboratory
9700 South Cass Avenue
Building 900
Argonne, IL 60439

279. Lawrence R. Frost
Instron Corporation
100 Royall Street
Canton, MA 02021

280. George A. Fryburg
Norton/TRW Ceramics
7A-4 Raymond Avenue
Salem, NH 03079

281. Xiren Fu
Shanghai Institute of Ceramics
Chinese Academy of Sciences
1295 Ding-xi Road
Shanghai 200050
CHINA AIR MAIL

282. John Gahimer
P.O. Box 1302
Dublin, OH 43017

283. J. P. Gallagher
University of Dayton Research Institute
300 College Park, JPC-250
Dayton, OH 45469-0120

284. Tom Garritano
University of Tennessee
Science Alliance
101 South College
Knoxville, TN 37996-1328

285. Joy A. Garwood
Norton Company
Advanced Ceramics
Goddard Road
Northboro, MA 01532-1545

286. H. Maury Gatewood
Reynolds Metals Company
Corporate R&D
Fourth and Canal Streets
P.O. Box 27003
Richmond, VA 23261

287. L. J. Gauckler
ETH-Zurich
Sonneggstrasse 5
CH-8092 Zurich 8092
SWITZERLAND AIR MAIL

288. Peter A. Gaydos
Battelle Columbus Laboratories
505 King Avenue
Columbus, OH 43201

289. George E. Gazza
U.S. Army Materials Technology Laboratory
Ceramics Research Division
405 Arsenal Street
Watertown, MA 02172-0001

290. D. Gerster
CEA-DCOM
33 Rue De La Federation
Paris 75015
FRANCE AIR MAIL

291. John Ghinazzi
Coors Technical Ceramics Company
1100 Commerce Park Drive
Oak Ridge, TN 37830

292. Robert Giddings
General Electric Company
Research Laboratory
P.O. Box 8
Schenectady, NY 12301

293. A. M. Glaeser
University of California
Materials Science and Mineral Engineering
Lawrence Berkeley Laboratory
Hearst Mining Building
Berkeley, CA 94720

294. Paul Glance
Concept Analysis
R&D
950 Stephenson Highway
Dupont Automotive Development Building
Troy, MI 48007-7013

295. Joseph W. Glatz
Naval Air Propulsion Center
Systems Engineering Division
P.O. Box 7176, PE24
Trenton, NJ 08628

296. W. M. Goldberger
Superior Graphite Company
R&D
2175 East Broad Street
Columbus, OH 43209

297. Allan E. Goldman
U.S. Graphite, Inc.
907 West Outer Drive
Oak Ridge, TN 37830

298. Stephen T. Gonczy
Allied Signal Research
P.O. Box 5016
Des Plaines, IL 60017

299. Jeffrey M. Gonzales
GTE Products Corporation
Hawes Street
Towanda, PA 18848-0504

300. Robert J. Gottschall
U.S. Department of Energy
ER-131, MS:G-236
Washington, DC 20545

301. Earl Graham
Cleveland State University
Department of Chemical Engineering
Euclid Avenue at East 24th Street
Cleveland, OH 44115

302. William A. Graham
Lanxide Corporation
P.O. Box 6077
Newark, DE 19714-6077

303. Robert E. Green, Jr.
Johns Hopkins University
Materials Science and Engineering Department
Baltimore, MD 21218

304. Lance Groseclose
General Motors Corporation
Allison Gas Turbine Division
P.O. Box 420, MS:W-5
Indianapolis, IN 46206

305. Mark F. Gruninger
Union Carbide Corporation
Specialty Powder Business
1555 Main Street
Indianapolis, IN 46224

306. Ernst Gugel
Cremer Forschungsinstitut GmbH&Co.KG
Oeslauer Strasse 35
D-8633 Roedental 8633
GERMANY AIR MAIL

307. Donald L. Guile
Corning Glass Works
SP-DV-1-9
Corning, NY 14831

308. Bimleshwar P. Gupta
Solar Energy Research Institute
Mechanical and Industrial Technology Division
1617 Cole Boulevard
Golden, CO 80401

309. John P. Gyekenyesi
NASA Lewis Research Center
21000 Brookpark Road, MS:6-1
Cleveland, OH 44135

310. Nabil S. Hakim
Detroit Diesel Corporation
13400 West Outer Drive
Detroit, MI 48239

311. Philip J. Haley
General Motors Corporation
Vehicular Engineering
P.O. Box 420, MS:T12A
Indianapolis, IN 46236

312. Judith Hall
Fiber Materials, Inc.
Biddeford Industrial Park
5 Morin Street
Biddeford, ME 04005

313. Y. Harada
IIT Research Institute
Nometallic Materials and Composites
10 West 35th Street
Chicago, IL 60616

314. R. A. Harmon
25 Schalren Drive
Latham, NY 12110

315. Amy Harmon-Barrett
Martin Marietta Laboratories
1450 South Rolling Road
Baltimore, MD 21227

316. Norman H. Harris
Hughes Aircraft Company
P.O. Box 800520
Saugus, CA 91380-0520

317. Alan Hart
Dow Chemical Company
Advanced Ceramics Laboratory
1776 Building
Midland, MI 48674

318. Pat E. Hart
Battelle Pacific Northwest Laboratories
Ceramics and Polymers Development Section
P.O. Box 999
Richland, WA 99352

319. Stephen D. Hartline
Norton Company
Advanced Ceramics
Goddard Road
Northboro, MA 01532-1545

320. Michael H. Haselkorn
Caterpillar, Inc.
Engineering Research Materials
Technical Center, Building E
P.O. Box 1875
Peoria, IL 61656-1875

321. N. B. Havewala
Corning, Inc.
SP-PR-11
Corning, NY 14831

322. John Haygarth
Teledyne WAA Chang Albany
P.O. Box 460
Albany, OR 97321

323. Norman L. Hecht
University of Dayton Research Institute
300 College Park
Dayton, OH 45469-0172

324. Peter W. Heitman
General Motors Corporation
Allison Gas Turbine Division
P.O. Box 420, MS:W-5
Indianapolis, IN 46206-0420

325. Robert W. Hendricks
Virginia Polytechnic Institute and State University
Materials Engineering Department
210 Holden Hall
Blacksburg, VA 24061-0237

326. Wynne Henley
Hertel Cutting Technologies, Inc.
1000 Clearview Court
Oak Ridge, TN 37830

327. Thomas L. Henson
GTE Products Corporation
Chemical & Metallurgical Division
Hawes Street
Towanda, PA 18848

328. Thomas P. Herbell
NASA Lewis Research Center
21000 Brookpark Road
MS:49-3
Cleveland, OH 44135

329. Marlene Heroux
Rolls-Royce, Inc.
2849 Paces Ferry Road
Suite 450
Atlanta, GA 30339-3769

330. Robert L. Hershey
Science Management Corporation
1255 New Hampshire Ave., N.W.
Suite 1033
Washington, DC 20036

331. Hendrik Heystek
Bureau of Mines
Tuscaloosa Research Center
P.O. Box L
University, AL 35486

332. Wallace C. Higgins
Norwal Unlimited
P.O. Box 1258
Alfred, NY 14802

333. Robert V. Hillery
GE Aircraft Engines
One Neumann Way, M.D. H85
Cincinnati, OH 45215

334. Arthur Hindman
Instron Corporation
100 Royall Street
Canton, MA 02021

335. Jon Hines
American Ceramic Society, Inc.
757 Brooksedge Plaza Drive
Westerville, OH 43081-6136

336. Hans Erich Hintermann
CSEM
Materials and Micromechanics Division
Rue Breguet-2
Neuchatel 2000
SWITZERLAND AIR MAIL

337. Shinichi Hirano
Mazda R&D of North America, Inc.
1203 Woodridge Avenue
Ann Arbor, MI 48105

338. Tommy Hiraoka
NGK Locke, Inc.
1000 Town Center
Southfield, MI 48075

339. John M. Hobday
U.S. Department of Energy
Morgantown Energy Technology Center
Collins Ferry Road
P.O. Box 880
Morgantown, WV 26507

340. Greg Hoenes
Vista Chemical Company
900 Threadneedle
P.O. Box 19029
Houston, TX 77079-2990

341. Clarence Hoenig
Lawrence Livermore National Laboratory
P.O. Box 808, Mail Code L-369
Livermore, CA 94550

342. Thomas Hollstein
Fraunhofer-Institut fur Werkstoffmechanik IWM
Wohlerstrabe 11
D-7800 Freiburg
GERMANY AIR MAIL

343. Richard Holt
National Research Council
of Canada
Structures and Materials
Laboratory
Ottawa Ontario K1A 0R6
CANADA AIR MAIL

344. Joseph Homeny
University of Illinois
Department of Materials Science
and Engineering
105 South Goodwin Avenue
Ceramics Building
Urbana, IL 61801

345. A. T. Hopper
Battelle Columbus
Laboratories
Metals and Ceramics Department
505 King Avenue
Columbus, OH 43201-2693

346. Michael Horgan
Materials Engineering Magazine
1100 Superior Avenue
Cleveland, OH 44114

347. Woodie Howe
Coors Technical Ceramics
Company
1100 Commerce Park Drive
Oak Ridge, TN 37830

348. Stephen M. Hsu
National Institute of
Standards and Technology
Gaithersburg, MD 20899

349. Hann S. Huang
Argonne National Laboratory
9700 South Cass Avenue
Argonne, IL 60439-4815

350. Gene Huber
Precision Ferrites & Ceramics
5576 Corporate Drive
Cypress, CA 90630

351. M. L. Huckabee
GTE Laboratories, Inc.
40 Sylvan Road
Waltham, MA 02254

352. Harold A. Huckins
Princeton Advanced
Technology, Inc.
56 Finley Road
Princeton, NJ 08540

353. Fred R. Huettic
Advanced Magnetics, Inc.
45 Corey Lane
Mendham, NJ-07945

354. Bill Huffman
Zircar
110 North Main Street
Florida, NY 10921

355. Brian K. Humphrey
Lubrizol Petroleum
Chemicals Co.
3000 Town Center, Suite 1340
Southfield, MI 48075-1201

356. Robert M. Humrick
Dylon Ceramic Technologies
3100 Edgehill Road
Cleveland Heights, OH 44118

357. Lorretta Inglehart
National Science Foundation
Division of Materials Research
1800 "G" Street, N.W.,
Room 408
Washington, DC 20550

358. Michael S. Inoue
Kyocera International, Inc.
KII Library
8611 Balboa Avenue
San Diego, CA 92123-1580

359. Osama Jadaan
University of Wisconsin-
Platteville
General Engineering Division
1 University Plaza
Platteville, WI 53818

360. Curtis A. Johnson
General Electric Company
Corporate R&D
Room MB-187
P.O. Box 8
Schenectady, NY 12301

361. Sylvia Johnson
SRI International
333 Ravenswood Avenue
Menlo Park, CA 94025

362. Thomas A. Johnson
Lanxide Corporation
1300 Marrows Road
P.O. Box 6077
Newark, DE 19714-6077

363. W. S. Johnson
Indiana University
One City Centre, Suite 200
Bloomington, IN 47405

364. Jill E. Jonkouski
U.S. Department of Energy
9800 South Cass Avenue
Argonne, IL 60439-4899

365. L. A. Joo
Great Lakes Research
Corporation
P.O. Box 1031
Elizabethton, TN 37643

366. A. D. Joseph
SPX Corporation
700 Terrace Point
Muskegon, MI 49443

367. Adam Jostsons
Australian Nuclear Science &
Technology Organization
Lucas Heights Research
Laboratories
New Illawarra Road
Lucas Heights New South Wales
AUSTRALIA AIR MAIL

368. Matthew K. Juneau
Ethyl Corporation
451 Florida Street
Baton Rouge, LA 70801

369. Hartmut Kainer
Didier-Werke AG
Anlagentechnik Wiesbaden
Abraham-Lincoln-Str. 16
D-62 Wiesbaden
GERMANY AIR MAIL

370. Tom Kalamasz
Norton/TRW Ceramics
7A-4 Raymond Avenue
Salem, NH 03079

371. Lyle R. Kallenbach
Phillips Petroleum Company
R&D
Mail Drop:123AL
Bartlesville, OK 74004

372. Nick Kamiya
Kyocera Industrial Ceramics
Corporation
2700 River Road
Des Plaines, IL 60018

373. Roy Kamo
Adiabatics, Inc.
3385 Commerce Park Drive
Columbus, IN 47201

374. S. Kang
GTE Laboratories, Inc.
40 Sylvan Road
Waltham, MA 02254

375. Chih-Chun Kao
Industrial Technology Research
Institute
Materials Research
Laboratories
195 Chung-Hsing Road, Sec. 4
Chutung Hsinchu 31015 R.O.C.
TAIWAN AIR MAIL

376. Keith R. Karasek
Allied-Signal, Inc.
Engineered Materials Research
Center
50 East Algonquin Road
P.O. Box 5016
Des Plaines, IL 60017-5016

377. Robert E. Kassel
Ceradyne, Inc.
3169 Redhill Avenue
Costa Mesa, CA 92626

378. Allan Katz
Wright Laboratory
Metals and Ceramics Division
WL/MLLM
Wright-Patterson AFB, OH 45433

379. R. Nathan Katz
Worcester Polytechnic Institute
Dept. of Mechanical Engineering
100 Institute Road
Worcester, MA 01609

380. Ted Kawaguchi
Tokai Carbon America, Inc.
375 Park Avenue, Suite 3802
New York, NY 10152

381. Noritsugu Kawashima
TOSHIBA Corporation
Mechanical Engineering Laboratory
4-1 Ukishima-Cho
Kawasaki-Ku Kawasaki 210
JAPAN AIR MAIL

382. Lisa Kempfer
Penton Publishing
Materials Engineering
1100 Superior Avenue
Cleveland, OH 44114-2543

383. Frederick L. Kennard, III
General Motors Corporation
AC Rochester
Department 32-24, EB
1300 North Dort Highway
Flint, MI 48556

384. David O. Kennedy
Lester B. Knight Cast Metals Inc.
549 West Randolph Street
Chicago, IL 60661

385. George Keros
Photon Physics
3175 Penobscot Building
Detroit, MI 48226

386. Pramod K. Khandelwal
General Motors Corporation
Allison Gas Turbine Division
P.O. Box 420, MS:W05
Indianapolis, IN 46206

387. Jim R. Kidwell
Allied-Signal Aerospace Company
Garrett Auxiliary Power Division
P.O. Box 5227
Phoenix, AZ 85010

388. Han J. Kim
GTE Laboratories, Inc.
40 Sylvan Road
Waltham, MA 02254

389. Shin Kim
Korea Institute of Machinery & Metals
66 Sangnam-dong, Changwon
Kyungnam 641-010
KOREA AIR MAIL

390. W. C. King
Mack Truck, Z-41
1999 Pennsylvania Avenue
Hagerstown, MD 21740

391. Carol Kirkpatrick
MSE, Inc.
CDIF Technical Library
P.O. Box 3767
Butte, MT 59702

392. Tony Kirn
Caterpillar, Inc.
Defense Products Department, JB7
Peoria, IL 61629

393. James D. Kiser
NASA Lewis Research Center
21000 Brookpark Road, MS:49-3
Cleveland, OH 44135

394. Max Klein
Gas Research Institute
Thermodynamics
8600 West Bryn Mawr Avenue
Chicago, IL 60631

395. Richard N. Kleiner
Coors Ceramics Company
4545 McIntyre Street
Golden, CO 80403

396. Stanley J. Klima
NASA Lewis Research Center
21000 Brookpark Road
MS:6-1
Cleveland, OH 44135

397. Chris E. Knapp
Norton Advanced Ceramics
of Canada Ltd.
8001 Daly Street
Niagara Falls, Ontario L2G 6S2
CANADA AIR MAIL

398. Albert S. Kobayashi
University of Washington
Mechanical Engineering
Department
MS:FU10
Seattle, WA 98195

399. Shigeki Kobayashi
Toyota Central Research
Labs, Inc.
Nagakute Aichi 480-11
JAPAN AIR MAIL

400. Richard A. Kole
Z-Tech Corporation
8 Dow Road
Bow, NH 03304

401. E. Kostiner
University of Connecticut
Chemistry Department, U-60
Storrs, CT 06269-3060

402. Kenneth A. Kovaly
Technical Insights, Inc.
P.O. Box 1304
Fort Lee, NJ 07024-9967

403. Ralph G. Kraft
Spraying Systems Company
North Avenue at Schmale Road
Wheaton, IL 60189-7900

404. Saunders B. Kramer
U.S. Department of Energy
Advanced Propulsion Division
CE-322, Forrestal Building
Washington, DC 20585

405. Arthur Kranish
Trends Publishing, Inc.
1079 National Press Building
Washington, DC 20045

406. A. S. Krieger
Radiation Science, Inc.
P.O. Box 293
Belmont, MA 02178

407. Pieter Krijgsman
Ceramic Design International
Holding B.V.
P.O. Box 68
Hattem 8050-AB
THE NETHERLANDS AIR MAIL

408. Waltraud M. Kriven
University of Illinois
Materials Science and
Engineering Department
105 South Goodwin Avenue
Urbana, IL 61801

409. Edward J. Kubel, Jr.
ASM International Advanced
Materials & Processes
Materials Park, OH 44073

410. Dave Kupperman
Argonne National Laboratory
9700 South Cass Avenue
Argonne, IL 60439

411. Oh-Hun Kwon
Norton Company
Advanced Ceramics
Goddard Road
Northboro, MA 01532-1545

412. W. J. Lackey
Georgia Institute of Technology
Materials Science and
Technology
Atlanta, GA 30332

413. Jai Lala
Tenmat Ltd.
40 Somers Road
Rugby Warwickshire CV22 7DH
ENGLAND AIR MAIL

414. Hari S. Lamba
General Motors Corporation
Electro-Motive Division
9301 West 55th Street
LaGrange, IL 60525

415. Richard L. Landingham
Lawrence Livermore National Laboratory
Ceramics, Corrosion, and Thermochemistry
P.O. Box 808, L-369
Livermore, CA 94550

416. Charles J. Landry
Chand Kare Technical Ceramics
712 Flat Hill Road
Lumenburg, MA 01462

417. Manfred W. Langer
Volkswagen AG
Material Technology
3180 Wolfsburg 1
GERMANY AIR MAIL

418. James Lankford
Southwest Research Institute
Department of Materials Sciences
6220 Culebra Road
San Antonio, TX 78228-0510

419. Stanley B. Lasday
Business News Publishing Co.
Manor Oak One
1910 Cochran Road, Suite 630
Pittsburgh, PA 15220

420. Mark S. Laser
Solar Turbines, Inc.
2211 Erie Street
San Diego, CA 92110

421. S. K. Lau
Carborundum Company
Technology Division
P.O. Box 832, B-100
Niagara Falls, NY 14302

422. Edward A. Lauder
Advanced Composite Materials Corporation
1525 South Buncombe Road
Greer, SC 29651-9208

423. J. Lawrence Lauderdale
Babcock & Wilcox
Contract Research Division
1850 "K" Street, Suite 950
Washington, DC 20006

424. Harry A. Lawler
Carborundum Company
Technology Division
P.O. Box 832
Niagara Falls, NY 14302

425. Jean F. LeCostaouec
Textron Speciality Materials
2 Industrial Avenue
Lowell, MA 01851

426. Benson P. Lee
Interscience, Inc.
9718 Lake Shore Boulevard
Cleveland, OH 44108

427. Burtrand I. Lee
Clemson University
Department of Ceramic Engineering
Olin Hall
Clemson, SC 29634-0907

428. June-Gunn Lee
KIST
Structural Ceramic Lab
P.O. Box 131, Cheong-Ryang
Seoul 130-650
KOREA AIR MAIL

429. Ran-Rong Lee
Ceramics Process Systems Corporation
155 Fortune Boulevard
Milford, MA 01757

430. Stan Levine
NASA Lewis Research Center
21000 Brookpark Road
MS:49-3
Cleveland, OH 44135

431. Alan V. Levy
Lawrence Berkeley Laboratory
One Cyclotron Road, MS:62-203
Berkeley, CA 94720

432. Ai-Kang Li
Materials Research
Laboratories, ITRI
195-5 Chung-Hsing Road, Sec. 4
Chutung Hsinchu 31015 R.O.C.
TAIWAN AIR MAIL

433. Winston W. Liang
Hong Kong Industrial
Technology Centre Co. Ltd.
78 Tat Chee Avenue
4/F, HKPC Building
Howloon
HONG KONG AIR MAIL

434. Robert Licht
Norton Company
Advanced Ceramics
Goddard Road
Northboro, MA 01532-1545

435. E. Lilley
Norton Company
Advanced Ceramics
Goddard Road
Northboro, MA 01532-1545

436. Laura J. Lindberg
Allied-Signal Aerospace
Company
Garrett Fluid Systems Division
1300 West Warner
MS: 93-901-1207-4TT
P.O. Box 22200
Tempe, AZ 85284-2200

437. Leonard C. Lindgren
General Motors Corporation
Allison Gas Turbine Division
P.O. Box 420, Speed Code:T-20A
Indianapolis, IN 46206-0420

438. Hans A. Lindner
Cremer Forschungsinstitut
GmbH&Co.KG
Oeslauer Strasse 35
D-8633 Rodental 8866
GERMANY AIR MAIL

439. Ronald E. Loehman
Sandia National Laboratories
Chemistry & Ceramics
Department 1840
P.O. Box 5800
Albuquerque, NM 87185

440. Jeffrey C. Logas
Winona State University
Composite Materials
Engineering
115 Pasteur Hall
Winona, MN 55987

441. Bill Long
Babcock & Wilcox
P.O. Box 11165
Lynchburg, VA 24506

442. William D. Long
Wacker Chemicals (USA), Inc.
ESK Engineered Ceramics
50 Locust Avenue
New Canaan, CT 06840

443. L. A. Lott
EG&G Idaho, Inc.
Idaho National Engineering
Laboratory
P.O. Box 1625
Idaho Falls, ID 83415-2209

444. Raouf O. Loutfy
MER Corporation
7960 South Kolb Road
Tucson, AZ 85706

445. Gordon R. Love
Aluminum Company of America
Alcoa Technical Center
Alcoa Center, PA 15069

446. Lydia Luckevich
Ortech International
2395 Speakman Drive
Mississauga Ontario L5K 1B3
CANADA AIR MAIL

447. James W. MacBeth
Carborundum Company
Structural Ceramics Division
P.O. Box 1054
Niagara Falls, NY 14302

448. H. MacLaren
General Electric Company
Thomson Laboratory, Materials Engineering 36807
1000 Western Avenue
Lynn, MA 01910

449. George Maczura
Aluminum Company of America
Industrial Chemicals Division
670 One Allegheny Square
Pittsburgh, PA 15212

450. David Maginnis
Tinker AFB
OC-ALC/LIIRE
Tinker AFB OK 73145-5989

451. Frank Maginnis
Aspen Research, Inc.
220 Industrial Boulevard
Moore, OK 73160

452. Tai-il Mah
Universal Energy Systems, Inc.
Ceramics and Composites Research
4401 Dayton-Xenia Road
Dayton, OH 45432

453. Kenneth M. Maillar
Barbour Stockwell Company
83 Linskey Way
Cambridge, MA 02142

454. Lorenzo Majno
Instron Corporation
100 Royall Street
Canton, MA 02021

455. S. G. Malghan
National Institute of Standards and Technology
I-270 & Clopper Road
Gaithersburg, MD 20899

456. Lars Malmrup
United Turbine AB
Box 13027
Malmo S-200 44
SWEDEN AIR MAIL

457. John Mangels
Ceradyne, Inc.
3169 Redhill Avenue
Costa Mesa, CA 92626

458. Russell V. Mann
Matec Applied Sciences, Inc.
75 South Street
Hopkinton, MA 01748

459. William R. Manning
Champion Aviation Products Division
Old Norris Road
P.O. Box 686
Liberty, SC 29657

460. Ken Marnoch
Amercom, Inc.
8928 Fullbright Avenue
Chatsworth, CA 91311

461. Robert A. Marra
Aluminum Company of America
Alcoa Technical Center
Advanced Ceramics Center - E
Alcoa Center, PA 15069

462. Chauncey L. Martin
3M Company
3M Center, Building 60-1N-01
St. Paul, MN 55144

463. Steven C. Martin
Advanced Refractory Technologies, Inc.
699 Hertel Avenue
Buffalo, NY 14207

464. Kelly J. Mather
Williams International Corporation
2280 West Maple Road
P.O. Box 200
Walled Lake, MI 48088

465. James P. Mathers
3M Company
3M Center
Building 201-3N-06
St. Paul, MN 55144

466. Marshall Mayer
Instron Corporation
3815 Presidential Parkway,
Suite 100
Atlanta, GA 30340

467. Ron Mayville
Arthur D. Little, Inc.
15-163 Acorn Park
Cambridge, MA 02140

468. F. N. Mazadarany
General Electric Company
Research Laboratory
Building K-1, Room MB-159
P.O. Box 8
Schenectady, NY 12301

469. James W. McCauley
Alfred University
NYS College of Ceramics
Binns-Merrill Hall
Alfred, NY 14802

470. Carolyn McCormick
Allied-Signal Aerospace
Company
Garrett Auxiliary Power
Division
Bldg. 1303-206
P.O. Box 5227, MS:9317-2
Phoenix, AZ 85010

471. Louis R. McCreight
2763 San Ramon Drive
Rancho Palos Verdes, CA 90274

472. Colin F. McDonald
McDonald Thermal Engineering
1730 Castellana Road
La Jolla, CA 92037

473. B. J. McEntire
Norton Company, TRW Ceramics
Goddard Road
Northboro, MA 01532-1545

474. Chuck McFadden
Coors Ceramics Company
600 9th Street
Golden, CO 80401

475. Henry McFadden
Magnetic Bearings, Inc.
Engineering Library
609 Rock Road
Radford, VA 24141

476. Thomas D. McGee
Iowa State University
Materials Science and
Engineering Department
110 Engineering Annex
Ames, IA 50011

477. Carol McGill
Corning Inc.
Sullivan Park, FR-02-08
Corning, NY 14831

478. T. C. McLaren
Cameron Forged Products
Company
P.O. Box 1212
Houston, TX 77251-1212

479. James McLaughlin
Sundstrand Power Systems
4400 Ruffin Road
P.O. Box 85757
San Diego, CA 92186-5757

480. Arthur F. McLean
6225 North Camino Almonte
Tucson, AZ 85718

481. Matt McMonigle
U.S. Department of Energy
Improved Energy Productivity
Division
Forrestal Building,
CE-231
Washington, DC 20585

482. Dennis McMurtry
EG&G Idaho, Inc.
Idaho National Engineering
Laboratory
P.O. Box 1625
Idaho Falls, ID 83415

483. D. B. Meadowcroft
National Power Technology
and Environmental Centre
Kelvin Avenue
Leatherhead Surrey
KT22 7SE
ENGLAND AIR MAIL

484. Jo Meglen
11004 Birdfoot Court
Reston, VA 22091

485. Pankaj K. Mehrotra
Kennametal, Inc.
P.O. Box 639
Greensburg, PA 15601

486. Joseph J. Meindl
Reynolds International, Inc.
6603 West Broad Street
P.O. Box 27002
Richmond, VA 23261-7003

487. Michael D. Meiser
Allied-Signal Aerospace Company
Garrett Ceramic Components
Division
19800 South Van Ness Avenue
Torrance, CA 90509

488. George Messenger
National Research Council of
Canada
Engine Laboratory
Building M-7
Ottawa Ontario K1A 0R6
CANADA AIR MAIL

489. D. Messier
U.S. Army Materials Technology
Laboratory
SLCMT-EMC
405 Arsenal Street
Watertown, MA 02172-0001

490. Gary L. Messing
Pennsylvania State University
Ceramic Science and Engineering
Department
119 Steidle Building
University Park, PA 16802

491. Arthur G. Metcalfe
Arthur G. Metcalfe and
Associates, Inc.
2108 East 24th Street
National City, CA 91950

492. R. Metselaar
Eindhoven University
Centre for Technical Ceramics
P.O. Box 513
Eindhoven 5600 MB
THE NETHERLANDS AIR MAIL

493. Nancy S. Meyers
U.S. Department of Energy
Transportation Technologies
CE-30, Forrestal Building
6B-094
Washington, DC 20585

494. David J. Michael
Harbison-Walker Refractories
Company
P.O. Box 98037
Pittsburgh, PA 15227

495. Ken Michaels
Chrysler Motors Corporation
Ceramics Development
Metallurgical Processes
P.O. Box 1118, CIMS:418-17-09
Detroit, MI 48288

496. Bernd Michel
Institute of Mechanics
Fracture and Micromechanics
Department
P.O. Box 408
D-9010 Chemnitz
GERMANY AIR MAIL

497. David E. Miles
Commission of the European
Communities
rue de la Loi, 200
B-1049 Brussels
BELGIUM AIR MAIL

498. John V. Milewski
Superkinetics, Inc.
P.O. Box 8029
Santa Fe, NM 87504

499. Carl E. Miller
AC Rochester
1300 North Dort Highway,
MS:32-31
Engineering Building B
Flint, MI 48556

500. Mike Miller
McGraw-Hill Aviation Week
Performance Materials
1156 15th Street, N.W.
Washington, DC 20005

501. Charles W. Miller, Jr.
Centorr Furnaces/Vacuum
Industries
542 Amherst Street
Nashua, NH 03063

502. R. Mininni
Enichem America
2000 Cornwall Road
Monmouth Junction, NJ 08852

503. Michele V. Mitchell
Allied-Signal Aerospace
Company
Garrett Ceramic Components
Division
19800 South Van Ness Avenue
Torrance, CA 90501-1149

504. Howard Mizuhara
GTE - WESGO
477 Harbor Boulevard
Belmont, CA 94002

505. Helen Moeller
Babcock & Wilcox
P.O. Box 11165
Lynchburg, VA 24506-1165

506. Francois R. Mollard
Metalworking Technology, Inc.
1450 Scalp Avenue
Johnstown, PA 15904

507. Phil Mooney
Panametrics
NDE Division
221 Crescent Street
Waltham, MA 02254

508. Thomas Morel
Ricardo North America
645 Blackhawk Drive
Westmont, IL 60559

509. Geoffrey P. Morris
3M Company
3M Traffic Control Materials
Division
Bldg. 209-BW-10, 3M Center
St. Paul, MN 55144-1000

510. Jay A. Morrison
Rolls-Royce, Inc.
Engineering and Information
Center, Overlook 1
2849 Paces Ferry Road,
Suite 450
Atlanta, GA 30339-3769

511. Joel P. Moskowitz
Ceradyne, Inc.
3169 Redhill Avenue
Costa Mesa, CA 92626

512. Brij Moudgil
University of Florida
Material Science and
Engineering
Gainesville, FL 32611

513. Christoph J. Mueller
Sprechsaal Publishing
Group
P.O. Box 2962, Mauer 2
D-8630 Coburg
GERMANY AIR MAIL

514. Thomas W. Mullan
Vapor Technologies Inc.
345 Route 17 South
Upper Saddle River, NJ 07458

515. M. K. Murthy
MKM Consultants International
10 Avoca Avenue, Unit 1906
Toronto Ontario M4T 2B7
CANADA AIR MAIL

516. Solomon Musikant
TransCon Technologies, Inc.
Materials Science & Engineering
1508 Waynesboro Road
Paoli, PA 19301

517. David L. Mustoe
Custom Technical Ceramics
8041 West I-70 Service Road,
Unit 6
Arvada, CO 80002

518. Curtis V. Nakaishi
U.S. Department of Energy
Morgantown Energy Technology
Center
Collins Ferry Road
P.O. Box 880
Morgantown, WV 26507-0880

519. Yoshio Nakamura
Faicera Research Institute
2-5-8 Hiyakunin-cho Shinjuku-Ko
Tokyo
JAPAN AIR MAIL

520. K. S. Narasimhan
Hoeganaes Corporation
River Road
Riverton, NJ 08077

521. Samuel Natansohn
GTE Laboratories, Inc.
40 Sylvan Road
Waltham, MA 02254

522. Robert Naum
Applied Resources, Inc.
P.O. Box 241
Pittsford, NY 14534

523. Malcolm Naylor
Cummins Engine Company, Inc.
P.O. Box 3005, Mail Code 50183
Columbus, IN 47202-3005

524. Jeffrey Neil
GTE Laboratories, Inc.
40 Sylvan Road
Waltham, MA 02254

525. Fred A. Nichols
Argonne National Laboratory
9700 South Cass Avenue
MCT - Building 212
Argonne, IL 60439

526. H. Nickel
Furschungszentrum Jüelich (KFA)
P.O. Box 1913
Jüelich 1-5170 BRD NRW
GERMANY AIR MAIL

527. Dale E. Niesz
Rutgers University
Center for Ceramic Research
P.O. Box 909
Piscataway, NJ 08855-0909

528. David M. Nissley
United Technologies Corporation
Pratt & Whitney Aircraft
400 Main Street, MS:163-10
East Hartford, CT 06108

529. Richard D. Nixdorf
ReMaxCo Technologies, Inc.
11317 Snyder Road
Knoxville, TN 37932

530. Bernard North
Kennametal, Inc.
P.O. Box 639
Greensburg, PA 15601

531. Bruce E. Novich
Ceramics Process Systems
Corporation
155 Fortune Boulevard
Milford, MA 01757

532. Daniel Oblas
GTE Laboratories, Inc.
40 Sylvan Road
Waltham, MA 02254

533. Don Ohanehi
Magnetic Bearings, Inc.
1908 Sussex Road
Blacksburg, VA 24060

534. Robert Orenstein
General Electric Company
55-112, River Road
Schenectady, NY 12345

535. Norb Osborn
Aerodyne Dallas
151 Regal Row,
Suite 120
Dallas, TX 75247

536. A. M. Paddick
BP International Limited
BP Research Centre, Main
Library
Chertsey Road
Sunbury-on-Thames
Middlesex TW16 7LN
UNITED KINGDOM AIR MAIL

537. Russell J. Page
Kanthal-Artcor
3001 Redhill Avenue, II-109
Costa Mesa, CA 92705

538. Richard Palicka
Cercom, Inc.
1960 Watson Way
Vista, CA 92083

539. Muktesh Paliwal
GTE Products Corporation
Hawes Street
Towanda, PA 18848

540. Joseph E. Palko
General Electric Company
55-113, River Road
Schenectady, NY 12345

541. Hayne Palmour, III
North Carolina State
University
Materials Science and
Engineering Dept.
Raleigh, NC 27605-7905

542. Joseph N. Panzarino
Norton Company
Advanced Ceramics
Goddard Road
Northboro, MA 01532-1545

543. Pellegrino Papa
Corning Inc.
MP-WX-02-1
Corning, NY 14831

544. E. Beth Pardue
Technology for Energy
Corporation
One Energy Center
P.O. Box 22996
Knoxville, TN 37933-0996

545. Soon C. Park
3M Company
3M Center
Building 142-4N-02
P.O. Box 2963
St. Paul, MN 55144

546. Hartmut Paschke
Schott Glaswerke
Christoph-Dorner-Strasse 29
D-8300 Landshut
GERMANY AIR MAIL

547. Marina R. Pascucci
GTE Laboratories, Inc.
40 Sylvan Road
Waltham, MA 02254

548. James W. Patten
Cummins Engine
Company, Inc.
Materials Engineering
P.O. Box 3005, Mail
Code 50183
Columbus, IN 47202-3005

549. Robert A. Penty
Eastman Kodak Company
KAD/D73 - 35612
901 Elmgrove Road
Rochester, NY 14653

550. Robert W. Pepper
Textron Specialty Materials
2 Industrial Avenue
Lowell, MA 01851

551. Peter Perdue
Detroit Diesel Corporation
Research Advanced Development
Group
13400 West Outer Drive,
Speed Code A-07
Detroit, MI 48239-4001

552. Bruce Peters
Dow Chemical Company
Building 52
Midland, MI 48667

553. John J. Petrovic
Los Alamos National Laboratory
Group MST-4, MS:6771
Los Alamos, NM 87545

554. Frederick S. Pettit
University of Pittsburgh
Pittsburgh, PA 15261

555. Ben A. Phillips
Phillips Engineering Company
721 Pleasant Street
St. Joseph, MI 49085

556. Richard C. Phoenix
Ohmtek, Inc.
2160 Liberty Drive
Niagara Falls, NY 14302

557. Bruce J. Pletka
Michigan Technological University
Metallurgical and Materials Engineering Department
Houghton, MI 49931

558. John P. Pollinger
Garrett Ceramic Components
19800 Van Ness Avenue
Torrance, CA 90501

559. P. Popper
High Technology Ceramics International Journal
22 Pembroke Drive
Westlands Newcastle-under-Lyme
Staffs ST5 2JN
ENGLAND AIR MAIL

560. F. Porz
Universitat Karlsruhe
Institut fur Keramik Im Maschinendau
Postfach 6980
D-7500 Karlsruhe
GERMANY AIR MAIL

561. Harry L. Potma
Royal Netherlands Embassy
Science and Technology
4200 Linnean Avenue, N.W.
Washington, DC 20008

562. Bob R. Powell
General Motors Research Laboratories
Metallurgy Department
30500 Mound Road
Box 9055
Warren, MI 48090-9055

563. Stephen C. Pred
ICD Group, Inc.
1100 Valley Brook Avenue
Lyndhurst, NJ 07071

564. Karl M. Prewo
United Technologies Research Center
411 Silver Lane
MS:24
East Hartford, CT 06108

565. Peter E. Price
Industrial Materials Technology, Inc.
P.O. Box 9565
Andover, MA 01810

566. Joseph M. Proud
GTE Laboratories, Inc.
Materials Science Laboratory
40 Sylvan Road
Waltham, MA 02254

567. Vimal K. Pujari
Norton Company
Advanced Ceramics
Goddard Road
Northboro, MA 01532-1545

568. George Quinn
National Institute of Standards and Technology
Ceramics Division, Bldg. 223
Gaithersburg, MD 20899

569. Ramas V. Raman
Ceracon, Inc.
1101 North Market Boulevard,
Suite 9
Sacramento, CA 95834

570. Charles F. Rapp
Owens Corning Fiberglass
2790 Columbus Road
Granville, OH 43023-1200

571. Dennis W. Readey
Colorado School of Mines
Department of Metallurgy
and Materials Engineering
Golden, CO 80401

572. Wilfred J. Rebello
PAR Enterprises, Inc.
12601 Clifton Hunt Lane
Clifton, VA 22024

573. Harold Rechter
Chicago Fire Brick Company
R&D
7531 South Ashland Avenue
Chicago, IL 60620

574. Robert R. Reeber
U.S. Army Research Office
P.O. Box 12211
Research Triangle Park, NC 27709

575. K. L. Reifsnider
Virginia Polytechnic Institute
and State University
Department of Engineering
Science and Mechanics
Blacksburg, VA 24061

576. Paul E. Rempes
McDonnell Douglass Missle
Systems Company
P.O. Box 516,
Mail Code:1066086
St. Louis, MO 63166-0516

577. Gopal S. Revankar
John Deere Company
Metals Research
3300 River Drive
Moline, IL 61265

578. K. T. Rhee
Rutgers University
Mechanical Engineering
P.O. Box 909
Piscataway, NJ 08854

579. James Rhodes
Advanced Composite Materials
Corporation
1525 South Buncombe Road
Greer, SC 29651

580. Roy W. Rice
W. R. Grace and Company
7379 Route 32
Columbia, MD 21044

581. David W. Richerson
2093 East Delmont Drive
Salt Lake City, UT 84117

582. Tomas Richter
J. H. France Refractories
1944 Clarence Road
Snow Shoe, PA 16874

583. Michel Rigaud
Ecole Polytechnique
Campus Universite De Montreal
P.O. Box 6079, Station A
Montreal, P.Q Quebec H3C 3A7
CANADA AIR MAIL

584. R. E. Riman
Rutgers University
Ceramics Engineering
Department
P.O. Box 909
Piscataway, NJ 08855-0909

585. Barry Ringstrom
Superior Graphite Company
P.O. Box 2373
Smyrna, GA 30081

586. John E. Ritter
University of Massachusetts
Mechanical Engineering
Department
Amherst, MA 01003

587. Frank L. Roberge
Allied-Signal Aerospace Company
Garrett Auxiliary Power Division
P.O. Box 5227
Phoenix, AZ 85010

588. W. Eric Roberts
Advanced Ceramic Technology, Inc.
990 "F" Enterprise Street
Orange, CA 92667

589. Martha Rohr
U.S. Department of Energy
DOE Oak Ridge Field Office
Building 4500N
P.O. Box 2008, MS:6269
Oak Ridge, TN 37831-6269

590. Y. G. Roman
TNO TPD Keramick
P.O. Box 595
Einhoven 5600 AN
HOLLAND AIR MAIL

591. Mark D. Roos
Carborundum Company
P.O. Box 156
Niagara Falls, NY 14302

592. Michael Rossetti
Arthur D. Little, Inc.
15 Acorn Park
Cambridge, MA 01240

593. Barry R. Rossing
Lanxide Corporation
1300 Marrows Road
Newark, DE 19714-6077

594. Steven L. Rotz
Lubrizol Corporation
29400 Lakeland Boulevard
Wickliffe, OH 44092

595. Bruce Rubinger
Global Competitiveness, Inc.
One Devonshire Place, Suite 1011
Boston, MA 02109

596. Robert Ruh
Wright Laboratory
WL/MLLM
Wright-Patterson AFB, OH 45433

597. Robert J. Russell
17 Highgate Road
Framingham, MA 01701

598. L. William Sahley
Supermaterials Company
24400 Highland Road
Richmond Heights, OH 44143

599. Jon Salem
NASA Lewis Research Center
21000 Brookpark Center
Cleveland, OH 44135

600. W. A. Sanders
NASA Lewis Research Center
21000 Brookpark Road,
MS:49-3
Cleveland, OH 44135

601. J. Sankar
North Carolina A&T State University
Department of Mechanical Engineering
Greensboro, NC 27411

602. Yasushi Sato
NGK Spark Plugs (U.S.A.), Inc.
1200 Business Center Drive, Suite 300
Mt. Prospect, IL 60056

603. Maxine L. Savitz
Allied-Signal Aerospace Company
Garrett Ceramic Components Division
19800 South Van Ness Avenue
Torrance, CA 90501

604. Ashok Saxena
Georgia Institute of Technology
Materials Engineering
Atlanta, GA 30332-0245

605. David W. Scanlon
Instron Corporation
100 Royall Street
Canton, MA 02021

606. Charles A. Schacht
Schacht Consulting Services
12 Holland Road
Pittsburgh, PA 15235

607. James Schienle
Allied-Signal Aerospace Company
Garrett Auxiliary Power Division
2739 East Washington Street
P.O. Box 5227, MS:1302-2P
Phoenix, AZ 85010

608. John C. Schneider
San Juan Technologies
P.O. Box 49326
Colorado Springs, CO 80949-9326

609. Gary Schnittgrund
Rocketdyne, BA05
6633 Canoga Avenue
Canoga Park, CA 91303

610. Mark Schomp
Lonza, Inc.
Corporate Headquarters
17-17 Route 208
Fair Lann, NJ 07410

611. Joop Schoonman
Delft University of Technology
Laboratory for Inorganic Chemistry
P.O. Box 5045
2600 GA Delft
THE NETHERLANDS AIR MAIL

612. John Schuldies
Industrial Ceramic Technology, Inc.
37 Enterprise Drive
Ann Arbor, MI 48103

613. Robert B. Schulz
U.S. Department of Energy
Office of Transportation Materials
CE-34, Forrestal Building
Washington, DC 20585

614. Murray A. Schwartz
Materials Technology Consulting, Inc.
30 Orchard Way, North
Potomac, MD 20854

615. Peter Schwarzkopf
SRI International
333 Ravenswood Avenue
Menlo Park, CA 94025

616. Thomas C. Schweizer
Princeton Economic Research, Inc.
12300 Twinbrook Pkwy., Suite 650
Rockville, MD 20852

617. William T. Schwessinger
Multi-Arc Scientific Coatings
1064 Chicago Road
Troy, MI 48083-4297

618. W. D. Scott
University of Washington
Materials Science Department
Mail Stop:FB10
Seattle, WA 98195

619. Nancy Scoville
Thermo Electron Technologies
74 West Street
P.O. Box 9046
Waltham, MA 02254-9046

620. Brian Seegmiller
Coors Ceramics Company
600 9th Street
Golden, CO 80401

621. T. B. Selover
AICRE/DIPPR
3575 Traver Road
Shaker Heights, OH 44122

622. J. H. Selverian
GTE Laboratories, Inc.
40 Sylvan Road
Waltham, MA 02254

623. Charles E. Semler
Semler Materials Services
4160 Mumford Court
Columbus, OH 43220

624. Thomas Service
Service Engineering Laboratory
324 Wells Street
Greenfield, MA 01301

625. Kish Seth
Ethyl Corporation
R&D Laboratories
P.O. Box 341
Baton Rouge, LA 70821

626. Karleen Seybold
Allied-Signal Aerospace
Company
Garrett Auxiliary Power
Division
P.O. Box 5227
Phoenix, AZ 85010

627. William J. Shack
Argonne National Laboratory
9700 South Cass Avenue
Building 212
Argonne, IL 60439

628. Peter T. B. Shaffer
Technical Ceramics
Laboratories, Inc.
4045 Nine/McFarland Drive
Alpharetta, GA 30201

629. Richard K. Shaltens
NASA Lewis Research Center
21000 Brookpark Road,
MS:301-2
Cleveland, OH 44135

630. Robert S. Shane
238 Hemlock Road
Wynnewood, PA 19096

631. Daniel Shanefield
Rutgers University
Ceramics Engineering
Department
P.O. Box 909
Piscataway, NJ 08855-0909

632. Ravi Shankar
Chromalloy
Research and Technology
Division
Blaisdell Road
Orangeburg, NY 10962

633. Terence Sheehan
Alpex Wheel Company
727 Berkley Street
New Milford, NJ 07646

634. Dinesh K. Shetty
University of Utah
304 EMRO, Dept. of Materials
Science and Engineering
Salt Lake City, UT 84112

635. Masahide Shimizu
Ceramic Society of Japan
2-2-503 Takiyama 6-chome
Higashikurume-Shi Tokyo 203
JAPAN AIR MAIL

636. John Shipinski
Toyota Technical Center
U.S.A., Inc.
Technical Research Department
2000 Town Center, Suite 500
Southfield, MI 48075

637. Thomas Shreves
American Ceramic Society, Inc.
Library
757 Brooksedge Plaza Drive
Westerville, OH 43081-2821

638. Jack D. Sibold
Coors Ceramics Company
Contracts for Corporate
Technology
4545 McIntyre Street
Golden, CO 80403

639. George H. Siegel
Point North Associates, Inc.
P.O. Box 907
Madison, NJ 07940

640. Richard Silberglitt
Technology Assessment and Transfer, Inc.
133 Defense Highway, #212
Annapolis, MD 21401

641. Mary Silverberg
Norton Company
Advanced Ceramics Library
Goddard Road
Northboro, MA 01532-1545

642. Gurpreet Singh
Department of the Navy
Internal Combustion & Gas Turbine Engine Division
Code 56X31
Washington, DC 20362-5101

643. Maurice J. Sinnott
University of Michigan
Chemical and Metallurgical Engineering
5106 IST Building
Ann Arbor, MI 48109-2099

644. John Skildum
3M Company
3M Center
Building 224-2S-25
St. Paul, MN 55144

645. David P. Smith
Hoskins, Rees & Smith
1910 Cochran Road
Manor Oak II, Suite 658
Pittsburgh, PA 15220

646. Richard H. Smoak
Smoak & Associates
3554 Hollyslope Road
Altadena, CA 91001-3923

647. Jay R. Smyth
Allied-Signal Aerospace Company
Garrett Auxiliary Power Division
2739 East Washington Street
P.O. Box 5227
MS:93-173/1303-207
Phoenix, AZ 85010

648. Edward A. Snajdr
Premier Refractories and Chemicals, Inc.
P.O. Box 392
Findlay, OH 44815

649. Rafal A. Sobotowski
British Petroleum Company
Technical Center, Broadway
3092 Broadway Avenue
Cleveland, OH 44115

650. A. G. Solomah
SAC International Ltd.
1445 Bonhill Road, # 13
Mississauga Ontario L5T 1V3
CANADA AIR MAIL

651. S. Somiya
Nishi Tokyo University
3-7-19 Soijo, Setagaya
Tokyo 157
JAPAN AIR MAIL

652. Boyd W. Sorenson
DuPont Lanxide Composites
1300 Marrows Road
P.O. Box 6077
Neward, DE 19707

653. Charles A. Sorrell
U.S. Department of Energy
Advanced Industrial Concepts Division
CE-232, Forrestal Building
Washington, DC 20585

654. C. Spencer
EA Technology
Capenhurst Chester
CH1 6ES
UNITED KINGDOM AIR MAIL

655. Allen Spizzo
Hercules, Inc.
Hercules Plaza
Wilmington, DE 19894

656. Richard M. Spriggs
Alfred University
Center for Advanced Ceramic Technology
Alfred, NY 14802

657. Charles Spuckler
NASA Lewis Research Center
21000 Brookpark Road
MS: 5-11
Cleveland, OH 44135-3191

658. M. Srinivasan
Material Solutions
P.O. Box 663
Grand Island, NY 14702-0663

659. Gordon L. Starr
Cummins Engine Company, Inc.
Design & Technology
P.O. Box 3005
Mail Code 50182
Columbus, IN 47202-3005

660. Jim Stevenson
Windrock, Incorporated
154 Fairbanks Plaza
Oak Ridge, TN 37830

661. Tom Stillwagon
Allied-Signal Aerospace Company
Garrett Ceramic Components Division
19800 South Van Ness Avenue
Torrance, CA 90501

662. Harold L. Stocker
General Motors Corporation
Allison Gas Turbine Division
P.O. Box 420
Indianapolis, IN 46206

663. Paul D. Stone
Dow Chemical USA
1776 "Eye" Street, N.W.,
Suite 575
Washington, DC 20006

664. Roger S. Storm
Carborundum Company
Technology Division
P.O. Box 337
Niagara Falls, NY 14302-0337

665. Peter A. Stranges
4 Chittenden Lane
Owings Mills, MD 21117

666. F. W. Stringer
Aero & Industrial Technology Ltd.
P.O. Box 46, Wood Top
Burnley Lancashire BB11 4BX
UNITED KINGDOM AIR MAIL

667. Thomas N. Strom
NASA Lewis Research Center
21000 Brookpark Road
MS:86-6
Cleveland, OH 44135

668. M. F. Stroosnijder
Institute for Advanced Materials
Joint Research Centre
21020 Ispra (VA)
ITALY AIR MAIL

669. Karsten Styhr
30604 Ganado Drive
Rancho Palos Verdes, CA 90274

670. T. S. Sudarshan
Materials Modification, Inc.
2929-P1 Eskridge Center
Fairfax, VA 22031

671. M. J. Sundaresan
University of Miami
Mechanical Engineering Department
P.O. Box 248294
Coral Gables, FL 33124

672. Patrick L. Sutton
U.S. Department of Energy
Advanced Propulsion Division
CE-322, Forrestal Building
Washington, DC 20585

673. Willard H. Sutton
United Technologies
Corporation
Research Center, MS:24
Silver Lane
East Hartford, CT 06108

674. Ron Sviben
100 Indel Avenue
Rancocas, NJ 08073

675. J. J. Swab
U.S. Army Materials Technology
Laboratory
Ceramics Research Division
SLCMT-EMC
405 Arsenal Street
Watertown, MA 02172

676. Robert E. Swanson
Metalworking Technology, Inc.
1450 Scalp Avenue
Johnstown, PA 15904

677. Scott L. Swartz
Battelle Columbus
Laboratories
Metals and Ceramics
505 King Avenue
Columbus, OH 43201

678. Steve Szaruga
Air Force Wright Aeronautical
Laboratory
Materials Directorate
WL/MLBC
Wright-Patterson
AFB, OH 45433-6533

679. Yo Tajima
NGK Spark Plug Company, Ltd.
NTK Technical Ceramic Division
2808 Iwasaki
Komaki-shi Aichi-ken 485
JAPAN AIR MAIL

680. Fred Teeter
5 Tra.ee Terrace
East Amherst, NY 14051

681. Monika O. Ten Eyck
Carborundum Company
Technology Division
P.O. Box 832
Niagara Falls, NY 14302

682. David F. Thompson
Corning Glass Works
SP-DV-02-1
Corning, NY 14831

683. Merle L. Thorpe
Hobart Tafa Technologies, Inc.
146 Pembroke Road
Concord, NH 03301

684. Eberhard Tiefenbacher
Daimler-Benz AG Abt. FIS
Mercedes-Strabe 136
Stuttgart 60
GERMANY AIR MAIL

685. T. Y. Tien
University of Michigan
Materials Science and
Engineering Department
Dow Building
Ann Arbor, MI 48103

686. Julian M. Tishkoff
Air Force Office of Scientific
Research
AFOSR/NA
Bolling AFB, DC 20332-6448

687. D. M. Tracey
Norton Company
Advanced Ceramics
Goddard Road
Northboro, MA 01532-1545

688. Dick Trippett
General Motors Corporation
Allison Gas Turbine Division
P.O. Box 420, MS:W-16
Indianapolis, IN 46206-0420

689. L. J. Trostel, Jr.
Box 199
Princeton, MA 01541

690. W. T. Tucker
General Electric Company
Corporate R&D
Building K1-4C35
P.O. Box 8
Schenectady, NY 12301

691. Masanori Ueki
Nippon Steel Corporation
Central R&D Bureau
1618 Ida
Nakahara-Ku Kawasaki 211
JAPAN AIR MAIL

692. Filippo M. Ugolini
ATA Studio
Via Degli Scipioni, 268A
ROMA 00192
ITALY AIR MAIL

693. Donald L. Vaccari
Allison Gas Turbines
P.O. Box 420
Speed Code S49
Indianapolis, IN 46206-0420

694. Carl F. Van Conant
Boride Products, Inc.
2879 Aero Park Drive
Traverse City, MI 49684

695. Marcel H. Van De Voorde
Commission of the European Communities
Institute for Advanced Materials
Joint Research Centre
P.O. Box 2
1755 ZG Petten
THE NETHERLANDS AIR MAIL

696. O. Van Der Biest
Katholieke Universiteit Leuven
Departement Metaalkunde en Toegepaste
de Croylaan 2
B-3030 Leuven
BELGIUM AIR MAIL

697. Michael Vannier
Washington University, St. Louis
Mallinckrodt Institute of Radiology
510 South Kings Highway
St. Louis, MO 63110

698. Stan Venkatesan
Southern Coke & Coal Corporation
P.O. Box 52383
Knoxville, TN 37950

699. V. Venkateswaran
Carborundum Company
Niagara Falls R&D Center
P.O. Box 832
Niagara Falls, NY 14302

700. Dennis Viechnicki
U.S. Army Materials Technology Laboratory
405 Arsenal Street
Watertown, MA 02172-0001

701. Ted Vojnovich
U.S. Department of Energy
Office of Energy Research, ER-42
Washington, DC 20585

702. John D. Volt
E. I. Dupont de Nemours & Company, Inc.
P.O. Box 80262
Wilmington, DE 19880

703. John B. Wachtman
Rutgers University
Ceramics Department
P.O. Box 909
Piscataway, NJ 08855

704. Shigetaka Wada
Toyota Central Research Labs, Inc.
Nagakute Aichi 480-11
JAPAN AIR MAIL

705. Janet Wade
Allied-Signal Aerospace Company
Garrett Auxiliary Power Division, Department 93-772
P.O. Box 5227, MS:1303-2
Phoenix, AZ 85010

706. Richard L. Wagner
Ceramic Technologies, Inc.
537 Turtle Creek South Drive, Suite 24D
Indianapolis, IN 46227

707. J. Bruce Wagner, Jr.
Arizona State University
Center for Solid State Science
Tempe, AZ 85287-1704

708. Daniel J. Wahlen
Kohler, Co.
444 Highland Drive
Kohler, WI 53044

709. Ingrid Wahlgren
Royal Institute of Technology
Studsvik Library
S-611 82 Nykoping
SWEDEN AIR MAIL

710. Ron H. Walecki
Allied-Signal Aerospace Company
Garrett Ceramic Components Division
19800 South Van Ness Avenue
Torrance, CA 90501

711. Michael S. Walsh
Vapor Technologies Inc.
2100 Central Avenue
Boulder, CO 80301

712. Chien-Min Wang
Industrial Technology Research Institute
Materials Research Laboratories
195 Chung-Hsing Road, Sec. 4
Chutung Hsinchu 31015 R.O.C.
TAIWAN AIR MAIL

713. Robert M. Washburn
ASMT
11203 Colima Road
Whittier, CA 90604

714. Gerald Q. Weaver
Carborundum Specialty Products
42 Linus Allain Avenue
Gardner, MA 01440-2478

715. Karen E. Weber
Detroit Diesel Corporation
Technology and Planning
13400 West Outer Drive
Detroit, MI 48239-4001

716. R. W. Weeks
Argonne National Laboratory
MCT-212
9700 South Cass Avenue
Argonne, IL 60439

717. Ludwig Weiler
ASEA Brown Boveri AG
Corporate Research
Eppelheimer Str. 82
D-6900 Heidelberg
GERMANY AIR MAIL

718. James Wessel
Dow Corning Corporation
1800 "M" Street, N.W., Suite 325 South
Washington, DC 20036

719. Robert D. West
Therm Advanced Ceramics
P.O. Box 220
Ithaca, NY 14851

720. Thomas J. Whalen
Ford Motor Company
26362 Harriet
Dearborn Heights, MI 48127

721. Ian A. White
Hoeganaes Corporation
River Road
Riverton, NJ 08077

722. Alan Whitehead
General Electric Company
1 River Road, 55-111
Schenectady, NY 12345

723. Sheldon M. Wiederhorn
National Institute of
Standards and Technology
Building 223, Room A329
Gaithersburg, MD 20899

724. John F. Wight
Alfred University
McMahon Building
Alfred, NY 14802

725. D. S. Wilkinson
McMaster University
Materials Science and
Engineering Department
1280 Main Street, West
Hamilton Ontario L8S 4L7
CANADA AIR MAIL

726. James C. Williams
General Electric Company
Engineering Materials
Technology Labs
One Neumann Way
Mail Drop: H85
Cincinnati, OH 45215-6301

727. Janette R. Williams
Kollmorgen Corporation
PCK Technology Division
150 Motor Parkway, # 262
Hauppauge, NY 11788-5108

728. Steve J. Williams
RCG Hagler Bailly, Inc.
1530 Wilson Boulevard,
Suite 900
Arlington, VA 22209-2406

729. Craig A. Willkens
Norton Company
Advanced Ceramics
Goddard Road
Northboro, MA 01532-1545

730. Roger R. Wills
TRW, Inc.
Valve Division
1455 East 185th Street
Cleveland, OH 44110

731. David Gordon Wilson
Massachusetts Institute of
Technology
Mechanical-Engineering
Department
77 Massachusetts Avenue,
Room 3-455
Cambridge, MA 02139

732. Matthew F. Winkler
Seaworthy Systems, Inc.
P.O. Box 965
Essex, CT 06426

733. Gerhard Winter
Hermann C. Starck Berlin GmbH,
Werk Goslar
P.O. Box 25 40
D-3380 Goslar 3380
GERMANY AIR MAIL

734. W. L. Winterbottom
Ford Motor Company
Material Systems Reliability
Department
20000 Rotunda Drive
SRL, Room E-3182
P.O. Box 2053
Dearborn, MI 48121

735. David G. Wirth
Coors Ceramics Company
600 9th Street
Golden, CO 80401

736. Thomas J. Wissing
Eaton Corporation
Engineering & Research Center
P.O. Box 766
Southfield, MI 48037

737. James C. Withers
MER Corporation
7960 South Kolb Road
Building F
Tucson, AZ 85706

738. Dale E. Wittmer
Southern Illinois University
Mechanical Engineering
Department
Carbondale, IL 62901

739. Warren W. Wolf
Owens Corning Fiberglass
2790 Columbus Road, Route 16
Granville, OH 43023

740. George W. Wolter
Howmet Turbine Components
Corporation
Technical Center
699 Benston Road
Whitehall, MI 49461

741. James C. Wood
NASA Lewis Research Center
21000 Brookpark Road
MS:86-6
Cleveland, OH 44135

742. Marrill Wood
LECO Corporation
Augusta Division
P.O. Box 211688
Augusta, GA 30917-1688

743. Wayne L. Worrell
University of Pennsylvania
Department of Materials
Science and Engineering
3231 Walnut Street
Philadelphia, PA 19104

744. John F. Wosinski
Corning Inc.
ME-2 E-5 H8
Corning, NY 14830

745. Ian G. Wright
Battelle Columbus Laboratories
505 King Avenue
Columbus, OH 43201

746. Ruth Wroe
ERDC
Metals & Materials Industries
Division
Capenhurst Chester CH1 6ES
ENGLAND AIR MAIL

747. Bernard J. Wrona
Advanced Composite Materials
Corporation
1525 South Buncombe Road
Greer, SC 29651

748. Carl C. M. Wu
Naval Research Laboratory
Ceramic Branch, Code 6373
Washington, DC 20375

749. John C. Wurst
University of Dayton Research
Institute
300 College Park
Dayton, OH 45469-0101

750. Neil Wyant
ARCH Development Corp.
9700 South Cass Avenue
Building 202
Argonne, IL 60439

751. Roy Yamamoto
Texaco Inc.
P.O. Box 509
Beacon, NY 12508-0509

752. John Yamanis
Allied-Signal, Inc.
Ceramics Program
P.O. Box 1021
Morristown, NJ 07962-1021

753. Harry C. Yeh
Allied-Signal Aerospace
Company
Garrett Ceramic Components
Division
19800 South Van Ness Avenue
Torrance, CA 90509

754. Hiroshi Yokoyama
Hitachi Research Lab
4026 Kuji-Cho
Hitachi-shi Ibaraki 319-12
JAPAN AIR MAIL

755. Thomas M. Yonushonis
Cummins Engine Company, Inc.
P.O. Box 3005
Mail Code 50183
Columbus, IN 47202-3005

756. Thomas J. Yost
Corning, Inc.
Technical Products Division,
Main Plant 21-1-2
Corning, NY 14831

757. Jong Yung
Sundstrand Aviation
Operations
Department 789-6
4747 Harrison Avenue
Rockford, IL 61125

758. A. L. Zadoks
Caterpillar Inc.
Technical Center, Building L
P.O. Box 1875
Peoria, IL 61656-1875

759. Avi Zangvil
University of Illinois
Materials Research Laboratory
104 South Goodwin Avenue
Urbana, IL 61801

760. Charles H. Zenuk
Transtech
6529 East Calle Cavalier
Tucson, AZ 85715

761. Anne Marie Zerega
U.S. Department of Energy
Office of Energy Research,
ER-42
Washington, DC 20585

762. Ken Zillmer
Applied Test Systems, Inc.
2571 Mt. Gallant Road
Rock Hill, SC 29730

763. Carl Zweben
General Electric Company
P.O. Box 8555, VFSC/V4019
Philadelphia, PA 19101

764. Klaus M. Zwilsky
National Research Council
National Materials
Advisory Board
2101 Constitution Avenue
Washington, DC 20418

765. Department of Energy
DOE Field Office, Oak Ridge
Assistant Manager for Energy
Research and Development
P.O. Box 2001
Oak Ridge, TN 37831-8501

766-775. Department of Energy
Office of Scientific and
Technical Information
Office of Information
Services
P.O. Box 62
Oak Ridge, TN 37831

For distribution by microfiche
as shown in DOE/OSTI-4500,
Distribution Category UC-332
(Ceramics/Advanced Materials).

END

DATE FILMED

10/28/92